Ligand Rearrangements of Organometallic Complexes in Solution

by

Jennifer Elaine Shanoski

B.S. (Wayne State University) 2000

A dissertation submitted in partial satisfaction
of the requirements for the degree of

Doctor of Philosophy

in

Chemistry

in the

GRADUATE DIVISION

of the

UNIVERSITY OF CALIFORNIA, BERKELEY

Committee in charge:

Professor Charles B. Harris, Chair
Professor Richard J. Saykally
Professor Roger W. Falcone

Spring 2006

The dissertation of Jennifer Elaine Shanoski is approved.

Chair Date

Date

Date

University of California, Berkeley

Spring 2006

Ligand Rearrangements of Organometallic Complexes in Solution

by

Jennifer Elaine Shanoski

Abstract

Ligand Rearrangements of Organometallic Complexes in Solution

by

Jennifer Elaine Shanoski

Doctor of Philosophy in Chemistry

University of California, Berkeley

Professor Charles B. Harris, Chair

Many chemical reactions utilize organometallic complexes as catalysts. These complexes find use in reactions as varied as bond activation, polymerization, and isomerization. An understanding of the mechanism can be obtained indirectly from many techniques including matrix isolation, reactant modification, and intermediate isolation. A tool that directly monitors the reaction under the conditions of the synthesis is, however, of greater general use in obtaining a detailed picture of the reaction. Ultrafast, UV-pump, IR-probe spectroscopy is such a tool, allowing for experimental monitoring of complex reaction dynamics in the condensed phase. Organometallic complexes are well suited to this type of experiment since many of the ligands have strong infrared absorptions that are highly dependent on the electronic nature of the metal center. Further, organometallic complexes that are ultimately utilized in synthetic applications undergo many fundamental condensed phase processes. It is these fundamental processes and the reactions that ultimately result that are the topic of this thesis.

This thesis outlines the construction of a new ultrafast laser system with an emphasis on the generation of tunable mid-infrared pulses, data collection, and data analysis. This system is then used to investigate the formation of vinylidene complexes with group 6 hexacarbonyl complexes. As the first step in polymerization reactions, the formation of

vinylidene complexes is of general interest. Our findings indicate that this is a higher energy process than originally thought and that solvation and rearrangement are important steps preceding this chemical event. The rearrangement of alkyne complexes is directly comparable to that of alcohols and silanes. This comparison led to a comprehensive experimental and theoretical investigation of such rearrangements in long chain alcohols. In these studies, we find that inter- and intramolecular descriptions of the rearrangement are not different when the reaction is considered as diffusive motion along a barrier. These labels have been utilized extensively in the past and our findings indicate that this may be inappropriate. As a primary process in reaction dynamics, such a conclusion provides a new context for linkage isomerization reactions.

The last project outlined in this thesis is centered on understanding the mechanistic details of boryl mediated carbon-hydrogen bond activation. Transition-metal boryl complexes have shown to be effective catalysts in the selective functionalization of hydrocarbons. Experimental studies which trace the reactive pathways for these complexes provide important insight which can aid in the development of future synthetic schemes. We have investigated the ultrafast reactivity of these complexes in both saturated and unsaturated hydrocarbons and have found multiple photolytically induced reaction channels. Additionally, we have confirmed that the bond activation process is high in energy and must be studied on the nano- to millisecond timescale.

Professor Charles B. Harris
Dissertation Committee Chair

In memory of my mother.

Contents

List of Figures

List of Tables

Acknowledgements

I would like to thank my advisor, Professor Charles Harris for providing me with the opportunity and support needed to carry out the research described in this thesis. I have been extremely lucky to have an advisor that has allowed me to explore many facets of academia including allowing me to teach extensively at various institutions. In addition, I am grateful for the continued encouragement to continue a career in research that Charles has provided me. In addition to Charles, I would like to thank Vijaya Narasimhan for everything that she continues to do for the group. There is no possibility of a Harris group without Vijaya and I am eternally grateful for her kindness, hard work, and meticulous management.

I would also like to acknowledge all of the people that I have had the good fortune to work with in the Harris group. I am particularly grateful to Libby Glascoe for everything that she has done to help me with the work described in this thesis. I am indebted to Libby for all of the hours that she spent working on the laser for me and the fact that she rarely complained about having to do so. Matthias Kling has fixed many of my errors and has always been polite about doing so. Christine Payne and Preston Snee together helped to start my graduate career and continue to be supportive, encouraging, and fun. Karma Sawyer, Jacob Schlegel, and James Cahoon who, as the next generation of liquid side folk, taught me more about research than I ever expected and who I am counting on for the next wave of Harris group research. I am also grateful to Steve Robertson who always had time to smoke, debug code, and talk science with me. Sean Garrett-Roe has provided me with more data presentation information than I ever wanted to know and can always be counted on for critical readings and assistance. Matt Strader, Aram Yang (my SV bro), James Johns ("Fievel"), and Paul Szymanski have all, as members of the surface side, been great additions to life in the group.

Finally, I would like to thank my family and friends for supporting me through my graduate career: my brother Dan who I consider one of my best friends, my brother Rick who thinks I am smarter than I am, Jeny who gave me Tristen and is like the sister that I never had, my Aunt for continuing her snail-mail correspondence, my grandparents who have provided me with continued support, my future family-in-law who are simply incredible,

Brenda who has remained my nearest and dearest despite the miles, Bob and Delores for a continuum of weekly lunches, and Jen who is one of the smartest people that I've ever met, an incredible friend, and the only one to read these pages from beginning to end. Finally, I would like to thank Engelbert for changing my life in ways that amaze me every day - I am looking forward to a lifetime of continued amazement.

This work was funded by the National Science Foundation and specialized equipment was provided by the U.S. Department of Energy (Office of Basic Energy Sciences, Chemical Sciences Division, Contract No. DE-AC02-05CH11231).

Chapter 1

Introduction and Background

1.1 Introduction

Organometallic complexes are primary participants in many important chemical processes including bond activation,(1; 2) ligand isomerization,(3) ligand exchange,(4) and functionalization reactions.(5) Used both as catalysts in industrial applications and as probes for fundamental chemical processes, a considerable amount of research has been carried out on the photochemistry of organometallic complexes.(6) Techniques aimed at isolating the intermediate species include matrix-isolation (7) and low temperature NMR.(8) While these experiments have proved to be extremely useful in gaining an understanding of many reaction processes and identifying intermediate species, they are limited in their ability to monitor reactions under real-world conditions. The environment in which reactions actually occur and those in which many mechanistic experiments are performed are drastically different. For example, alkyne polymerization is industrially carried out in room temperature solutions,(9) while the mechanistic studies of this reaction were primarily done in glassy matrices at low temperature.(10; 11) In matrix-isolation studies, the rigidity of the environment can cage reactants providing an alternative mechanistic route. Further, low temperature studies, in general, cannot obtain reliable kinetic data and the resulting thermodynamic parameters for a given reaction. Since the solvent environment can play a key

role in the reaction dynamics, it is important to study the mechanistic details of these reactions in solution at room temperature.

While the solvent environment is often a direct participant in the chemistry of interest, it generally complicates the process of observing reaction dynamics: spectroscopic absorptions are inhomogeneously and homogeneously broadened by the solvent environment compared to the gas phase peaks; higher temperatures result in faster kinetic behavior; and the solvent provides an energy bath for the dynamics. The availability of ultrafast lasers, improved detection devices, and fast data acquisition have allowed the study of many condensed phase reactions that could not be studied previously.(12) This thesis is focused on using such ultrafast techniques to gain an understanding of both fundamental and practical aspects of condensed phase, organometallic photochemistry.

1.2 Experimental Background

In order to understand the dynamic behavior of the organometallic complexes studied in this thesis, it is important to first become familiar with the basic principles of the experimental techniques used by our group. The starting materials in the reactions studied all have a transition metal center and carbonyl ligands. Ultraviolet-pump/infrared-probe spectroscopy is ideally suited to the mechanistic investigations of complexes with these features. The ultraviolet pump beam initiates the reaction and the infrared probe beam is used to detect changes in the spectroscopic signatures of parent, transient, and product species. A brief discussion of the important aspects of the experiment is given below; for a more extensive treatment of these topics one should refer to the thesis of Christine Payne.(13)

In all of the experiments described in this thesis, the pump beam is 266 nm light. Excitation is to a metal-to-ligand charge-transfer band which crosses into a dissociative state and results in the loss of a single carbonyl ligand.(14) The eighteen electron rule (analogous to the octet rule) is violated with the loss of the carbonyl group, a two electron donor in the language of inorganic chemistry. The unstable, sixteen electron complex that results will be referred to as an unsaturated metal center throughout this thesis. Because the reaction is performed in the condensed phase at room temperature, a solvent molecule is always

in close proximity to the metal center and provides stabilization through solvation. This process of solvation has been shown to occur within 1-2 ps after the photoinduced loss of a single carbonyl ligand.(15; 16; 17; 18) The degree to which the newly formed complex is energetically stable will determine subsequent mechanistic steps and the timescales associated with those steps. It is these details which we probe in our experiment.

The probe beam is a tunable infrared pulse of light. Carbonyl ligands have sharp, strong absorptions in the infrared region of the electromagnetic spectrum that are particularly sensitive to the electronic properties of the metal center. The basis for this sensitivity is the bonding type of the carbonyl group to the metal.(4) Two different interactions, shown in Figure 1.1, occur between the metal center and the carbonyl ligand: σ-bonding and π-backbonding. The σ-bonding interaction is typical in that the ligand donates a lone pair of electrons to an empty metal d or p orbital. It is the π-backbonding, however, which provides a sensitive probe of the metal center. In π-backbonding, a filled metal d orbital donates electron density into the antibonding, π^* orbital of the carbonyl group. The increased electron count in the carbonyl antibonding orbital weakens the carbon-oxygen bond. If one considers the carbonyl ligand as a classical spring, the weakening of the carbon-oxygen bond results in a smaller spring constant and, consequently, a lower frequency of vibration. A greater electron density at the metal center results in increased electron donation to the carbonyl group and a lower energy vibration. Conversely, a lower electron density at the metal center results in a decreased electron donation to the carbonyl group and a higher energy vibration. Hence, monitoring the carbonyl stretching frequency provides important information about electron density changes at the metal center.

As an example, in Figure 1.2 the calculated frequencies for all complexes in a simple reaction scheme are shown.[1] The parent species, $Cr(CO)_6$, is the reference for comparison and has a characteristic antisymmetric CO stretching frequency at 1998 cm^{-1}. Upon excitation with 266 nm light, a single carbonyl group is dissociated. The coordinatively unsaturated metal pentacarbonyl complex has increased electron density at the metal center because of the loss of backbonding and the stretching frequency decreases to 1983 cm^{-1}. In an alcohol solution, coordination to an alkyl group of the alcohol solvent molecule can

[1]Calculations of the type given here will discussed in detail in Section 1.3.

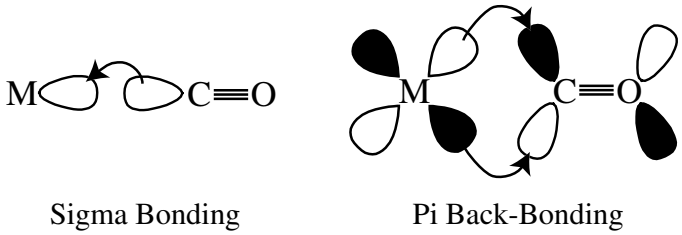

Figure 1.1. The two types of bonding found in metal-carbonyl complexes: σ-bonding and π-backbonding.

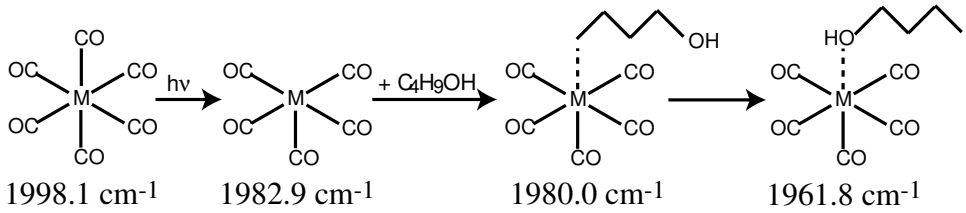

Figure 1.2. Calculated vibrational frequencies for the antisymmetric carbonyl stretch of a series of pertinent complexes.

occur. The alkyl group donates some electron density to the metal, but is not capable of backbonding and the carbonyl stretching frequency decreases further to 1980 cm^{-1}. This alkyl coordinated complex will eventually rearrange to the thermodynamically more stable hydroxyl coordinated complex as shown in Figure 1.2 and discussed in Chapter 4. Because the oxygen group coordinates via one of its lone pairs, the amount of electron density donated to the metal is larger than with the alkyl coordination and results in an appropriately larger frequency shift with the carbonyl stretch appearing at 1962 cm^{-1}. These shifts in the carbonyl absorption frequencies were monitored and analyzed in the experimental spectra discussed in this thesis.

All of the UV-pump/IR-probe spectra presented here are difference spectra. The spectra are constructed by subtracting an unpumped (but probed) spectrum from a pumped (and probed) spectrum reported at a given delay time after photoexcitation. Because the concentration of transient species is very small with respect to the concentration of starting material, such a procedure allows for the observation of minute changes (ΔmOD=50) in the absorption spectrum. The resulting spectra show positive absorptions for species that have

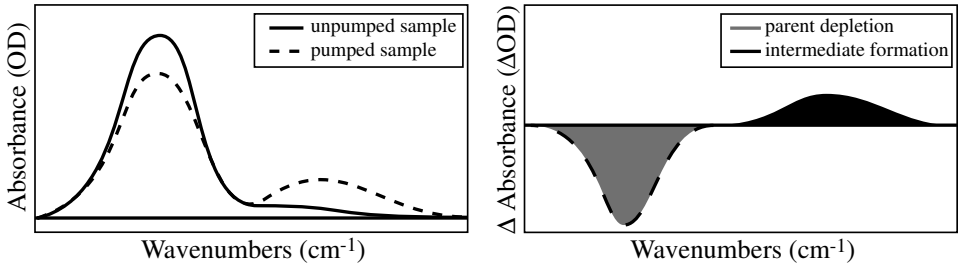

Figure 1.3. Difference spectra result from subtracting the unpumped sample from the pumped sample recorded at a given time after photoexcitation. Positive absorptions in the difference spectra correspond to intermediate and/or product formation and negative absorptions correspond to the depletion of parent molecules starting material.

formed after photoexcitation and negative absorptions for any parent complex absorptions. The negative absorptions are generally referred to as a parent bleach indicating the loss of parent molecules from the solution. A schematic representation of the procedure for constructing a difference spectrum is shown in Figure 1.3.

The basic principles of excitation and detection as described above are complicated at early times after photoexcitation because of the solvent environment. A couple of processes are worth explaining here since they are observed in all of the experiments discussed in this thesis. All of the infrared spectra collected at early times after photoexcitation (within the first 100 ps) display features indicative of vibrational relaxation. This energy redistribution has been extensively studied as a primary process in the early time dynamics of condensed phase photochemistry.(18; 19; 20) A brief description of this process is useful here in order to explain the spectral features that result.

The pump beam imparts an energy of 108 kcal/mol to the starting complex. The energy of a metal-carbonyl bond in a group 6 hexacarbonyl complex is approximately 30 kcal/mol.(21) Obviously, there is a large amount of excess energy in the complex after the dissociation of a single carbonyl ligand. In the gas phase, this excess energy results in the loss of additional ligands.(22) In the condensed phase, however, the excess energy is quickly distributed among the various vibrational modes of the complex and then transfered to the solvent. Although, additional carbonyl loss is not observed, the spectra are congested by the vibrationally excited transient species. Experimentally, this is seen as broad, red-

shifted (lower energy) peaks at early times that eventually narrow and blue-shift (higher energy). Figure 1.4 shows the spectra of $Cr(CO)_5$ in 1-butanol at increasing delay times after photoexcitation up to 100 ps. The line in the figure follows the maximum absorption point in the spectra. The peaks are broad because many vibrational levels are populated resulting in more transitions in a given frequency range. The peaks are red-shifted because the energy level spacing is smaller at higher energy (anharmonicity). The thermal distribution of vibrational states is recovered after some vibrational relaxation time that is characteristic of the solvent and solute species. In Figure 1.4, the peaks have reached their equilibrium positions and do not continue to narrow after about 35 ps. This timescale is often the limiting factor in the determination of early time dynamics because changes in the spectra are difficult to accurately observe until after this process has completed. When an important factor in determining reaction dynamics, vibrational relaxation will be discussed further in the appropriate sections of this thesis.

In addition to vibrational relaxation, geminate recombination is a ubiquitous process that is observable in many of the spectra shown in this thesis.(23; 19) Geminate recombination refers to the regeneration of starting material after excitation and can be classified as primary, secondary, or tertiary. Primary geminate recombination occurs when the dissociated carbonyl group recoordinates to the metal center before it can escape from the first solvent shell. In this case, the solvent shell serves as a physical barrier, keeping the dissociated ligand in close proximately to the unsaturated metal center. The timescale for primary geminate recombination is on the order of 100 fs. Secondary geminate recombination refers to the same type of process with the dissociated carbonyl ligand recoordinating to the same metal center from which it originated. The difference is in the timescale for the process, tens of picoseconds, which is a result of the ligand diffusing out of the first solvent shell and then back into the region where coordination can occur. Tertiary geminate recombination is diffusion limited, with a nano- to millisecond timescale, and occurs when any free carbonyl ligand diffuses into the solvent shell of an unsaturated metal center. The carbonyl group need not be the exact molecule that was originally dissociated. Experimentally, geminate recombination of all three types is observed as a decrease in the bleach signal. Since the parent bleach is a negative absorption, reflecting the loss of starting material, the reformation of parent complexes gives a smaller negative absorption over time. None of the experiments

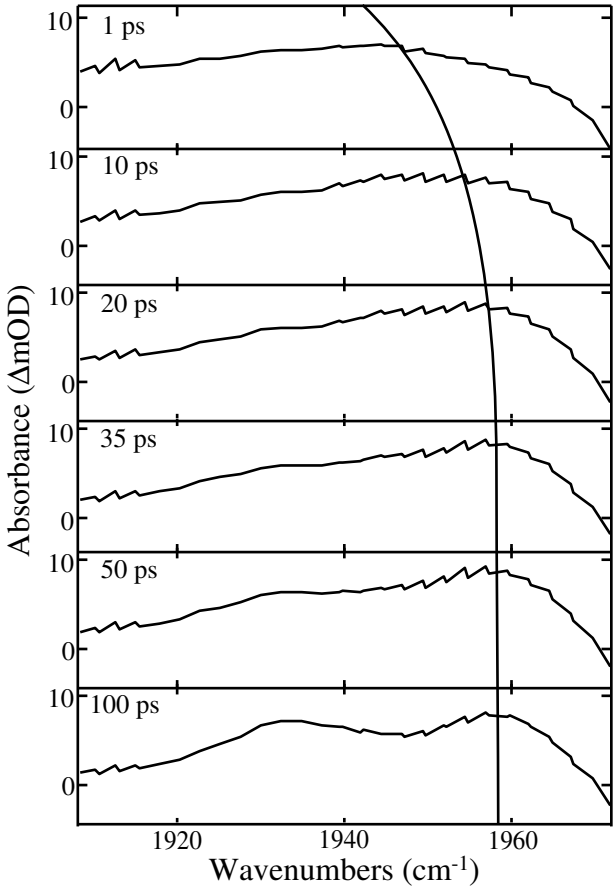

Figure 1.4. Difference spectra of chromium pentacarbonyl in neat 1-butanol up to 100 ps after photoexcitation. The solid line connecting spectra from different times is to aid in visualization. The broad peaks at early times blue shift and narrow. These features are indicative of vibrational relaxation.

described in this thesis are focused on the behavior of the parent species and, therefore, geminate recombination is not of primary significance in this work. As a common feature of all solution phase photochemistry, however, it is an important aspect of these experiments.

1.3 Computational Methods

One of the tools utilized in this work is density functional theory (DFT). Quantum calculations of the energetics of the complexes studied experimentally often aid in the assignment of absorptions and facilitate an understanding of the underlying dynamical processes. All of the theoretical calculations described in this thesis were performed using the Gaussian03 suite.(24) Becke's three-parameter exchange correlation energy(25) combined with the Lee-Yang-Par correlation functional,(26) B3LYP,(27) was used in all calculations. The basis set used for the main group elements consisted of the 6-311G** basis functions(28; 29) and the LANL2DZ core potential(30) was used for all of the central transition metals. Frequency calculations were carried out in order to ensure that optimized geometries corresponded to minima on the potential energy surface or saddle points indicating a transition state structure. All complexes were analyzed for signature infrared absorptions and energies. Frequencies were scaled by a factor of 0.9614 according to standard practice.(31) Calculated binding energies are the result of subtracting the single point energies of the fragments from that of the complex. This method includes a zero-point energy correction to the calculated binding energies, but does not maintain a consistent basis set and should, therefore, only provide an estimate of the interaction energy. These energy values are utilized to understand reactivity trends between similar molecules.

1.4 Sample Preparation

Unless otherwise noted in the relevant chapter, all samples were prepared using spectroscopic grade solvents and $M(CO)_6$ (M = Cr, W, Mo) purchased from SigmaAldrich. The metal-boryl compounds utilized in Chapter 5 were synthesized by Tim Boller and Marko Hapke in the John Hartwig group (Yale University). All solvents and metal carbonyl com-

plexes were used without further purification. Solutions were prepared by dissolving the metal hexacarbonyl complex in the solvent and stirring for 20-30 minutes. Samples were then filtered to remove any undissolved metal complex which could scatter incident radiation. The resulting solutions have a concentration of 10-20 mM which corresponds to an ultraviolet absorption of about 1 OD. The air sensitive samples in Chapter 5 required further sample preparation considerations and those will be discussed there.

1.5 Outline

This thesis describes a number of studies utilizing ultrafast, ultraviolet-pump, infrared-probe spectroscopy. Chapter 2 describes the details of the experimental apparatus including the construction of a tunable infrared source and the data acquisition hardware and software for the instrument. Chapter 3 investigates the first steps in the polymerization of alkyne complexes using organometallic catalysts. The findings of these experiments prompted an extensive investigation of complex ligand rearrangement. Both experiments and numerical simulations were aimed at gaining a more thorough understanding of these reactions and are described in Chapter 4. Chapter 5 is concerned with boryl-mediated bond activation reactions which behave catalytically and selectively. These studies represent a continuation of the theme of bond-activation which has been examined extensively in this research group. The first two projects described in this thesis (Chapters 3 and 4) are very similar in their focus and are aimed at understanding of the primary solvation process. The last project described (Chapter 5) uses these findings to explore a more complicated reaction sequence. As a whole, these studies represent three different systems in which ligand rearrangement is the primary photoprocess to explore in complex, condensed phase, organometallic chemistry.

Chapter 2

Experimental Methods

The experimental results outlined in this thesis were all obtained using a new ultrafast laser system. The solid state laser system used in these studies provides stable output and can be utilized to conduct experiments with little data collection time. The laser system is based on a commercially available titanium:sapphire oscillator that is regeneratively amplified. Details of the theory behind operation of the oscillator and regenerative amplifier can be found in the theses of Christine Payne(13) and Kenneth Kotz.(32) Initially, the system was constructed utilitizing single wavelength data acquisition. The broadband infrared light was sent into a monochromator and the single wavelength output was detected by two single element mercury cadmium telluride (MCT) detectors: one corresponding to the signal beam and one to the reference beam. Later, the monochromator was replaced by a spectrograph and the two single element detectors were replaced by a single 32x2 element MCT array detector. The array detector allows data collection at a much faster rate. First, 32 spectral points can be collected simultaneously. Second, the amount of time required for the monochromator to move from one wavelength to another is eliminated. This improvement has made it possible to study more unstable complexes such as the highly air-sensitive metal-boryl complexes discussed in Chapter 5. This chapter briefly describes the laser system and provides a detailed description of the optical parametric amplifier, signal/reference line setup, and the data acquisition software and hardware. The details of

the signal/reference line setup and the data acquisition setup described below are for the single element detection scheme. Details for the relevant parts of the laser system for the array detector are given in the thesis of Elizabeth Glascoe.(33)

2.1 Ultrafast Laser Apparatus

A schematic of the experimental setup is shown in Figure 2.1. The experimental apparatus consists of a Ti:sapphire regenerative amplifier (SpectraPhysics, Spitfire) seeded by a Ti:sapphire oscillator (SpectraPhysics, Tsunami) to produce a 1 kHz pulse train of 100 fs pulses centered around 800 nm with an average pulse power of 0.9 mJ. The oscillator is pumped by a neodymium doped yttrium orthovanadate (Nd:YVO_4) laser (SpectraPhysics, Millenia Vs J) and the regenerative amplifier is pumped by a neodymium doped yttrium lithium fluoride (Nd:YLF) laser. The output of the system is split and used for both harmonic generation of 266 nm pump pulses and to pump a home-built optical parametric amplifier (OPA) to deliver tunable mid-IR probe pulses. A computer-controlled translation stage (Klinger) allows for variable time delays between the pump and probe pulses.

The OPA routinely generates infrared pulses tunable from 3.0 - 6.0 μm with a spectral width of ca. 200 cm^{-1} and pulse durations of around 120 fs (see Section 2.2). The IR probe beam is split after the OPA into signal and reference lines using a 50% germanium beam splitter. The signal line is focused using a CaF_2 lens to provide a beam diameter at the sample of 100 μm. The pump beam is focused using a CaF_2 lens to a diameter of about 200 μm at the sample. The maximum power of the generated 266 nm light is 4 μJ, but can be reduced when required by specific experimental considerations. Using a mechanical pump, the sample is flowed through a cell (Harrick Scientific) fitted with 1.5 mm thick MgF_2 windows. The optical path length in the experiments described here was either 150 or 390 μm depending on the sample properties so that the optical density (OD) of the sample at the pump wavelength was about 1. The sample is moved perpendicular to the laser beam by computer-controlled translational stages (Standa) after each incident laser pulse to ensure that absorptions are not masked or enhanced due to burning effects, which result in secondary product accumulation on the cell windows.

The pump and signal beams are overlapped in space and cross-correlated using a silica wafer to identify time zero. The pulse width is measured to be 100-150 fs. In part of these experiments, reference and signal beams are sent through a computer-controlled spectrograph (Acton Research Corporation, SpectraPro-150) along a parallel path. The entrance slits on the spectrograph are routinely set at 35 μm to achieve a spectral resolution of ca. $\pm$1.5 cm^{-1}. Spectrally dispersed signal and reference beams are detected by a 2 x 32 element mercury-cadmium-telluride (MCT) array detector (InfraRed Associates, Inc.) and a high-speed signal acquisition system (Infrared Systems Development Corp.). In the low temperature alkyne experiments described in Chapter 3, reference and signal infrared beams were sent through a computer-controlled monochromator (CVI, Digikrom 240) with a spectral resolution of ca. $\pm$2 cm^{-1} at a slit width of 400 μm and detected by two single-element MCT detectors (Electro-Optical Systems). Collected signals are typically normalized over 1000 laser shots to account for shot-to-shot amplitude fluctuations of the laser. Differences in optical density (ΔOD) as small as 5 x 10^{-5} can be discerned with 1 s of signal averaging.

2.2 Optical Parametric Amplifier

The dynamical behavior of organometallic complexes is monitored using spectroscopic signatures of parent, transient, and product vibrational absorptions as described in Chapter 1. These vibrational transitions occur in the infrared region of the electromagnetic spectrum. Consequently, the ability to generate low-noise, tunable, infrared pulses of light is of primary importance. This is achieved through the use of an optical parametric amplifier (OPA). The construction of the OPA used in all experiments is outlined below. The basic principles of operation will be explained briefly followed by an discussion of the alignment process. A schematic of the instrument is provided along with descriptions of the optical components.

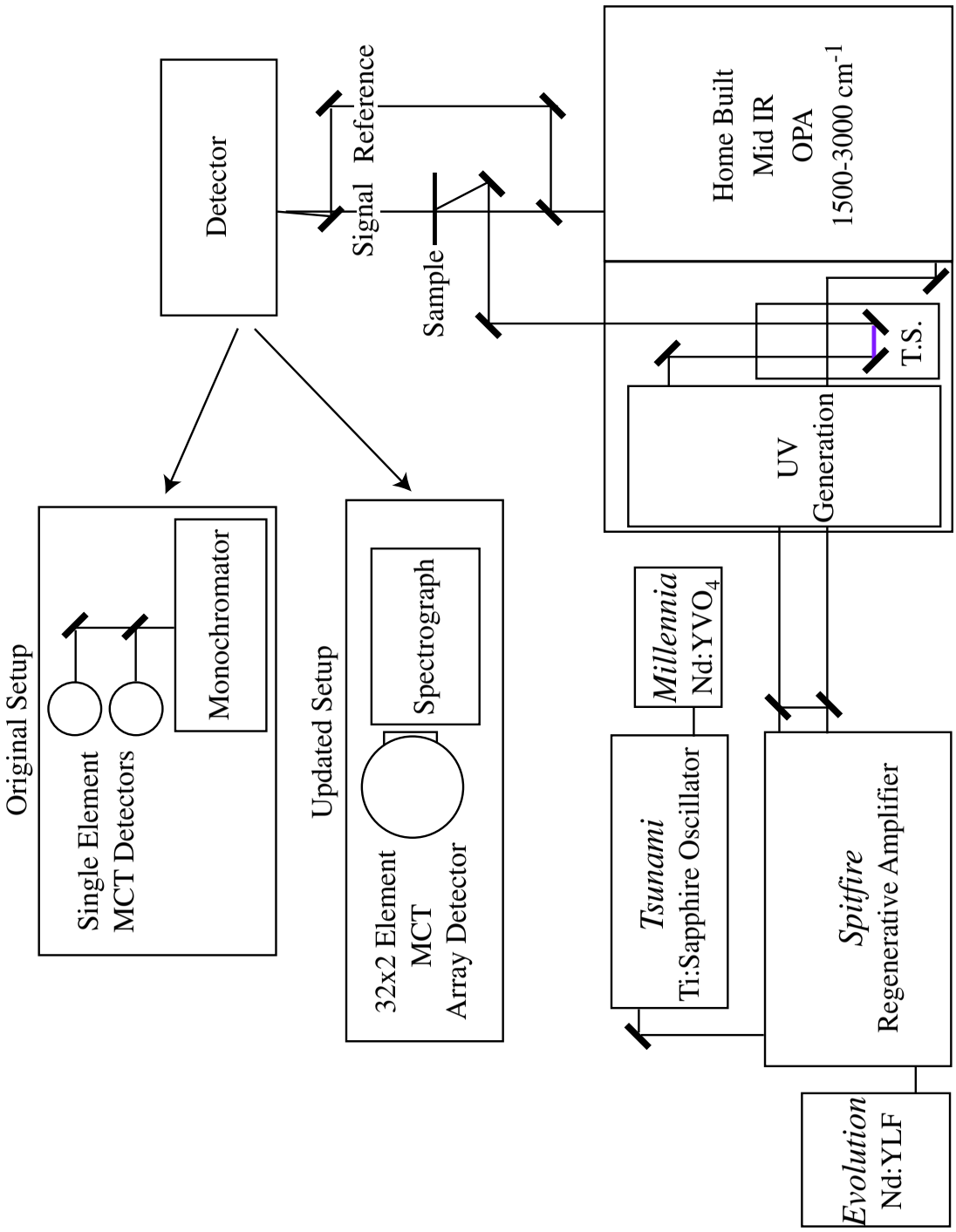

Figure 2.1. Diagram of the ultrafast pump-probe experimental setup. All components are labeled and discussed in the text. T.S. refers to the translational stage.

2.2.1 Operation Principles

The OPA constructed is based on the design of Peter Hamm's group.(34) Tunable mid-infrared light (3.0μm - 6.0 μm) is generated in two stages using two different non-linear crystals. As a three wave mixing process, the generation of infrared light relies on a property of the crystal, the second order nonlinear susceptibility ($\chi^{(2)}$). In a material with a sufficiently large $\chi^{(2)}$, difference frequency mixing can occur:

$$\omega_1 = \omega_2 + \omega_3 \tag{2.1}$$

where ω_1 is the pump beam, ω_2 is the seed beam, and ω_3 is the resultant beam. The process of difference frequency mixing can be an amplification process because the generation of a field with frequency ω_3 can interact with the pump field to produce a field with frequency ω_2 and vice versa. This process amplifies fields of both frequencies ω_2 and ω_3. For efficient conversion, the waves must remain in phase as they travel through the crystal; the phase matching condition must be met:

$$\mathbf{k_1} = \mathbf{k_2} + \mathbf{k_3} \tag{2.2}$$

where $\mathbf{k_i}$ is the wave vector of the field. Since the velocity of the electromagnetic wave as it travels through a material depends on its wavelength and the material index of refraction, it is necessary to use a birefringent material to ensure that no phase mismatch occurs. In a birefringent material, the material index of refraction that a given wave interacts with depends on its direction of propagation. In a uniaxial birefringent material, there is one axis, the optical axis, along which the index of refraction depends on the angle of incidence. One can use an index ellipsoid or indicatrix, Figure 2.2, to calculate the index of refraction and, consequently, the phase matching angle for a given material. In this picture, the z-axis is the optical axis of the crystal which is defined as the axis of cylindrical symmetry. The ordinary wave has a polarization vector that is perpendicular to the optical axis and the extraordinary wave has a polarization vector that is along the optical axis. When both waves are in collinear geometry, the phase matching condition is met when:

$$n_1\omega_1 = n_2\omega_2 + n_3\omega_3 \tag{2.3}$$

where n_i is the index of refraction of the material at a particular frequency and direction of propagation. With this equation and a selected pump and seed beam wavelength, one

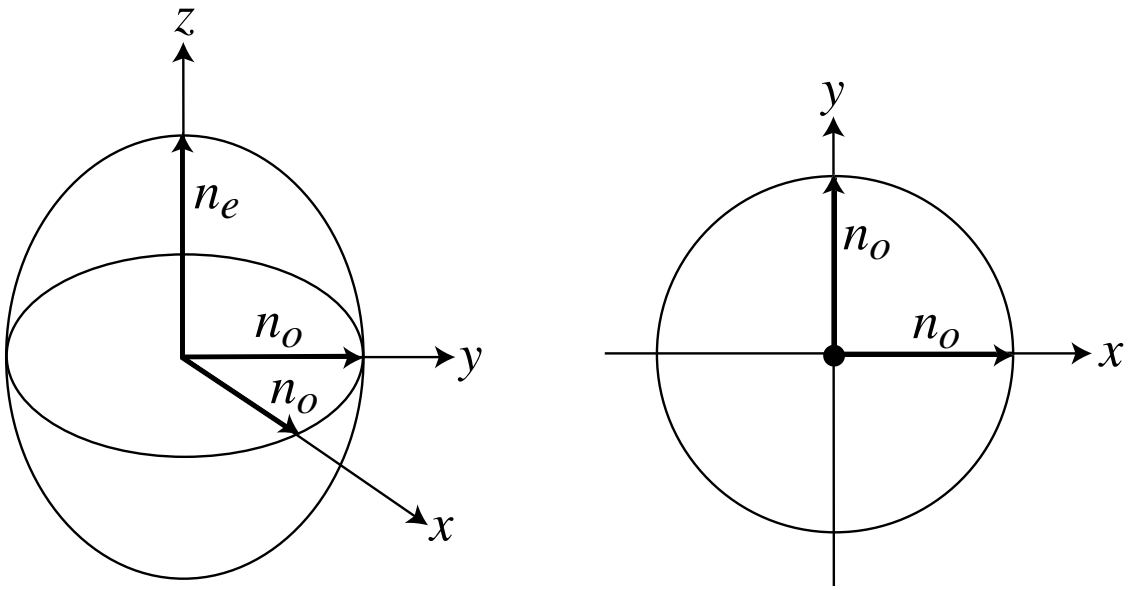

Figure 2.2. Index ellipsoid or indicatrix for a uniaxial, positively birefringent crystal. The z-axis defines the axis of cylindrical symmetry and is termed the optical axis of the crystal. The polarization vector of the extraordinary wave is along the optical axis and the polarization vector of the ordinary wave is in the plane perpendicular to the optical axis. In a positively birefringent crystal $n_o < n_e$ and in a negatively birefringent crystal $n_e < n_o$. A negatively birefringent crystal is used in the experiments described in this thesis, but a positively birefringent index ellipsoid is shown for simpler visualization.

can easily find the angle for which the indices of refraction appropriately meet this phase matching condition.

The operation of the OPA can be conveniently segmented into two stages. The first stage is the actual OPA using a Type II BBO crystal and the second stage mixes the two output beams of the OPA to generate mid-IR light using a Type I $AgGaS_2$ crystal. The first stage of the OPA consists of two passes of light through the BBO crystal. A weak (5μW) seed beam of 800 nm light is focused onto a thin sapphire window to generate a white light continuum after it passes through a half-wave plate. The white light is then directed into the BBO crystal where it is mixed with another focused weak (5μW) 800 nm pump beam. The crystal angle is manually adjusted to maximize the generation of near-infrared light, thus ensuring optimal phase matching conditions. The generated signal and idler beams

have the same polarization as the white light according to the condition:

$$E_o^{\omega_1} - E_e^{\omega_2} = E_e^{\omega_3} \tag{2.4}$$

where $E_x^{\omega_i}$ is the electric field of frequency ω_i polarized in the ordinary ($x = o$) or extraordinary ($x = e$) direction. According to convention, ω_1 is the pump beam, ω_2 is the seed beam referred to as the signal beam, and ω_3 is referred to as the idler beam. The signal and idler beams are separated using a dichroic mirror and the idler is removed from the OPA. This preamplification stage spectrally filters the signal beam which is collimated and sent back to the BBO to serve as the seed beam for the amplification stage. The pump beam in the second pass is collimated 800 nm light. Because the phase matching condition has been met for the pre-amplification stage, no further adjustment of the crystal is necessary for the amplification of the infrared beams. Efficiencies up to 20% can be achieved with this OPA.

The generated signal and idler beams have the same polarization and are separated again using a dichroic mirror. Each beam is directed onto a cylindrical mirror that is mounted on a translational stage which allows for adjustment of their temporal overlap in the second stage of the OPA. The signal and idler beams are recombined and focused onto the Type I $AgGaS_2$ crystal to generate mid-infrared pulses that are polarized in the same direction as the original pump beam:

$$E_e^{\omega_1} - E_e^{\omega_2} = E_o^{\omega_3}. \tag{2.5}$$

The conversion efficiency of difference frequency mixing in the $AgGaS_2$ crystal is 50%. Any unconverted near-infrared light is removed using a GaAs filter at the exit of the OPA setup.

2.2.2 Noise Reducing Features

The unique feature of this OPA is that it has been shown to reduce the shot-to-shot noise of the laser system. The commercial laser system utilized for the experiments described in this thesis has a typical rms noise of about 2%. The mid-IR light that is generated has a typical rms noise of about 1%. This noise suppression is achieved by adjusting the timing between the pump and seed beams in the amplification stage and the timing between the signal and idler beams in the $AgGaS_2$ crystal.

Both stages of the mid-IR generation need to be considered in the discussion of the noise suppression properties of this piece of equipment. The BBO OPA stage alone does not serve to reduce the shot-to-shot noise of the laser output. Operation of the amplifier is in the saturation regime, where some of the down-converted light regenerates the pump beam in a sum-frequency manner. Amplitude noise in the pump beam is carried through to the output signal and idler beams. Group velocity mismatch, resulting from different wavelengths of light traveling at different speeds through the crystal, causes the idler beam to exit from the crystal before the signal beam. Thus, noise also introduces time jitter (delay) between the beams. In the $AgGaS_2$ crystal, however, noise reduction is observed. The sign of the correlation between the energy fluctuation of the 800 nm pump beam and the energy of the generated mid-IR beam (calculated by Hamm et. al.) changes when the time between the two is altered. This correlation function provides an estimate of the ideal operating conditions for the difference-frequency generation. The idler pulse is set using a translational stage to arrive at the $AgGaS_2$ much later than the signal pulse; this ensures that maximum overlap occurs at the center of the crystal and results in the maximum down conversion efficiency. Again, this is a result of the group velocity mismatch of the beams in the $AgGaS_2$ crystal. Fluctuations in the intensity of the pump that have been carried over into fluctuations in the signal and idler are converted into spectral phase noise and the generated mid-IR is essentially noise free. A more detailed explanation of these features and theoretical simulations of these results can be found in the paper by Hamm et. al.(34).

2.2.3 Practical Outline

A schematic diagram of the OPA is shown in Figure 2.3. All of the optical components shown in the diagram are listed in Table 2.1. Sixty percent of the output from the regenerative amplifier is sent to the OPA. The input 800 nm light (approximately 600 μJ) is sent through a fused silica window (W_1) which reflects about 2% of the incident light. The reflected light is sent through a half-wave plate and used to generate the white light seed for the first pass of the OPA. White light generation is achieved by placing a thin sapphire window (W_2) in the focus of a telescope. A red, band-pass filter is placed after the second lens of the telescope for visualization purposes. The ability to generate high quality

white light is of primary importance for generating low-noise infrared light. The white light should be continuous and circularly symmetric and should be surrounded by a narrow ring of red light which indicates optimal alignment. In order to obtain high quality white light, it is often necessary to adjust the compression out of the regenerative amplifier along with the focal point of the beam onto the sapphire window. The white light is then centered at the bottom of the BBO crystal. The transmitted light is sent to a retroreflector and will be used as the pump beam for both passes of the OPA. The pump beam for the first pass of the OPA is generated by placing a second fused silica window (W_1) after the retroreflector. A second low intensity beam is reflected off of the window and focused onto the BBO using a 50 cm lens. The lens is placed onto a stage so that the focal point can be adjusted to compensate for variations in the laser power. The pump beam for the first pass should be focused before entering the BBO crystal. In practice, the focus should be as close to the crystal as possible without generating white light in the BBO which indicates an excessive intensitity in the crystal (and can lead to crystal damage). The white light seed beam and the weak, 800 nm pump beam are overlapped spatially and temporally in the crystal to generate infrared light. Optimization of the temporal overlap is achieved by adjusting the timing on the first translational stage. Spatial overlap is optimized by changing the seed beam path with the mirror just before the telescope and just after the wave-plate (M_1). The infrared light passes through a dichroic mirror (DM_1) and the signal and idler beams are separated by a second dichroic mirror (DM_2). The idler beam is removed with a beam block and the signal beam is sent to a convex mirror on a translational stage (M_3). The mirror has a focal length of 25 cm selected to recollimate the beam (in practice, the beam is generally not perfectly collimated). The signal beam from the first pass is the seed beam for the second pass of the OPA. The pump beam for the second pass is the remaining 800 nm light and is telescoped into the BBO in the center of the top portion of the crystal. Figure 2.4 shows the approximate position for both the pre-amplification and amplification passes through the BBO crystal. The beam diameter of the pump and seed beams should be similar when they are sent through the crystal and are spatially and temporally overlapped to generate amplified infrared light. The translational stage upon which M_3 is mounted can be adjusted for optimum temporal overlap to maximize the generated power and minimize the noise. Spatial overlap can be optimized by adjusting the position of the seed beam with

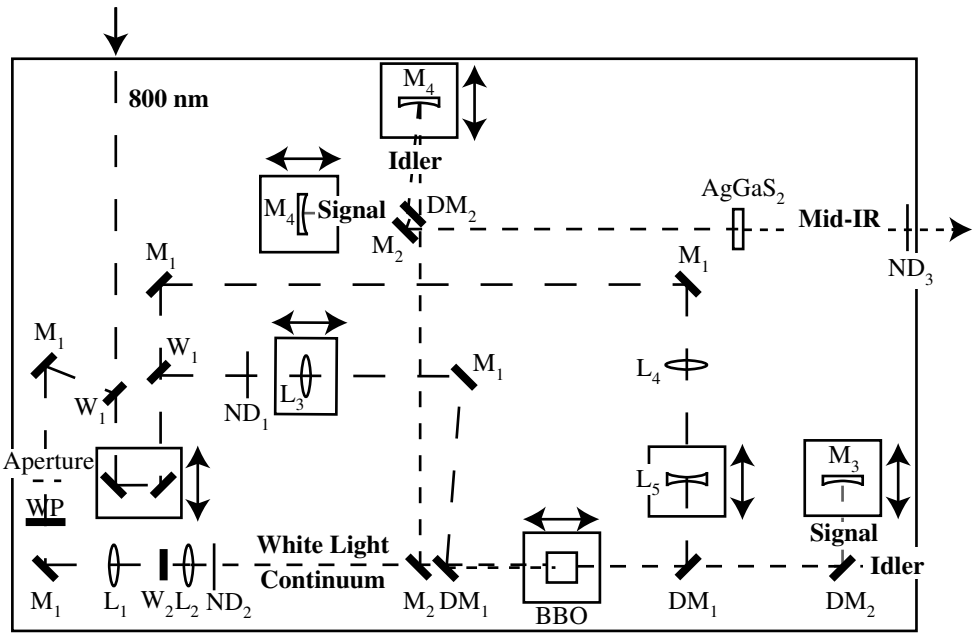

Figure 2.3. Diagram of the optical parametric amplifier (OPA) utilized in the ultrafast pump-probe experiments.

the translational stage mirror (M_3) and the dichroic mirror next to it (DM_2). The newly generated signal and idler beams are reflected off of a small gold mirror (M_2), split using a dichroic mirror (DM_2), and focused using two convex mirrors (M_4) onto a $AgGaS_2$ crystal for difference frequency mixing. Both convex mirrors are mounted on translational stages to optimize the temporal overlap of the beams. A filter (ND_3) is then used to adjust the infrared intensity and to remove any remaining signal and idler frequencies of light. The OPA can be tuned to a different frequency range by adjusting the angles of the BBO and $AgGaS_2$ crystals which changes the frequencies of light which are properly phase matched. In practice, this process is simplified by changing the center wavelength of the spectrograph and first adjusting the BBO crystal angle then the $AgGaS_2$ crystal angle to maximize signal. After iterating between the two crystals until no further increase in signal is observed, the spectrograph can be further adjusted and the process repeated until the desired wavelength range has been reached.

Label	Description
W_1	Fused Silica Window, D. = 1.0 in., 1.0 mm thick
W_2	Sapphire Window, C-Axis Cut, D. = 12.7 mm, 1.0 mm thick
WP	Waveplate, Zero Order, Half Wave, 800 nm, AR Coating
BBO	BBO Crystal, Type II, Size: 4x4x4 mm^3, P-Coating,
	Θ=28.9^o, Φ=30^o
$AgGaS_2$	$AgGaS_2$ Crystal, Type I, Size: 5x5x1.5 mm^3, P-Coating
	Θ=40.7^o, Φ=45^o
M_1	Broadband Low GVD Ultrafast Mirrors, 700-825 nm, D = 1.0 in.
M_2	Protected Gold Mirrors, 0.5 in. diameter, 0.375 in. thick
DM_1	Beam Splitter, D. = 1.0 in., CaF_2, R. at 800 nm, T. at 1.2-2.2 μm
DM_2	Beam Splitter, D. = 1.0 in., CaF_2, R. at 1.2-1.7 μmm, T. at 1.7-2.2 μm
M_3	Concave Mirror, D. = 1.0 in., F.L. = 25 cm
M_4	Concave Mirror, D. = 1.0 in., F.L. = 50 cm
L_1	Lens, BK7, D. = 30 mm, F.L. = 100 mm
L_2	Lens, BK7, D. = 30 mm, F.L. = 30 mm
L_3	Lens, BK7, D. = 42 mm, F.L. = 500 mm
L_4	Lens, BK7, D. = 30 mm, F.L. = 200 mm
L_5	Lens, BK7, D. = 30 mm, F.L. = -50 mm
ND_1	Red Band Pass Filter
ND_2	50% ND Filter
ND_3	Mid-IR Band Pass Filter

Table 2.1. Optical components of the optical parametric amplifier. Labels from Figure 2.3 and descriptions of all components are given. D. is the diameter, F.L. is the focal length, R. is reflective, and T. is transmissive.

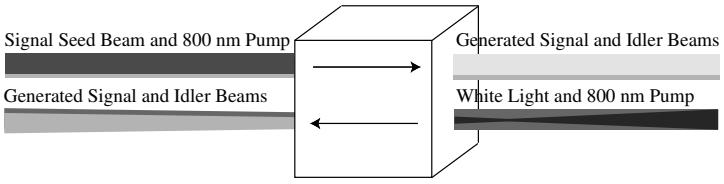

Figure 2.4. Schematic of the pre-amplification and amplification passes through the BBO crystal in the OPA. Arrows on the diagram indicate the direction of laser beam propagation.

2.3 Data Acquisition and Analysis

The data acquisition (DAQ) system is comprised of three main components: the analog sector, the digital sector, and the computer interface software. The analog portion of the system is comprised of sensors to convert the incident signal to voltages or current and a device to convert the voltages or current into a digital signal. In the system used here, mercury cadmium telluride (MCT) detectors are used to detect incident infrared light. The resulting electrical signal is converted into a digital signal and conditioned (filtered) using a multifunction input/output board (NI PCI-6115 S series, National Instruments). This board also serves as the digital sector allowing for timing, synchronization, and on board memory. The computer interface software is LabView and controls data acquisition, stage motion, monochromator/spectrograph position, and preliminary data analysis. Each of these components has important requirements which will be discussed in the following paragraphs.

The input/output board has a number of important requirements including sufficient on board memory, high sampling rates, synchronization capabilities, and enough independent channels for the application. The MCT detectors are connected to the DAQ card using a BNC connector block (BNC-2110, National Instruments). Two analog input channels (ACH0 and ACH1) are directly attached to each of two MCT detectors (signal and reference) with BNC cables. In addition, a trigger is supplied using a square wave from a pulse generator (Stanford Research Systems, Inc.) that is synchronized to the laser using the system trigger. The system trigger is supplied by the oscillator indicating that a laser pulse has exited from the oscillator cavity; this trigger has a 1 kHz repetition rate and drives the

generation of the square wave at a 500 Hz repetition rate. The square wave will be used to indicate whether a collected spectrum is chopped (the pump beam has been blocked) or unchopped (the pump beam is incident on the sample) for each infrared spectrum collected. The DAQ card features a shared external clock that is used to correlate the analog and digital signals. Since three inputs are needed for each shot (signal, reference, and chopper), the clocking capabilities of the card are vital to the application. The card can accept up to four analog inputs and eight digital inputs. The analog inputs have 10 MS/s data acquisition with a 32 MS buffer which is sufficient for acquiring the pulse profile of our 1 kHz laser system. A GPIB interface card (AT-GPIB/TNT, National Instruments) is used to control the translational stage and the monochromator is directly connected to the computer when it is in use.

The LabView program controls all aspects of data collection and control. In the single element detector configuration there are two programs: one collects spectral data and one collects kinetic data. The reason for the use of two programs is sample decay; in the kinetic program, a single wavelength is monitored at varying delay times to minimize the effects of sample degradation on the kinetic traces. In the spectral program, a spectrum at a single time slice is collected before moving through the stage positions. In this way, one can obtain a physical representation of the peak intensity ratios (spectral scan) and the kinetic behavior of each individual infrared feature (kinetic scan). The complexity of the LabView program inhibits its inclusion in this thesis. The basic principles of the spectral program are outlined below. The kinetic program is almost identical except that the stage positions (time delay) are read in from a file which is looped through while the wavelength remains constant.

The first step in the program is to initialize the monochromator and to move the stage to the correct position. The monochromator is connected directly to the computer (COM 1) and the stage is interfaced as a GPIB instrument. The program now enters a loop which collects each spectral position. The index of this loop is based on the size of the spectral input file. The program then waits for a trigger which is the square wave from the function generator which is triggered by the laser. The device (DAQ board) is then configured for analog input with a large buffer. The buffer is set to be as large as possible (100,000

samples) so that no information is overwritten after the data collection begins. The internal clock is then disabled and a new clock is configured (scan clock 1) to obtain a maximum rate of collection. The board is then set up to collect 100,000 scans (or points) for each trigger obtained. The *Retrigger Configure* sub vi is then utilized to set up the counter to retrigger. This is important because a trigger should be received every millisecond (1 kHz laser repetition rate). Once the board has been set up, data is read and placed into an array. For each point collected the user selects a preset number of shots to be collected (default is 1000 shots). The program is looped through for each wavenumber position given in the input file. The resulting data array will contain three data sets: the signal, the reference, and the chopper signal for each wavenumber in the spectral file. After data collection is complete, the task and triggers are cleared. After collecting the data, it is sorted, analyzed and written to an output file. First, the data is pulled out of the two dimensional array. The signal data is divided by the reference data for each spectral point (cm^{-1}) collected. Points are then compared to determine if there are any outliers which are determined using the standard deviation value (1-3) selected by the user. The value from the chopper array is then used to determined whether the point is a chopped or an unchopped. Chopped data is divided by unchopped data. The negative log of this value is then calculated according to the Beer-Lambert law. The average value from a preselected number of laser shots (default is 1000) is then written to a file along with the wavenumber value from the monochromator.

The output from the LabView program is manipulated by a Matlab program that was written for single element data collection. This program is necessary in order to average together multiple scans that have been collected for a single experiment. Again, two programs exist for the data analysis: one for the spectral data and one for the kinetic data. These programs read in all of the files and conduct a small amount of error analysis. The data is averaged and a standard deviation for each point is calculated. Any extreme points are thrown out based on the number of standard deviations given as an input. Plots of the data and output files can be generated by the user. An example input file and the Matlab program for kinetic data are given in Appendix 1.

Chapter 3

The Interaction of 1-Hexyne With Group 6 Hexacarbonyl Complexes

3.1 Introduction

The coordination of unsaturated hydrocarbons to transition metal complexes is important to both fundamental and industrial applications due to the essential role these complexes play in the synthesis of hydrocarbon products.(9) Examples of such reactions include polymerization, metathesis, and cyclo-oligomerization.(35; 36; 37) Knowledge of the mechanistic details of this coordination is the key to controlling such reactions, providing for the possibility of selective functionalization. Many of the reactions involving the complexation of unsaturated hydrocarbons to transition metal centers are thought to proceed via the formation of a vinylidene metal species. Particular interest has centered on the photoinduced coordination and rearrangement of transition metal carbonyl complexes, such as $M(CO)_6$ (M = Cr, Mo, W) with terminal alkynes.(38; 39; 40)

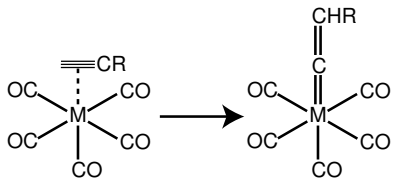

Figure 3.1. Schematic representation of the tautomerization from the π-bonded alkyne complex to the vinylidene-metal complex.

Upon photodissociation of a single carbonyl ligand from a parent metal hexacarbonyl complex, the first step in many condensed phase reactions is the interaction of the unsaturated metal center with a neighboring solvent molecule.(15; 16) In terminal alkyne solutions, this solvation is thought to yield a π-bond coordinated complex which rearranges to the vinylidene species as shown in Figure 3.1. Previous ultrafast studies on group 6 metal hexacarbonyl complexes in alcohol and silane solutions, however, revealed that solvation is more complex and may involve initial coordination at any site of a functionalized solvent molecule with subsequent rearrangement to a more stable configuration.(41) Specifically, with a functionalized hydrocarbon, the initial coordination may be to an alkyl site followed by rearrangement to a complex that is coordinated to a more electron rich group on the hydrocarbon. Although considerable interest has focused on the coordination and rearrangement of transition metal complexes with terminal alkynes, a clear consensus on the mechanistic details of the reaction has not yet been reached. The original mechanism proposed for the photoinduced reaction of metal carbonyl complexes with terminal alkynes is based on low-temperature matrix studies.(42; 10; 11) These experiments yielded information about possible intermediates formed in the photoinduced reaction, but because these experiments were conducted at low temperatures in glassy matrices, solvent effects were not explicitly studied and the initial coordination steps could not be investigated.

Experimental and theoretical results obtained in other work suggest that the formation of a vinylidene species is highly dependent on the particular chemical system studied. Electron spin resonance (ESR) measurements have focused on the rearrangement of $[Cr(CO)_2(\eta^2\text{-}Me_3\text{-}SiC{\equiv}CSiMe_3)(\eta\text{-}C_6Me_6)]$ to its vinylidene analogue.(43) The rate constant was measured to be $k = 0.31\ s^{-1}$ at room temperature indicating a high barrier for

the thermal reaction. Other recent work on metal-carbonyl complexes $M(CO)_5$=C≡CR (M = Cr, Mo, W) utilizing steady-state infrared and NMR spectroscopic techniques suggests an equilibrium between the π-bonded complex and the corresponding vinylidene species, while the former is thought to be thermodynamically favored.(44) The vinylidene complex could only be isolated with trapping methods in this case. In contrast, DFT calculations carried out by De Angelis and co-workers on $Cp(PMe_3)Ru(HC{\equiv}CR)$ suggest that the vinylidene species is energetically favored over the π-bonded complex by 13.1 kcal/mol.(45)

The group 6 metal carbonyl complexes, $M(CO)_5$–HC≡CR (M = Cr, Mo, W); R = C_4H_7), studied in this work are expected to undergo a similar type of tautomerization(46) from a π-bonded complex to a vinylidene metal complex. Interestingly, the formation of the vinylidene species in the photochemistry of $M(CO)_6$ complexes in terminal alkynes has been attributed to thermal effects(47) and/or sequential photoexcitation.(10; 11) In light of these ambiguities, a femtosecond infrared study of the photoinitiated reaction of $M(CO)_6$ (M = Cr, Mo, W) in neat alkyne solutions was carried out in order to clarify the mechanism. This technique can follow reaction dynamics on the time scales (femtoseconds to nanoseconds) over which they occur in ambient solutions.

In addition to expanding the understanding of the mechanism of vinylidene formation, the current experiments aim to further the understanding of rearrangements for metal-carbonyl complex in coordinative solvents. All previous experiments have focused on the rearrangement of the π-bonded complex to the vinylidene complex without any consideration of the initial solvation. The primary steps of coordination and rearrangement are not yet understood and should provide important mechanistic details of the process. To the best of our knowledge, no study has yet been carried out on the solvation and rearrangement dynamics of transition metal carbonyl complexes in unsaturated hydrocarbon solutions.(48)

3.2 Experimental Results and Mechanistic Explanation

Ultrafast UV-pump, IR-probe experiments were carried out for each of the group 6 metal hexacarbonyl complexes: $Cr(CO)_6$, $Mo(CO)_6$, and $W(CO)_6$. The spectra obtained for a room-temperature solution of $Cr(CO)_6$ in 1-hexyne at increasing delay times after

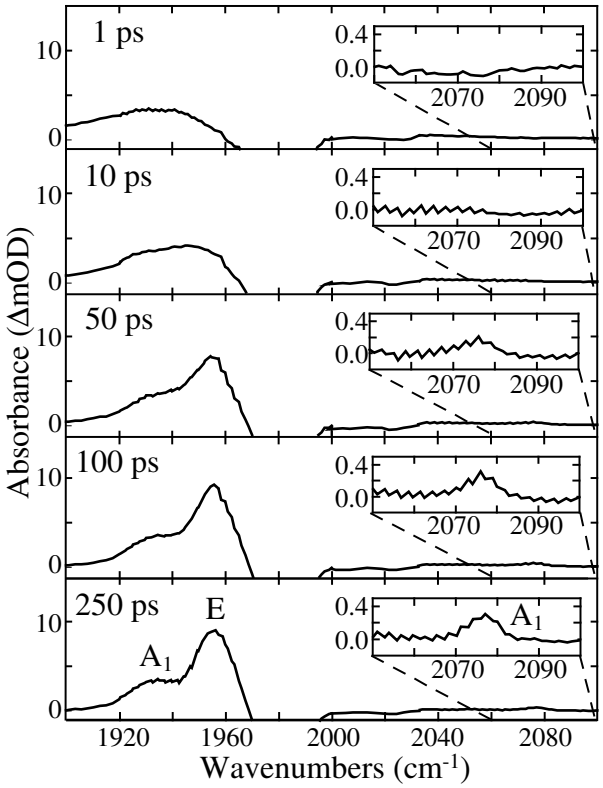

Figure 3.2. $Cr(CO)_6$ in 1-hexyne at increasing delay times after photodissociation of a single carbonyl group. The three peaks evident at 250 ps remain unchanged for the remainder of the experimental time (up to 1 ms). Absorptions at 1929 and 1960 cm^{-1} are the A_1 and E bands of the initially solvated species. The small absorption at 2076 cm^{-1} is the A_1 band of the π-bound species. Small oscillations in the data are the result of collecting two spectra offset by 1 cm^{-1} from one another and interleaving them together.

photoexcitation are shown in Figure 3.2. All three metal hexacarbonyl species demonstrate the same qualitative behavior.

Inspection of the time-resolved spectra for $Cr(CO)_6$ in 1-hexyne after photoexcitation shows a parent bleach at 1987 cm^{-1} indicating the depletion of parent species due to carbonyl loss. The bleach is excluded from the spectra in Figure 3.2 for improved visualization. The appearance of broad peaks in the spectrum at the earliest time delay time of 1 ps indicates the formation of a vibrationally excited, solvated complex in agreement with the solvation times for other metal carbonyl complexes in solution (see Ch. 1).(15; 16; 17; 18)

peak assignment	$Cr(CO)_6$-L	$Mo(CO)_6$-L	$W(CO)_6$-L
A_1	1929	1935	1933
E	1960	1962	1957
A_1	2076	2085	2086

Table 3.1. Peak positions for ultrafast experiments (in wavenumbers(cm^{-1})) for all three metal complexes: Cr, Mo, W. Errors for peak positions are ± 2 cm^{-1}.

Solvation here refers to the interaction of the metal center with a molecule from the bath without specifying between the modes of the complexation. Vibrational relaxation is observed via the narrowing and shifting of the peaks until they reach their equilibrium absorption frequencies of 1929, 1960, and 2076 cm^{-1}. The relevant equilibrium spectral features and their symmetry labels for all three complexes are given in Table 3.1.

To provide assignments for the observed peaks, it is necessary to consider all possible outcomes of the initial solvation. Two effective bonding arrangements are available for 1-Hexyne: in a σ-bonded fashion to one of the alkyl sites of the alkyl chain or in a π-bonded fashion to the triple bond of the alkyne. The DFT optimized geometries of the two possible complexes as well as the vinylidene complex are shown in Figure 3.3.[1] The three structures are labeled as **1**, the σ-bonded complex; **2**, the π-bonded complex; and **3**, the vinylidene complex, and will be referred to as such throughout the remainder of this chapter. The calculated absorption frequencies of complexes **1** and **2** are given in Table 3.2 and agree well with the previous experimental trends shown in Table 3.3.(10; 11) Also shown in Table 3.2 are the calculated relative peak intensities for all of the absorption frequencies. The peaks at 1929 and 2076 cm^{-1} correspond to two A_1 bands, and the peak at 1960 cm^{-1} corresponds to the E band of the solvated species with local C_{4v} symmetry. These assignments do not distinguish between the two possible solvated intermediates, but are general, as the local symmetry of both complexes is the same. The calculated absorption frequencies for all bands of **1** and **2** are very similar and cannot, therefore, be used alone to uncover the mechanistic details of the reaction. It is important, however, to note that the calculated

[1]In the calculations, 1-propyne has been used in place of 1-hexyne for more efficient computation.

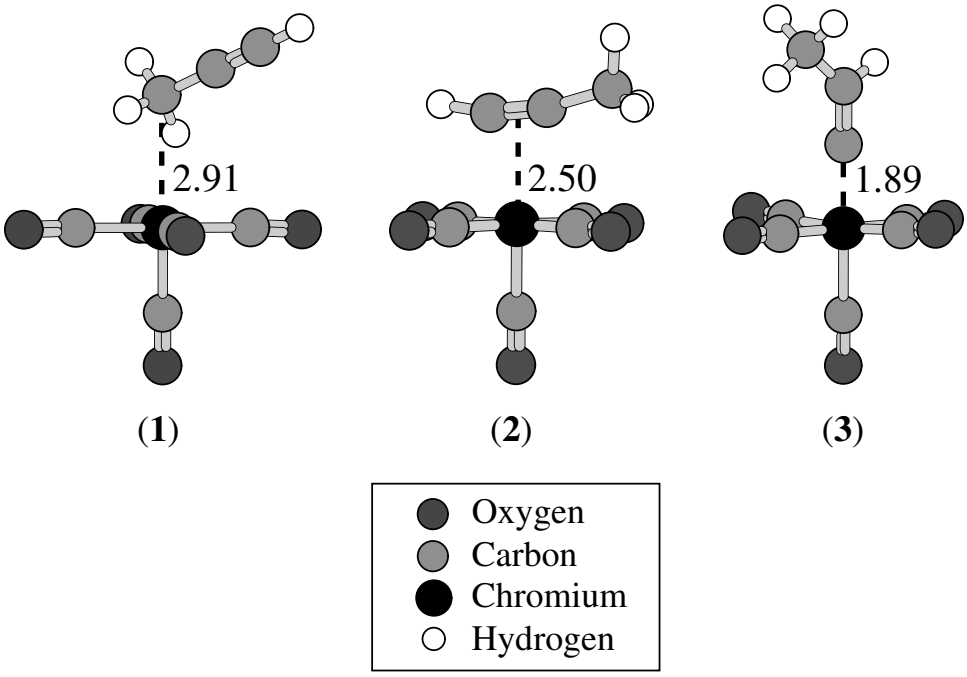

Figure 3.3. Optimized geometries of the σ-bonded intermediate (**1**), the π-bonded intermediate (**2**), and the vinylidene complex (**3**). All calculations were done using 1-propyne for calculation simplicity. Bond lengths (in Å) are shown for the metal-alkyne interactions.

absorption intensity of the A_1 band around 2080 cm^{-1} is four times as large for **2** than it is for **1** in the chromium complex.

Additional relevant information is gained through inspection of the kinetic traces for the transient absorptions. Shown in Figure 3.4 are kinetic traces for the E band centered at 1960 cm^{-1} and A_1 band centered at 2076 cm^{-1}. A kinetic trace of the A_1 band at 1929 cm^{-1} is not shown because the early time dynamics are obscured by the vibrationally hot population of the E band as can be seen in the early time spectra shown in Figure 3.2. The traces show first-order kinetic behavior in all cases. The rise times for the chromium complex absorptions at 1960 and 2076 cm^{-1} were found to be 45.8 $\pm$ 3.8 and 68 $\pm$ 12 ps, respectively. Table 3.4 summarizes the time constants that result from first-order kinetic fits for all three metal-carbonyl complexes. The significant difference between the time constants for the two peaks indicates that different kinetic processes are occurring. The shorter time constant, 45.8 $\pm$ 3.8 ps, is a measure of the vibrational relaxation time of the

complex	peak assignment	$Cr(CO)_6$-L	$Mo(CO)_6$-L	$W(CO)_6$-L
1	A_1	1965.7 (0.24)	1953.2 (0.24)	1950.2 (0.24)
	E	1982.4 (1.00)	1979.1 (1.00)	1969.4 (1.00)
	A_1	2078.9 (0.01)	2080.9 (0.01)	2078.8 (0.02)
2	A_1	1961.7 (0.28)	1955.5 (0.26)	1955.7 (0.22)
	E	1966.7 (1.00)	1964.9 (1.00)	1964.4 (1.00)
	A_1	2064.2 (0.04)	2069.4 (0.03)	1072.3 (0.04)

Table 3.2. Calculated frequencies (in cm^{-1}) for complexes **1** and **2** for all three metals: Cr, Mo, and W. Normalized absorption intensities are given in parentheses.

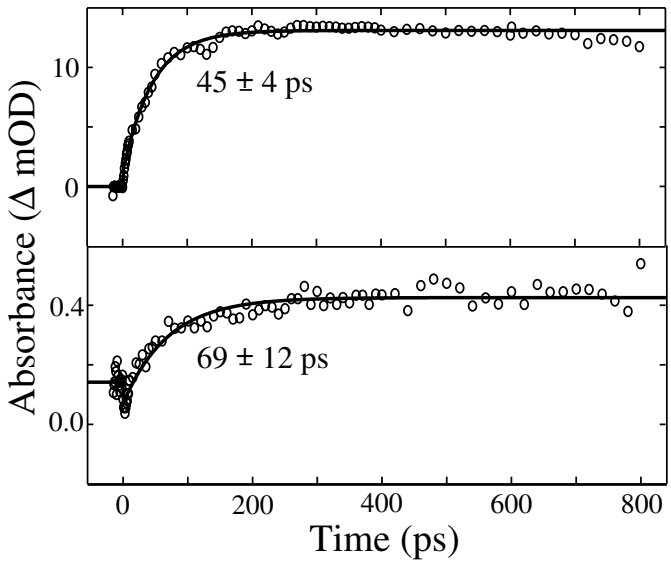

Figure 3.4. Kinetic traces for $Cr(CO)_5$ in 1-hexyne: (a) E band centered at 1960 cm^{-1}; (b) A_1 band centered at 2076 cm^{-1}. Open circles represent experimental data and lines represent fits to the data with time constants shown.

complex	peak assignment	$Mo(CO)_6$-L	$W(CO)_6$-L
1	A_1	1927 (m)	1926
		1930 (m)	
	E	1969 (vs)	1957.5
		2092 (w)	2092
2	A_1	1945 (w)	1950 (w)
	E	1968 (vs)	1978 (m)
	E	1974 (s)	
	A_1	2088 (w)	2093 (w)
3	E	2000 (w)	
	A_1	2078 (w)	
		2074 (w)	

Table 3.3. Experimental carbonyl absorption frequencies from previous low-temperature matrix studies (in wavenumbers (cm^{-1})) for Mo and W.(10; 11) Complex **1** in this table is the methane coordinated complex from the methane-matrix experiments. Absorption intensities are given in parenthesis where available, with w = weak, m = medium, s = strong, and vs = very strong. Bands for which two frequencies are listed are the result of splitting by matrix side effects.

	E band	A_1 band
$Cr(CO)_6$	45 ± 4	70 ± 10
$Mo(CO)_6$	42 ± 3	90 ± 10
$W(CO)_6$	28 ± 6	40 ± 10

Table 3.4. Rise time constants (in ps) obtained from single-exponential fits of $M(CO)_5$ in 1-hexyne for the E band centered around 1960 cm^{-1} and the A_1 band centered around 2080 cm^{-1}. Errors are 95% confidence intervals.

	A (cm^{-1})	τ (ps)	Γ (cm^{-1})
$Cr(CO)_6$	3.0 ± 0.5	42.5 ± 6.6	6.0
$Mo(CO)_6$	12.5 ± 3.2	32.5 ± 7.7	7.0
$W(CO)_6$	7.0 ± 2.0	34.3 ± 9.1	9.8

Table 3.5. Vibrational relaxation fitting parameters for $M(CO)_6$ in 1-hexyne. The long time width (Γ) is fixed according to the spectra in all cases.

E band of the initially solvated complex and contains information about both species **1** and **2** due to their strong spectral overlap. To verify this statement, the vibrational relaxation time was estimated using the product band narrowing method.(49) A Gaussian function was chosen to fit the spectra in order to obtain peak width estimates. The variation of the peak width over time was fit according to the relationship

$$\delta v_{abs}(t) = [(A \exp^{-t/\tau} + \Gamma)^2 + (IRF)^2]^{1/2} \tag{3.1}$$

where Γ is the long-time width, A is the additional width, τ is the cooling time, and IRF is the instrument response or resolution (2 cm^{-1} here). Table 3.5 gives the fit parameters for all three metal-carbonyl complexes according to an analysis of this type. The vibrational relaxation times agree well with the values obtained by fitting the rise time of the E band. Additionally, the time scale for vibrational relaxation measured here falls within the range of previously reported values, 5-50 ps.(17; 18)

We propose that the longer time constant, 68 ± 12 ps, measured for the A_1 band centered at 2076 cm^{-1} is solely representative of complex **2**. The small peak does not shift or narrow as it increases in intensity, indicating that the time constant is not a measure of vibrational relaxation of the A_1 band. Instead, this long time constant represents the amount of time required for the rearrangement of complexes of type **1** to complexes of type **2**. Previous work has demonstrated that a coordinated alkyl group can be best described as a 'token ligand' which interacts weakly with the metal center.(50; 51; 52) If a stronger interaction is possible, as in the case of a terminal alkyne via the π-bond, then rearrangement to the thermodynamically favored product results. Thus, in 1-hexyne, any σ-bound complex (**1**) will eventually rearrange to the π-bound complex (**2**). Figure 3.5 shows the proposed

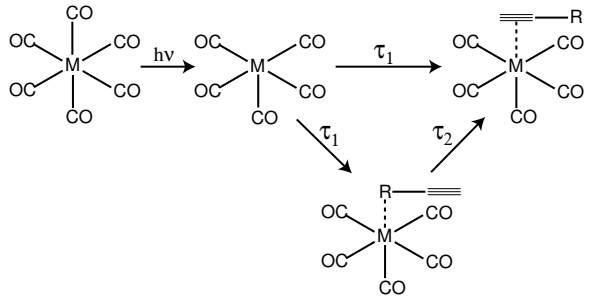

Figure 3.5. Proposed rearrangement reaction for $M(CO)_6$ in 1-hexyne. After photodissociation of a carbonyl ligand, the unsaturated metal center is solvated by any site along the alkyne in one of two bonding configurations. Eventually, rearrangement will occur to convert any σ-bound complexes (**1**) to π-bound complexes (**2**).

rearrangement mechanism. The E band absorption is insensitive to the rearrangement because both **1** and **2** exhibit a large peak at this frequency; any decay in the absorption from **1** is concomitant with an increase in the absorption from **2**, resulting in no net absorbance change.

An important piece of information in assigning the longer time constant to the rearrangement process as described is the relative intensities of the absorption of the A_1 band around 2080 cm^{-1} (Table 3.2). These values indicate that although the absorption frequencies are very similar for **1** and **2**, the intensities of these absorptions differ. To identify which solvated product is responsible for the experimentally observed absorption, a comparison can be made between the experimental peak ratios and the calculated peak ratios for each of the possible solvated species. In the chromium experiments, the peaks at 1929, 1960, and 2076 cm^{-1} have calculated oscillator strength ratios of 24:100:1 for **1** and 28:100:4 for **2**. The experimental peak ratio at long delay times after photoexcitation is 28:100:4 in excellent agreement with the calculated ratio for **2**. The use of relative absorption intensities has been extensively tested for transition metal complexes and has been verified to qualitatively reproduce experimental data.(53; 54; 55)

To verify the absence of an absorption for **1** in the region around 2080 cm^{-1}, the experiment was repeated in neat hexane under otherwise identical conditions; no absorption band was observed in the region around 2080 cm^{-1} (i.e., $< 50\mu$OD). In fact, in linear

alkane solutions, the A_1 band absorption around 2080 cm^{-1} has not, to our knowledge, been observed experimentally in ambient solutions. Experiments in cyclohexane, however, have reported the observation of a weak absorption at 2087 cm^{-1}.(56) DFT calculations on hexane- and cyclohexane-solvated metal fragments indicate that the cyclohexane-solvated species has an absorption in this region that is three times as intense as the hexane-solvated species. Thus, the calculated peak ratios and experimental observations are in excellent agreement with the alkyne solvated calculations.

3.3 Comparison of Group 6 Metal Coordination in Terminal Alkynes and Alcohols

The rearrangement of group 6 metal carbonyl complexes in 1-hexanol, as studied previously in the Harris group, is analogous to that of alkyne rearrangement and provides an ideal point of comparison. In the case of 1-hexanol, rearrangement occurs until the metal fragment coordinates to the hydroxyl group of the alcohol, at which point the rearrangement ceases.(41) For $Cr(CO)_6$ in room-temperature hexanol, the time scale for the rearrangement from an alkyl site to the final hydroxyl coordinated site is 1.8 ns, while the hexyne rearrangement is observed to occur on a time scale of 67 ps. Although this difference appears striking at first glance, it is most likely due to differences in the viscosity of the two solvents in conjunction with the variation in interaction energy. 1-Hexanol exhibits a viscosity of 6.00 cP,(57) while 1-hexyne has a much lower viscosity of 0.34 cP.(58) According to the high friction limit of Kramer's theory,(59) the time constant of a reaction is proportional to a friction term that is related to the bulk viscosity via Einstein's diffusion relation and Stoke's law.(60) A more viscous solvent will result in a longer rearrangement time since the local solvent motions are smaller. The applicability of the bulk solvent viscosity in such a rearrangement process finds broad precedence in a variety of experiments.(61)

3.4 Comparison of the Rearrangement Times for the Group 6 Metal Hexacarbonyls

While recent work has indicated that rearrangement is an intermolecular process,(41; 62; 63; 64; 65) there is no consensus on the details of the mechanism. Conventionally, rearrangement reactions of the type discussed here are described as associative, dissociative, or dissociative interchange.(66) Recent calculations using the method of transition path sampling(67) have suggested that a dissociative interchange mechanism is the most general and best description of ligand exchange reactions. Associative and dissociative mechanisms are the two extremes of the dissociative interchange mechanism. In the associative extreme, there is partial coordination of a surrounding solvent molecule followed by dissociation of the coordinated ligand. In this limit, rearrangement time scales for the three transition metal systems would be expected to correlate with the binding energies of the complex to alkynes in its more stable configurations (**2**). In the dissociative extreme, the coordinated ligand dissociates before a new species from the surrounding solvent can coordinate. The dissociative interchange mechanism is a hybrid of these two possibilities, where a solvent from the surrounding bath weakly interacts with the metal center at the same time as the coordinated ligand starts to dissociate.

While all three hexacarbonyl complexes, $Cr(CO)_6$, $Mo(CO)_6$, and $W(CO)_6$, demonstrate the same rearrangement behavior, time constants for the initial solvation and subsequent rearrangement from **1** to **2** differ. The time scales for the three metals and the mechanism of rearrangement can be understood in the context of the proposed mechanism by comparing the binding energies for each of the three metal complexes to an alkyne molecule in complexes **1** and **2**. The calculated bond dissociation energies for metal-alkyne interaction for the binding of acetylene to $Mo(CO)_5$ (M = Cr, Mo, W) are shown in Table 3.6.(68) Also shown in Table 3.6 are the experimental binding energies of alkanes to $M(CO)_5$ (M = Cr, Mo, W).(21) $W(CO)_5$ clearly forms the strongest bond with both the alkane and the alkyne and also coordinates on the fastest time scale; $Mo(CO)_5$ and $Cr(CO)_5$ have binding energies that are much weaker and coordinate on longer time scales. There is an anticorrelation between the bond strength and the rearrangement time. This behavior is

	$Cr(CO)_5$-L	$Mo(CO)_5$-L	$W(CO)_5$-L
L = C_2H_2	19.6	18.0	25.3
L = C_7H_{14}	9.6±2.3	8.7±2.7	13.4±2.8

Table 3.6. Binding energies (in kcal/mol) of $M(CO)_5$ to acetylene and heptane. Binding energies to acetylene are calculated values (68) and to heptane are experimental values.(21)

indicative of an associative mechanism, where the rate constant for the rearrangement from species **1** to species **2** is expected to be proportional to the binding energies. A purely dissociative mechanism can be ruled out directly since the metal with the weakest interaction with the alkane in structure **1** would be expected to dissociate most readily. Rearrangement would then occur on the fastest time scale for the weakest interaction in direct contrast with the time constants measured for this rearrangement process. A mechanism with mainly associative character is in agreement with the experimental data. However, as suggested previously, a dissociative interchange mechanism may be the best possible description of this process.

3.5 Effects of Chainlength on Reaction Dynamics

In order to determine the effect of chainlength on the rearrangement dynamics, experiments for all three metal carbonyl complexes were conducted in 1-butyne at 200 K.[2] A corresponding set of experiments in 1-hexyne was done at 200 K in order to ensure that any observed behavior could be correctly attributed to either solvent or temperature effects. The spectral features of the 1-butyne experiments are in agreement with the room temperature 1-hexyne experiments. Spectra for $Cr(CO)_6$ in 1-hexyne and 1-butyne at 200 K are shown in Figure 3.6 at 700 ps after photoexcitation. Figure 3.7 shows the kinetic traces for the E band of the coordinated complex of $Cr(CO)_5$ in 1-butyne (a) and 1-hexyne (b) at 200 K.

[2]The boiling point of 1-butyne (8°C) precludes the possibility of conducting room temperature experiments.

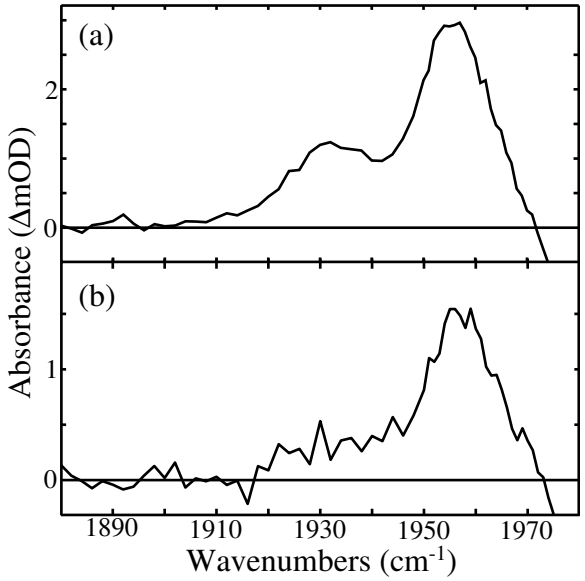

Figure 3.6. Spectra of $Cr(CO)_6$ in 1-butyne (a) and in 1-hexyne (b) 700 ps after photoexcitation at 200 K.

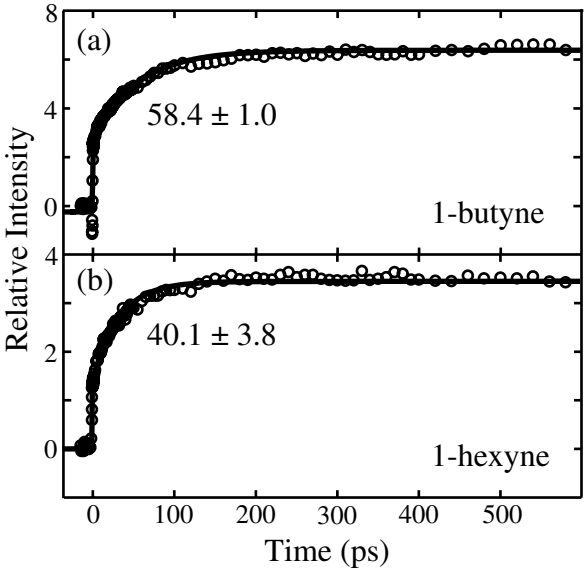

Figure 3.7. Kinetic traces for $Cr(CO)_5$ in 1-butyne (a) and 1-hexyne (b) at 200 K. Experimental data is shown as open circles and the exponential fit to the data is shown as a solid line. Errors in time constants are 95% confidence intervals.

	$Cr(CO)_5$-L	$Mo(CO)_5$-L	$W(CO)_5$-L
L = 1-butyne	58.4±1.1	79.4±2.1	33.4±3.3
L = 1-hexyne	40.1±3.3	47.4±3.0	37.8±1.3

Table 3.7. Rise time constants (in ps) obtained from single exponential fits of the data at 200 K obtained for the E band of the $M(CO)_5$-L complex (M = Cr, Mo, W; L = 1-butyne, 1-hexyne). Errors are 95% confidence intervals.

The relevant time constants for all metal carbonyl complexes in 1-hexyne at 200 K are given in Table 3.7. A comparison of the solvation times (rise times) at the two different temperatures shows little variability. The most notable difference is that the time constant for tungsten rearrangement is slightly longer. The primary difference between the systems at the different temperatures is the viscosity. Since the viscosity does not change significantly over this temperature range and is not an important factor in the initial solvation step, the small change in time constants is reasonable. Unfortunately, due to the decreased solubility of the metal carbonyl complex at 200 K, the dynamics of the absorption at 2076 cm^{-1} could not be measured. Consequently, the time constants measured for 1-hexyne at 200 K only represent the initial solvation of the unsaturated metal center with a bath molecule and are not sensitive to the rearrangement.

Time constants for the solvation of $M(CO)_5$ by 1-butyne are also given in Table 3.7. The experimental time constants for the kinetic traces in 1-butyne are longer than those in 1-hexyne, but shorter than the rearrangement times in room temperature 1-hexyne (refer to Table 3.4). Because the kinetic data for $M(CO)_5$ in 1-butyne and 1-hexyne at 200 K were collected using a single element detection scheme, it is important to consider the information contained in the kinetic data. In the room temperature data, kinetic traces represent the area under a peak. Since peaks from **1** and **2** are overlapping in the 1960 cm^{-1} region, the area of the peak will encompass both processes. In the 200 K experiments, however, kinetic traces are the result of collecting data at a single wavelength over time. As a result, it is possible to collect data at a region of the peak that contains a larger contribution from one complex over the other. In other words, it is possible that we are isolating the rearrangement in the cold 1-butyne experiments and not in the other experiments. The

comparison of the time constants in cold 1-hexyne and room temperature 1-hexyne leads us to this conclusion.[3]

The timescale for rearrangement in 1-hexyne is slower than in 1-butyne because of the difference in the solvent and the binding energy of the metal fragment to the alkyne. A slight decrease in the time required for the rearrangement in 1-butyne is consistent with the rearrangement dynamics as described above. The shorter alkyl chain in 1-butyne means that there are fewer alkyl sites with which the unsaturated metal center can coordinate. Thus, rearrangement will be faster for the 1-butyne complex because fewer alkyl sites will be sampled before a stable π-bonded complex is formed.

3.6 Vinylidene Formation

According to early proposed mechanisms for the photoinduced chemistry of metal hexacarbonyls in alkynes, triple-bond coordinated complexes (**2**) eventually tautomerize to the corresponding vinylidene complex (**3**). According to the spectral evidence provided by our experiments, the formation of a vinylidene complex does not occur on the ultrafast time scale. Previous work in low-temperature matrices assigns two peaks to the vinylidene species. For the tungsten complex these peaks are at 2002 and 2079 cm^{-1} and correspond to the E and A_1 bands of the complex, respectively. Due to possible spectral overlap with the triple-bond coordinated complex, the peak at 2079 cm^{-1} cannot be used in our studies to directly indicate whether the tautomerization to a vinylidene complex occurs on the ultrafast time scale. The intensity of this absorption, however, is expected to be at least 5 times more intense that the corresponding absorption of **2** according to DFT calculations and previous experiments.(39; 10; 11) No increase in this absorption is observed after the measured rearrangement time. Further, the peak at 2002 cm^{-1} is a peak of substantial intensity (comparable to the A_1 peak at 1929 cm^{-1} for complex **1**) that should be easily discernible in our time-resolved IR experiments if present. None of the three metals studied in the present work display such a feature. Finally, if a rearrangement of **2** to **3** were

[3]These experiments could be redone using the current experimental setup which includes the array detector to verify these statements. Such experiments were not done because of the difficulty of the experiment and the limited information that they would provide.

occurring, the kinetic traces for the A_1 and E bands on the red side (lower energy) of the bleach should decay; no decay is observed. The lack of a strong absorption at 2080 or 2002 cm^{-1} and any observable kinetic changes in the other absorption frequencies of **2** lead to the conclusion that tautomerization to the vinylidene species does not occur under the conditions of these experiments on the time scales that we have investigated.

Preliminary studies were carried out using a step- and rapid-scan FTIR experiment in collaboration with Heinz Frei's laboratory(69) to investigate the rearrangement behavior of the triple-bond coordinated complex (**2**) on the nanosecond to millisecond time scale. The presence of a vinylidene complex was not observed in the spectra collected, shown in Figure 3.8. The same spectral features present in the ultrafast data are observed in the long-time data without change. In fact, these experiments show no dynamical behavior. The experimental observation that no vinylidene complex forms on the millisecond time scale indicates that the free energy barrier to this tautomerization is at least 13 kcal/mol. DFT calculations done by De Angelis and co-workers(45) for $M(CO)_5HC{\equiv}CCH_3$ (M = Cr, Mo, W) indicate that the highest transition states in the lowest energy pathway for the tautomerization from **2** to **3** exhibit barriers of 21.7 (W), 22.6 (Cr), and 23.3 kcal/mol (Mo). Furthermore, the reaction is found to be slightly endothermic with 2.4, 5.2, and 6.9 kcal/mol for W, Cr, and Mo, respectively (reaction enthalpies include zero-point and thermal energy corrections for 298 K), thus favoring an alkyne coordination (**2**) over vinylidene coordination (**3**) for the transition metal complexes studied here.

Our findings conflict with earlier observations in low-temperature matrix studies.(42) Thermal tautomerization from **2** to **3** is expected to be negligible at low temperatures, yet matrix experiments indicate high yields of **3**. A sequential photon mechanism in which **3** is formed from **2** via the absorption of an additional photon may explain such an observation as was originally presented in matrix studies.(10; 11) Such a mechanism would not be seen in the ultrafast experiments described here since the applied pulses of light are much shorter than the formation time of **2**. In contrast, continuous irradiation of the sample may result in the formation of the vinylidene species and explain the high yields observed in the matrix studies.

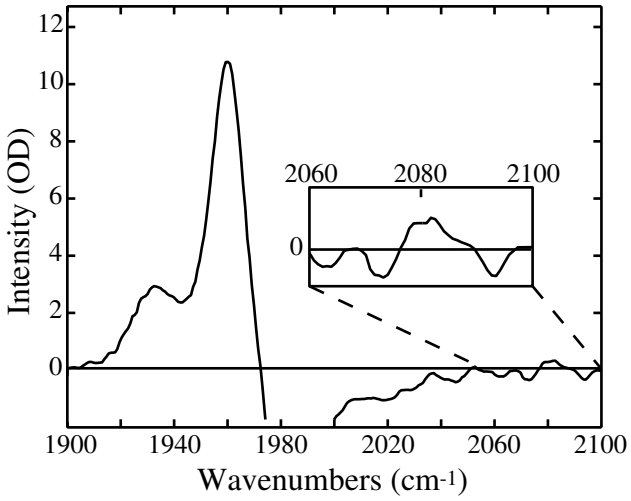

Figure 3.8. Step-scan spectra of molybdenum hexacarbonyl in neat 1-hexyne 1 microsecond after photoexcitation. The inset shows the region of the spectrum where the π-bonded complex is observed.

3.7 Conclusions

We have investigated the mechanism of coordination of terminal alkynes to metal carbonyl complexes of the type $M(CO)_6$ (M = Cr, Mo, W). The initial steps in the solvation of a coordinatively unsaturated metal center are consistent with previous studies of linear alcohols and silanes. In unsaturated hydrocarbons, this process involves the initial coordination of a neighboring solvent molecule followed by rearrangement to a more stable, π-coordinated complex. On the basis of experimentally measured rates of rearrangement and calculated binding energies, a dissociative mechanism can be ruled out in favor of an associative or dissociative interchange mechanism for the rearrangement of terminal alkynes coordinating to transition metal complexes. In these experiments, tungsten forms the strongest bond to the alkyne and was found to rearrange on the fastest time scale. Additionally, we investigated the role of chainlength on the rearrangement process and found that 1-butyne rearranges on a faster timescale than 1-hexyne in agreement with the proposed mechanism of rearrangement.

The tautomerization of a π-bonded complex to its vinylidene analogue was not ob-

served on the femtosecond to millisecond time scale, indicating a significant barrier to the tautomerization. These results were verified using DFT calculations. Future experiments could be carried out to investigate the possibility of a sequential photon process for the tautomerization from an alkyne- to a vinylidene-coordinated complex. This would require an alteration of the experimental setup to allow for the controlled excitation of the complex at two defined times before monitoring with infrared light.

Chapter 4

Alcohol Rearrangement Reactions

4.1 Introduction

The studies of group 6 hexacarbonyl complexes discussed in Chapter 3 found that the rearrangement dynamics were important first steps in the formation of the vinylidene precursor. These studies were compared with previous work on the rearrangement of metal-carbonyl complexes in silanes and alcohols. In fact, such reactions are ubiquitous because they involve both the fundamental solvation of photochemically prepared transient species and the rearrangement of such species to synthetically important products. In general terms, ligand exchange describes any reaction in which a bound ligand is traded for another ligand molecule of the same or of different chemical composition. Traditionally, such reactions are given mechanistic descriptions of dissociative, associative, and dissociative interchange(66) as was done in Chapter 3. Many other researchers have focused attention on determining the most appropriate label for a specific reaction sequence using kinetic data, but such determinations are complicated by the similarity in the kinetic behavior observed for these

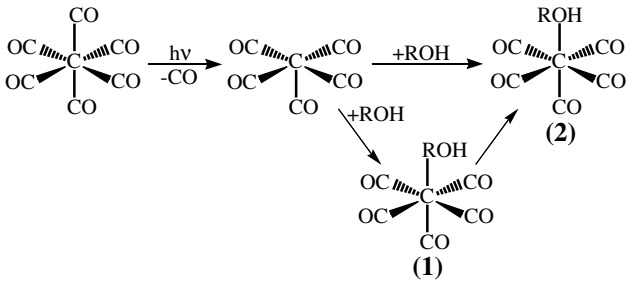

Figure 4.1. Photochemical reaction of chromium hexacarbonyl in a neat alcohol solution after photoexcitation. The first solvated species can be either alkyl (1) or hydroxyl (2) solvated. Eventually, all alkyl solvated complexes will become hydroxyl solvated species.

three processes. In fact, it is questionable whether or not such a distinction is possible with ensemble measurements.(70)

A similar focus has been directed toward linkage isomerization reactions where the solvent molecule offers more than one bonding site to the unsaturated metal.(71; 64; 72) This is exactly the interaction that was observed for group 6 metal hexacarbonyls in alkyne solutions, Chapter 3. In this chapter, we examine the dynamics of linkage isomerization reactions of $Cr(CO)_6$ in neat alcohol solutions. Upon photoirradiation, the unsaturated metal center is solvated within 1-2 ps to form a species that is bound to either one of the alkyl groups or to the hydroxyl group. The interaction between the metal center and the alkyl group is weak and rearrangement from the alkyl bound complex to the hydroxyl bound complex is observed as shown in Figure 4.1. The alkyl interaction itself is an instructive starting point for understanding the nature of the rearrangement.

When a Group 6 metal pentacarbonyl is prepared in a neat alkane solution, the alkyl group serves as a 'token' ligand in which the interaction between the metal center and the alkyl solvent is very weak.(52) These complexes have been observed in ambient solutions using a variety of techniques including infrared spectroscopy and nuclear magnetic resonance (NMR). NMR studies have indicated that the interaction is not static and that the alkyl site which is bound to the metal center changes with time.(73) In a neat alkane solvent, this weakly solvated complex continues to exist in solution until a carbonyl group diffuses into

the first solvation shell. The more strongly binding carbonyl group will replace the weakly bound alkyl solvent resulting in regeneration of the parent species.

In an alcohol solution, however, the hydroxyl group serves as a stronger binding site and will always be in close proximity to the metal center. Consequently, the weakly solvated alkyl-metal complexes will eventually turn over into the thermodynamically more stable hydroxyl solvated complexes before diffusive motion brings a carbonyl group in close contact to the metal center. At times after the initial solvation, but before the final product formation, the various alkyl sites of the solvent can be sampled by the metal center. As a result, reactions of this type will have dynamics that reflect this exchange: longer chain alcohols will have final product formation time constants that are much longer than short chain alcohols. For example, $Cr(CO)_6$ in neat ethanol forms the hydroxyl solvated complex within 25 ps while $Cr(CO)_6$ in neat hexanol forms a parallel complex in approximately 1.8 ns, as measured previously by our group.(74) The sampling of alkyl sites is a central aspect of the microscopic nature of these reactions.

Instead of simply characterizing the mechanism as dissociative, associative, or dissociative interchange, it has been suggested that such a reaction should be considered in terms of inter- versus intramolecular rearrangement. Two general mechanistic paradigms have been presented in the literature to explain the mechanism of this rearrangement process. The intramolecular chainwalk mechanism, depicted in Figure 4.2, is one common description of this reaction.(72; 75) The initial binding of a solvent molecule in the first 1-2 ps after photolysis is expected to be random as described above. If the initial solvation is to an alkyl site, the molecule will rearrange by walking along the alkyl backbone until it reaches the hydroxyl site, terminating the rearrangement. Alternatively, an intermolecular mechanistic description, depicted in Figure 4.3, has been suggested where the initially solvated metal complex rearranges through exchange with a new solvent molecule.(41; 76; 64) This process can occur via an associative, dissociative, or dissociative interchange mechanism. The newly bound complex, however, will be bound to a different solvent molecule in some random orientation or position along the alcohol chain. This can be considered a stochastic process since the sampling of solvent sites is expected to be random in contrast to the more

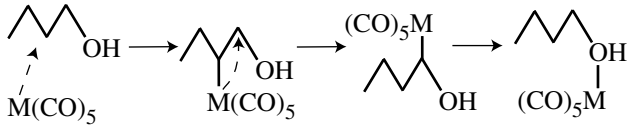

Figure 4.2. Schematic representation of the intramolecular rearrangement or chainwalk mechanism.

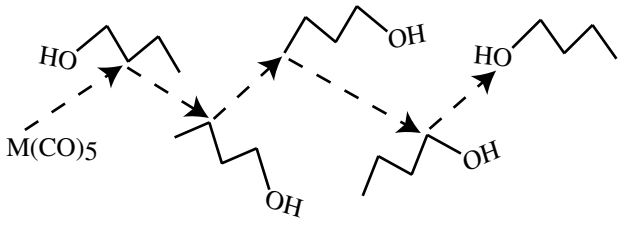

Figure 4.3. Schematic representation of the intermolecular rearrangement or stochastic mechanism.

systematic chainwalk mechanism. The stochastic rearrangement ends when a hydroxyl site is eventually found as in the chainwalk description.

In order to gain a more definitive understanding of the particular form of the rearrangement mechanism it is necessary to determine whether the two standard descriptions are actually distinguishable from each other. Toward this end, we have undertaken a comprehensive study of this reaction employing both experiments and numerical simulations. The numerical simulations of the dynamics for both the stochastic and chainwalk mechanisms are based on the Langevin equation. Such simulations have been utilized for a variety of chemical processes that range from simple isomerization reactions(77) to protein folding dynamics.(78) The underlying physical picture for these simulations is that the solvent serves as an energy bath to facilitate the chemical change. The fluctuating force is related to the friction coefficient which is characterized by the solvent viscosity which is derived from the microscopic fluctuations of particle velocity, as discussed below. These simulations therefore utilize a bulk property to characterize the microscopic details of a chemical reaction.

This work uses these techniques to model complex organometallic rearrangement dy-

namics for the first time and compares the results to ultrafast, ultraviolet pump, infrared probe experimental data. These simulations are, to our knowledge, the first aimed at elucidating the nature of this ubiquitous rearrangement process. We demonstrate that these two models are nearly indistinguishable due to the broad distribution of initial sites and the highly diffusive nature of the reaction which results in a large sampling of sites for both mechanistic descriptions.

4.2 Data Fitting Methods

Both alkyl and hydroxyl solvated species are observed in the experimental data. It is therefore possible to consider the spectra in long chain alcohols as the sum of contributions from the two different solvated metal species. Raw spectra from $Cr(CO)_6$ in pentane and $Cr(CO)_6$ in methanol were used in the determination of time constants for $Cr(CO)_6$ in each alcohol. The spectra of $Cr(CO)_6$ in pentane and $Cr(CO)_6$ in methanol at a given time were each multiplied by a constant value and added together according to the following expression:

$$\nu(\tau_i)_{ROH} = A * \nu(\tau_i)_{methanol} + B * \nu(\tau_i)_{pentane} \tag{4.1}$$

where $\nu(\tau_i)$ is the spectrum of the alcohol or pentane at delay time τ_i and A and B are adjustable parameters. An example of a fit for 1-butanol using this method is shown in Figure 4.4. Methanol was used to fit the hydroxyl peak because spectra of $Cr(CO)_6$ in methanol only show a hydroxyl solvated complex at all delay times after photoexcitation; no rearrangement is observed. Values of A and B were determined using a χ-squared optimization routine to fit the spectrum of the alcohol of interest with the sum of the spectra of methanol and pentane at the same time slice. This was repeated for all of the experimental time slices. This method allowed for the minimization of vibrational relaxation and overlap effects which served to mask the absorptions. The values of the constants were plotted against the time at which the spectra were taken and fit using either a single or double exponential function to measure the rise of the absorption due to hydroxyl solvation and the decay of the absorption due to alkyl solvation. The kinetic data obtained in this fashion were compared with raw experimental traces and were found to agree well

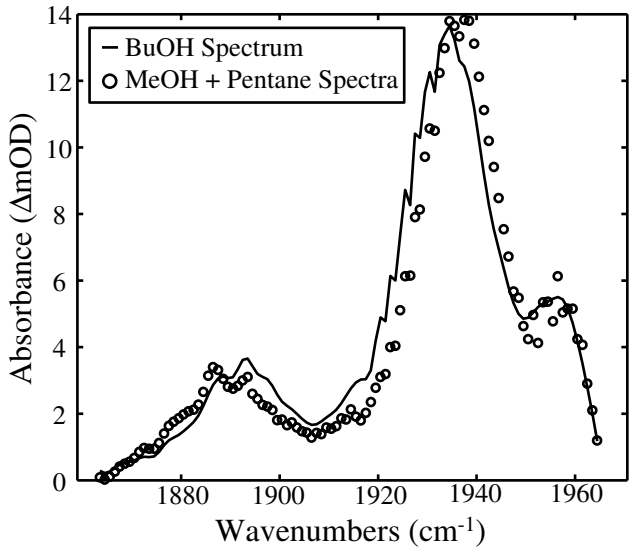

Figure 4.4. Spectrum of $Cr(CO)_5$ in 1-butanol 700 ps after photoexcitation (solid lines) overlaid with the sum of spectra from $Cr(CO)_5$ in methanol and pentane (open circles). The fitting routine adjusts for intensity, but does not incorporate shifts in the absorption frequency. Differences in the absorption frequency of 5 cm^{-1} are encountered due to solvent differences.

numerically, but with decreased scatter (less noise) as expected. A comparison of the raw kinetic data to the kinetic data from fitting is shown in Figure 4.5. All kinetic data given for long chain alcohols are the result of this fitting routine. All other data, including spectra, are raw data. Errors in the exponential fits to the data are 95% confidence intervals.

The Langevin simulation results were analyzed in sets of 500 trajectories each. Each set was binned according to the amount of time required for each particle to become trapped in the hydroxyl well. The number of hydroxyl solvated products was plotted against time and the data were fit using a single exponential function. This was done independently for 10 trajectory sets (5000 trajectories total). The reported errors in simulation time constants are derived from the standard deviation of those fit constants over the 10 sets.

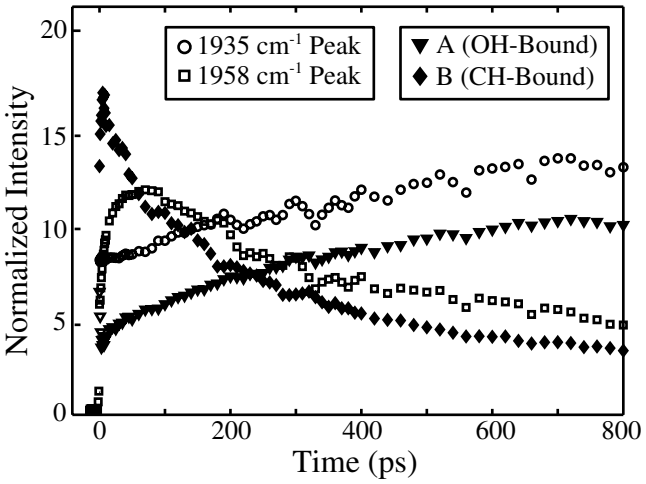

Figure 4.5. Comparison of kinetic traces resulting from Equation 1 (solid diamonds and triangles) and raw data (open circles and squares) for 1-butanol. The exponential rise (hydroxyl solvated species) and decay (alkyl solvated species) are well reproduced. The early time vibrational relaxation is minimized by utilizing equation 1 and the rearrangement dynamics are isolated.

4.3 Model Details

Condensed phase reaction dynamics have many unique properties derived from their environment. One such property, energy exchange through collisions, is exploited in the simulations carried out in the current investigation. Here a solvated metal center can become unsaturated if the metal-ligand binding energy is weak enough to be perturbed by collisions from the bath. The binding energy of heptane to $Cr(CO)_5$ has been experimentally measured by Burkey and coworkers using photoacoustic calorimetry to be 9.8 $\pm$ 2.2 kcal/mol.(79) Thus, the rearrangement from a weakly bound alkyl complex to a strongly bound hydroxyl complex is considered in the context of energy exchange with the bath.

We model the system of intermolecular exchange using diffusive motion over a barrier. The barrier is defined according to the binding energy of the specific carbon or hydroxyl group that the metal can coordinate to; this value is calculated using DFT as explained in the Chapter 1. For calculation simplicity, we construct a 1-D potential using a cosine function (from 0 to π). The well depth is adjusted so that it has a maximum value of zero

		Binding Energy (kcal/mol)				
Alcohol	M-OH	M-C_α	M-C_β	M-Cγ	M-C_δ	M-C_ϵ
1-propanol	16.53	5.62	5.22	3.71		
2-propanol	15.69	5.47	4.26	4.26		
1-butanol	16.40	5.43	5.07	3.27	3.67	
2-butanol	15.50	5.47	4.87 3.14	3.84		
isobutanol	16.21	5.22	5.43	3.54		
1-pentanol	16.42	5.47	5.14	2.90	3.37	3.89
2-pentanol	16.51	5.51	4.66 3.19	2.84	3.96	
2-methylbutanol	16.65	5.55	4.88	3.58 4.11	4.04	
3-methylbutanol	16.61	5.84	5.64	4.10	3.96	

Table 4.1. Table of metal-ligand binding energies calculated using density functional theory. Labels for the various alkyl sites on the alkyl chain represent the distance from the hydroxyl site. Entries with multiple binding energies are found for asymmetric branched alcohols.

and a minimum value that corresponds to the bond energy of the metal fragment with the alcohol site of interest. Table 4.1 gives the calculated bond energies for all of the solvent systems studied. The width of the potential well is set to be 3.0 Å for each of the sites; this value corresponds to the average distance between binding sites along the alcohol. The 1-D potential surface used for 1-butanol is shown in Figure 4.6. A more complicated model for the potential of mean force will affect all of the binding sites and will, therefore, change the overall rearrangement time but should not affect the trend when comparing different solvents. Since these simulations are aimed at uncovering the trend in rearrangement times for a number of alcohol solutions, they are not expected to give exact agreement with the experimentally obtained time constants and a more complicated model for the potential energy surface is not needed.

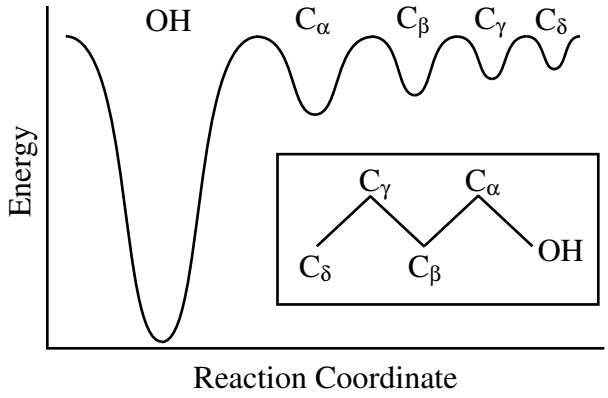

Figure 4.6. One-dimensional potential energy surface used in the simulation of rearrangement dynamics for $Cr(CO)_6$ in butanol. All other alcohol solutions have the same form of the potential energy surface and vary only in the number and depth of the various wells.

The motion along the potential energy surface is dictated by the Langevin equation:

$$m\dot{v}(t) = -\xi m v(t) + R(t) \tag{4.2}$$

where m is the mass of the metal fragment,[1] ξ is the friction coefficient, R(t) is the fluctuating force, and $v(t)$ is the velocity.(60) The friction coefficient is representative of the frictional force from the solvent acting against the particle motion. The fluctuating force is random and results from collisions between the metal fragment and the solvent; it has zero mean and is uncorrelated to the particle velocity:

$$\langle R(t) \rangle = 0 \tag{4.3a}$$

$$\langle R(t) \cdot v(0) \rangle = 0 \tag{4.3b}$$

In the simulations discussed here, the random force will be considered white noise; the process is Markovian.

The friction coefficient is related to the bulk solvent viscosity, η, using Stokes' law:

$$\xi = \frac{2\pi\eta d}{m} \tag{4.4}$$

[1]The results of the simulations show the same trend when two body reduced mass (based on the metal fragment and the alcohol) is used in the simulation.

subject to slip boundary conditions, where d is the Brownian particle diameter and m is the Brownian particle mass. Slip conditions (as opposed to stick conditions) have been shown to be more appropriate for the type of calculations carried out here since it is expected that a saturated metal center will not interact strongly with surrounding solvent species.(80; 81; 82; 83) Further, we consider a system where the Brownian particle is of similar size to the solvent molecules. Viscosity values at room temperature[2] were used from a standard reference text.(58)

The initial velocity is selected from a thermal distribution and the initial position is selected randomly. The position, $\mathbf{r}$, and velocity, $\mathbf{v}$, after one time step are calculated using the velocity-Verlet algorithm:(84)

$$\mathbf{r}(t+\delta t) = \mathbf{r}(t) + c_1\mathbf{v}(t)\delta t + c_2\mathbf{a}(t)\delta t^2 + \delta\mathbf{r}^G \tag{4.5a}$$

$$\mathbf{v}(t+\delta t) = c_0\mathbf{v}(t) + (c_1 - c_2)\mathbf{a}(t)\delta t + c_2\mathbf{a}(t+\delta t)\delta t + \delta\mathbf{v}^G \tag{4.5b}$$

where c_0, c_1 and c_2 are dependent on the friction coefficient according to:

$$c_0 = e^{\xi\delta t} \tag{4.6a}$$

$$c_1 = (\xi\delta t)^{-1}(1 - c_0) \tag{4.6b}$$

$$c_2 = (\xi\delta t)^{-1}(1 - c_1) \tag{4.6c}$$

and $\delta\mathbf{r}^G$ and $\delta\mathbf{v}^G$ are the random components of the position and velocity, respectively, chosen from a Gaussian bivariate distribution. These random terms both have zero mean, but since they derive from the same random process (collisions with the bath), they are correlated.(84) The correlation is defined:

$$\langle(\delta\mathbf{r}^G\delta\mathbf{v}^G)\rangle = \delta t \mathrm{k_B}T(\xi\delta t)^{-1}(1 - e^{-\xi\delta t})^2. \tag{4.7}$$

The criteria for the use of this simulation type is that the particle must experience many collisions within the timescale of the dynamics. This criteria is met when:

$$\xi\delta t \gg 1. \tag{4.8}$$

[2]Inclusion of local heating effects that result from photoexcitation was attempted by altering the bath temperature at early simulation times. The simulation results at higher temperature are faster, as expected, but do not show any difference in the trends observed for the various simulation types. Consequently, all simulations reported here were carried out in room temperature solutions. Inclusion of pressure variations (also a result of photoexcitation) in the simulation will change the friction coefficient and should, therefore, have an effect that is similar to increasing the temperature.

Thus, the time step of 0.500 ps is chosen for these simulations. It is large enough to ensure the validity of this inequality and, at the same time, is small enough to ensure adequate sampling of the trajectories.

Three distinct simulation types were carried out for the rearrangement in each of the solvents studied: stochastic, chainwalk, and biased chainwalk. All three simulation types begin with a randomly chosen velocity and position and utilize the above algorithm to move the particle within a given well. The metal center becomes unbound when it moves beyond the position where the potential is defined for a given site in either the positive or negative direction (refer to Figure 4.6). The simulation ends when a particle becomes trapped in the hydroxyl well; a trapped particle is defined as being $10k_BT$ below the barrier top. The difference between the three simulation types is in the choice of a new site after the metal center has become unbound, but before it is trapped. In the first simulation type, the stochastic simulation, after the alkyl bound complex is dissociated from the metal center a new site and a new position in the well that defines the site are randomly chosen. In the second simulation choice, the random chainwalk simulation, dissociation of an alkyl bound complex is followed by movement to an adjacent site and the position will be on the edge of the well. If there is more than one adjacent site, the site is chosen randomly from the possibilities. The third simulation type, the biased chainwalk simulation, is the same as the random chainwalk simulation except that the choice between neighboring sites is weighted by the derivative of the potential energy surface so that the site with the strongest binding energy is most likely. The biased chainwalk simulation represents a rearrangement process that is between the two extremes of pure stochastic and pure chainwalk. The biased chainwalk simulation reflects the possibility that dissociation can occur, but that the choice of the next site will be influenced by the previous position and the force from the potential.[3]

The chainwalk and biased chainwalk mechanisms as described are not purely associative as suggested by previous studies.(72; 75) Our model is dissociative in nature and cannot, therefore, be used to examine a purely associative mechanism. This is not important because the intermediate complexes are the same in both the associative and dissociative mechanisms and the only difference in the mechanistic descriptions will be the transition state of the

[3]Code for all three simulation types is given in Appendix 2.

complex as it moves from one site to another. In our simulations, the transition state will characterize the barrier heights on the potential energy surface and will alter all of the barriers in a similar fashion. Further, all alcohol solvents will have a similar change in the barrier height. Since we are concerned with the trends between the different models as they relate to the experimental data, this limitation in our model is not expected to have a significant contribution.

In order to demonstrate that the trends in rearrangement time do not depend on the absolute barrier height, simulations were carried out where the binding energy of the complex was adjusted by ± 5-10% of the DFT results. As expected, simulation sets with similar energy adjustments show similar results for all of the alcohol solvents studied. Table 4.2 gives the rearrangement time (in ps) for each solvent as the energy is adjusted by ΔE. Figure 4.7 shows a plot for each of the simulation types for all five ΔE values for the five solvents. In Figure 4.7, panel A shows the stochastic simulation results, panel B shows the chainwalk results, and panel C shows the biased chainwalk results.

4.4 Results

Upon irradiation with 266 nm light, a single carbonyl group dissociates from the parent hexacarbonyl complex within 100 fs.(85) The unsaturated metal center is solvated by a ligand from the bath within 1-2 ps resulting in an 18 electron complex with varying degrees of stability.(17) UV-pump, IR-probe difference spectra are shown in Figures 4.8 and 4.9 for chromium hexacarbonyl in methanol and pentane, respectively, at varying delay times after photoexcitation. Negative absorptions in the figures indicate the depletion of parent molecules and positive absorptions indicate the presence of transient or product species.

In neat methanol, irradiation of $Cr(CO)_6$ results in the behavior shown in Figure 4.8. Three features are visible in the difference spectra: the parent bleach centered around 1980 cm^{-1}, and two absorptions from the $Cr(CO)_6$-MeOH species at 1887 and 1939 cm^{-1} corresponding to the A_1 and E bands of the hydroxyl solvated complex respectively. No peaks are observed corresponding to the solvation of the metal center with the alkyl portion of the methanol molecule. The absorptions from the hydroxyl solvated species grow in with

Alcohol	Energy Shift (ΔE (kcal/mol)	Stochastic	Chainwalk	Biased Chainwalk
1-propanol	+0.30	491.9	693.5	410.0
	+0.10	437.3	649.1	369.9
	0.00	428.4	627.4	357.5
	-0.10	433.6	616.0	331.3
	-0.30	400.4	579.7	321.4
2-propanol	+0.30	267.2	346.4	183.7
	+0.10	242.1	324.7	174.8
	0.00	231.4	314.3	161.9
	-0.10	224.4	304.5	158.5
	-0.30	209.7	268.6	145.0
1-butanol	+0.30	609.4	964.8	500.9
	+0.10	570.7	876.6	453.6
	0.00	543.7	853.2	431.0
	-0.10	525.2	815.0	413.8
	-0.30	483.4	756.6	375.7
2-butanol	+0.30	705.8	961.8	488.8
	+0.10	665.4	915.4	441.2
	0.00	641.0	863.1	420.5
	-0.10	632.2	863.3	416.3
	-0.30	569.2	766.2	375.2
isobutanol	+0.30	747.0	1307.9	683.6
	+0.10	715.3	1206.7	619.6
	0.00	697.3	1101.4	607.0
	-0.10	657.7	1093.4	542.4
	-0.30	620.2	991.6	512.5
1-pentanol	+0.30	901.1	1515.1	767.3
	+0.10	841.7	1404.9	730.3
	0.00	795.9	1392.3	676.6
	-0.10	796.0	1250.6	660.9
	-0.30	706.4	1201.9	596.8
2-pentanol	+0.30	842.7	1310.3	592.3
	+0.10	776.0	1223.6	551.8
	0.00	755.1	1145.7	526.8
	-0.10	752.5	1131.7	489.8
	-0.30	665.4	1051.0	445.5

Table 4.2. Rearrangement time for five alcohol solvents for five different energy values. The energy is changed by adding the given ΔE value to the DFT calculated binding energy used in the main simulations.

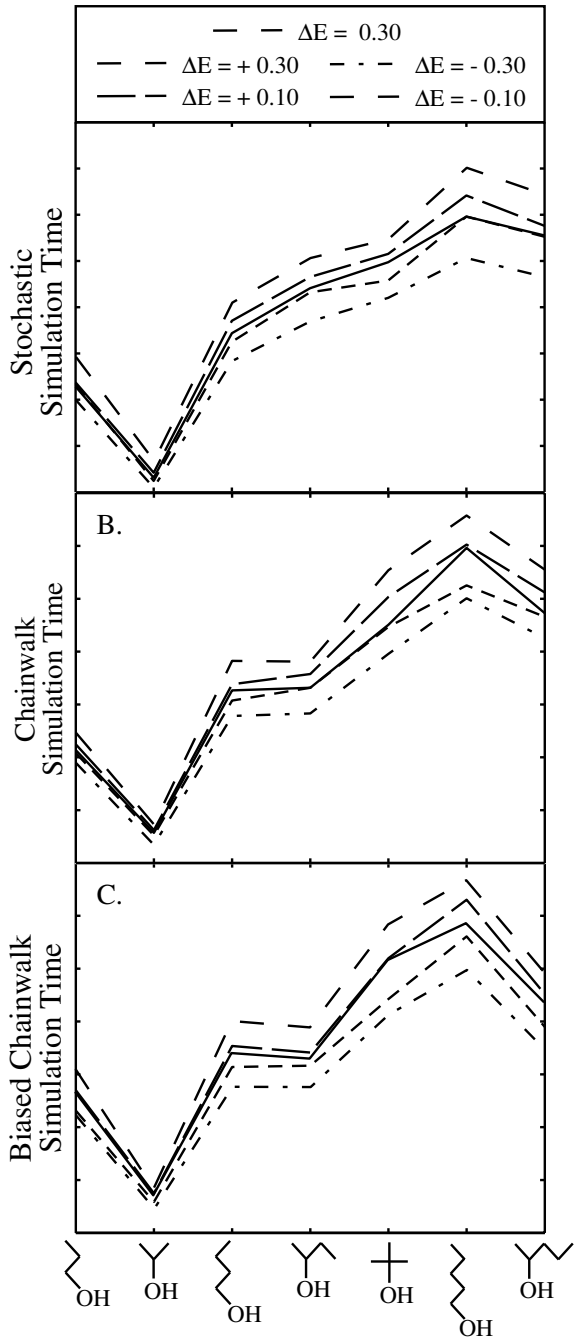

Figure 4.7. Simulation results for seven solvent systems with varying binding energy values. The x-axis represents the simulation time required for metal pentacarbonyl complexes to become bound to the hydroxyl site of the alcohol. The energy is scaled by adding or subtracting the ΔE value from the DFT calculated binding energy. Trends in the rearrangement time do not show large variability with the energy range shown.

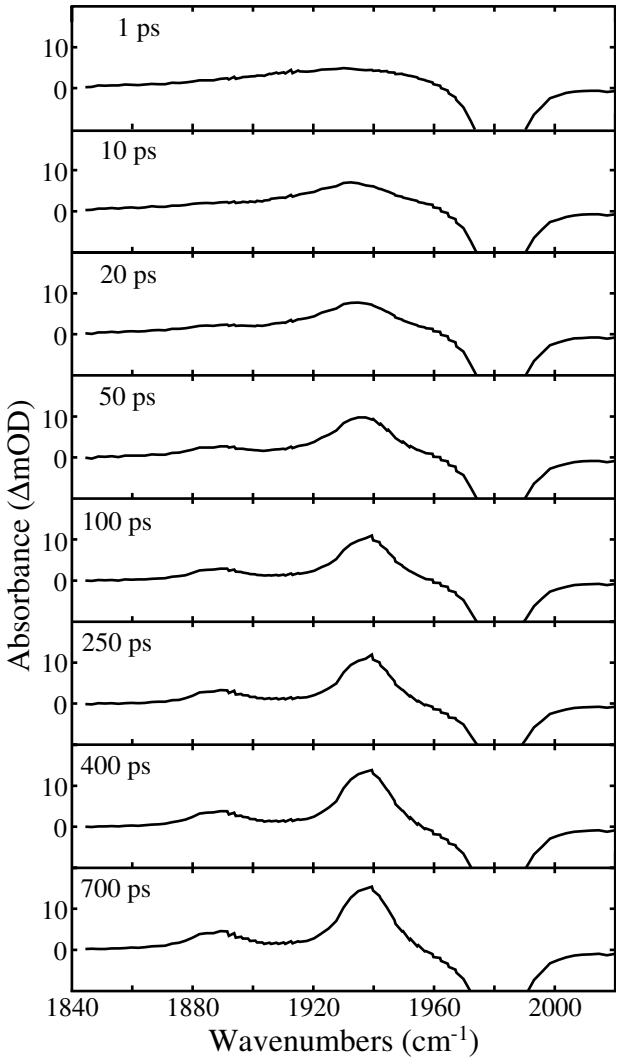

Figure 4.8. UV-pump, IR-probe spectra of chromium hexacarbonyl in neat methanol at increasing delay times after photoexcitation.

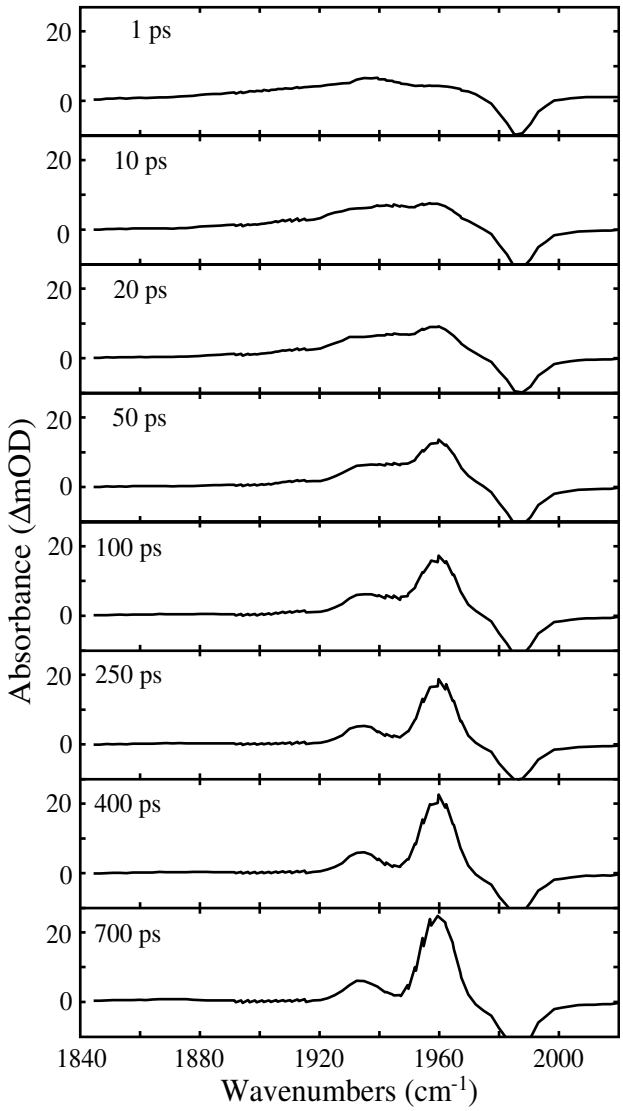

Figure 4.9. UV-pump, IR-probe spectra of chromium hexacarbonyl in neat pentane at increasing delay times after photoexcitation. The apparent increase in the bleach at long delay times is an experimental artifact.

a time constant of 37.5 ± 5.1 ps which is consistent with previously reported values of the vibrational relaxation time of the solvated pentacarbonyl complex in methanol.(74)

In neat pentane, Figure 4.9, only alkyl groups are available to solvate the unsaturated metal center. Again, three distinct features are visible in the difference spectra for $Cr(CO)_6$ in pentane: the parent bleach centered at 1985 cm^{-1} and two absorptions from the $Cr(CO)_5$-pentane species at 1932 and 1960 cm^{-1}, corresponding to the A_1 and E bands of the complex respectively.(86) These absorptions are blue shifted from the values associated with $Cr(CO)_5(MeOH)$ reflecting the increased electron donating ability of the hydroxyl group to the metal center. These absorptions grows in with a time constant of 43.5 ± 5.5 ps which is again consistent with previously reported values of the vibrational relaxation time of the solvated pentacarbonyl complex in pentane.(17)

The experiments in neat methanol and pentane exhibit little dynamical behavior: after excitation with 266 nm light, a carbonyl ligand is dissociated, followed by solvation of the unsaturated metal center and vibrational relaxation. When the experiment is carried out in a longer chain alcohol, however, solvation by both the alkyl site and the hydroxyl site is observed and rearrangement dynamics can be monitored. The difference spectra for $Cr(CO)_6$ in 1-butanol are shown in Figure 4.10. Four distinct absorptions are seen in the spectra. These features are attributed to the parent bleach at 1983 cm^{-1}, an alkyl solvated pentacarbonyl complex E band at 1957 cm^{-1}, and two hydroxyl solvated pentacarbonyl absorptions at 1892 and 1935 cm^{-1} corresponding to the A_1 and E bands respectively. The A_1 band of the alkyl solvated complex is masked by the overlapping E band of the hydroxyl solvated complex and is not observed. At early times, all four features are present and, at increasing time delays, the intensities of the absorptions from the alkyl solvated species decrease and those from the hydroxyl solvated species increase. Kinetic traces for the decay of the alkyl bound complex and the rise of the hydroxyl bound complex are shown in Figure 4.11. These processes are concomitant with similar time constants of 240 ± 20 and 310 ± 40 ps respectively.[4] The similarity of the decay time for the alkyl solvated species and

[4]The discrepancies between the time constants for the decay of the alkyl absorption and the rise of the hydroxyl absorption are a result of the fitting routine used in the data analysis. Since the solvent environment influences the absorption frequencies of the parent species and intermediate complexes, there is an inherent error in the fits which is not accounted for in the errors of the fits to the data which only reflect the confidence interval of the fit representing the data.

the rise time of the hydroxyl solvated as well as the isosbestic point (point of unchanging intensity between two peaks) that is observed at 1946 cm^{-1} indicates that these are related processes. This is consistent with the expectation for this process, namely that the weakly bound alkyl solvated complex will eventually rearrange to the more stable hydroxyl bound configuration.

The only experiments carried out in alcohol solutions that do not exhibit the rearrangement described for 1-butanol are methanol, as mentioned above, and ethanol. The reason for the lack of rearrangement in these solvents is attributed to the inability to see distinct absorptions in the first 30 ps after photoexcitation. At very early times, the metal carbonyl species is vibrationally excited. This excess energy results in absorptions that are broad and red shifted as compared with the species in its vibrational ground state.(18) Further, since the quantum yield of carbonyl loss is not 1.00, there will also be a population of excited parent molecules.(87) These excited species will have absorptions that are red shifted with respect to the parent bleach. This is the same spectral region as the alkyl solvated species absorbs and, therefore, it is reasonable to expect that the population of alkyl solvated complexes will be masked by vibrational relaxation processes. Because there are very few alkyl sites for the metal center to sample in methanol and ethanol, the rearrangement occurs on a time scale that is comparable to vibrational relaxation and is therefore not directly observable. Simulations of these two solvent systems using the model discussed below give rearrangement times that are extremely fast in agreement with the experimental observations.

All of the other alcohol solutions yield difference spectra that are very similar to that shown for 1-butanol. The main difference between the solvents is the rearrangement time. Table 4.3 lists the decay time of the alkyl solvated absorption centered around 1957 cm^{-1} and the rise time of the hydroxyl solvated absorption centered around 1935 cm^{-1}. In cases where only one time constant is given, a single exponential function was used to fit the data. In cases where two time constants are provided, the data were fit to a double exponential. The disparity between data fit with a single exponential and data fit with a double exponential is related to the properties of the solvent. Since vibrational energy relaxation is a solvent dependent process, it is not always perfectly accurate to use the

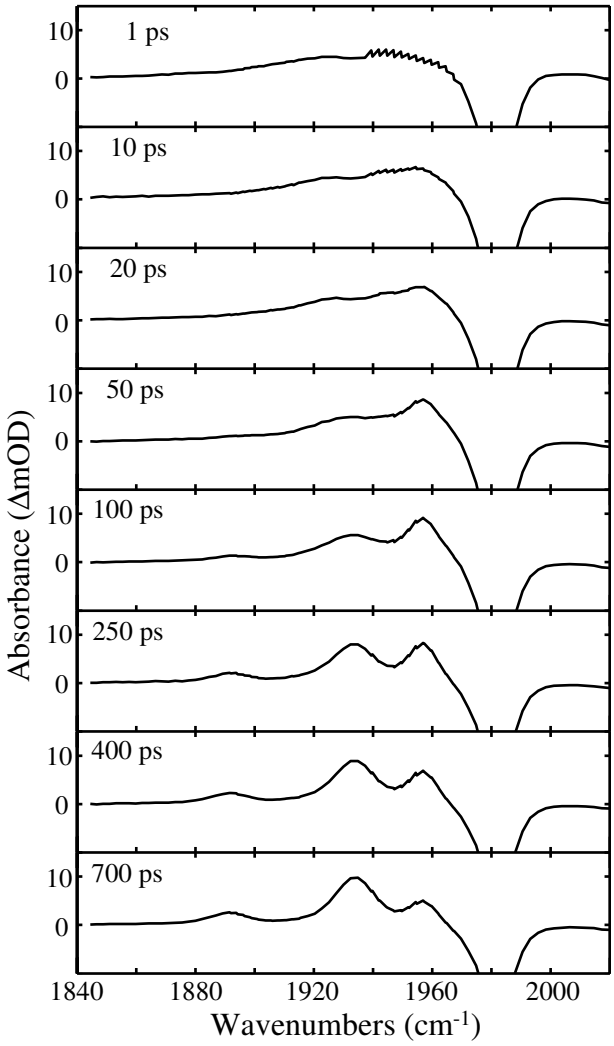

Figure 4.10. UV-pump, IR-probe spectra of chromium hexacarbonyl in neat 1-butanol at increasing delay times after photoexcitation.

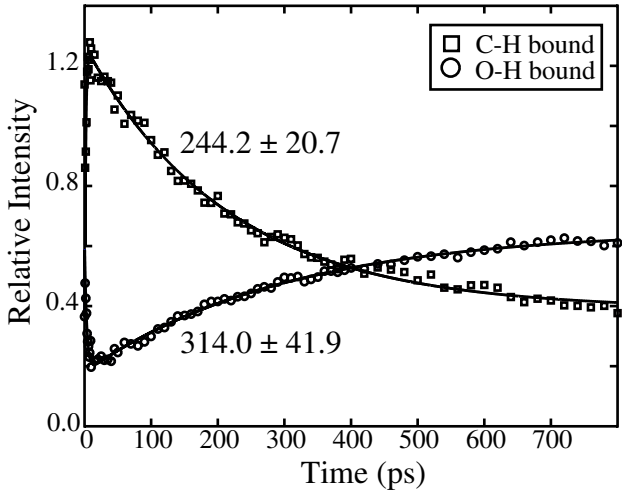

Figure 4.11. Experimental kinetic data for chromium hexacarbonyl in 1-butanol. The experimental data is obtained by fitting the spectra of $Cr(CO)_5$-butanol with the sum of spectra of $Cr(CO)_5$-methanol (OH-bound) and $Cr(CO)_5$-pentane (CH-bound) according to Equation 1. Kinetic traces of the alkyl bound complex (open squares) and the hydroxyl bound complex (open circles) are shown with single exponential fits to the data (solid lines). Time constants for the exponential fits are shown beside each trace.

Alcohol	Decay of M-CH Complex (ps)	Rise of M-OH Complex (ps)
1-propanol	223.0±9.9	225.7±11.2
2-propanol	101.8±3.9	101.9±5.6
1-butanol	244.2±20.7	314.0±41.9
2-butanol	198.9±10.7	161.3±10.3
isobutanol	377.7±37.8	427.4±46.8
1-pentanol	69.6±27.1	23.0±17.5
	461.5±415.0	440.1±162.6
2-pentanol	324.5±55.0	243.5±32.8
2-methylbutanol	440.5±95.2	402.5±82.8
3-methylbutanol	480.9±143.6	342.6±58.3

Table 4.3. Time constants for exponential fits to experimental data. In all alcohol solutions the absorption from the alkyl solvated metal complex decays with a concomitant rise in the absorption from the hydroxyl solvated metal complex.

spectra from pentane and methanol solutions to fit the data in a long chain alcohol. Further, the parent bleach and product absorptions are shifted slightly depending on the solvent environment. Thus, fitting the spectra of $Cr(CO)_6$ in a long chain alcohol with the spectra in methanol and pentane results in some inherent error.

In assigning a mechanism to the experimental data it is useful to group the data according to the expected results associated with each mechanism. In Figure 4.12A the experimental data is grouped according to the number of carbon atoms in the alcohol; in the case of a stochastic mechanism, this grouping scheme would show an obvious trend. In Figure 4.12B the experimental data is grouped according to the number of carbon atoms from one end of the alkyl chain to the hydroxyl group. Branched molecules are plotted multiple times since they can have more than one distance associated with them. If a chainwalk mechanism is the best description of the reaction, then it would be expected that alcohols having the same number of carbon atoms from one end of the alkyl chain to the hydroxyl group would have similar rearrangement times. Inspection of these plots indicates that while the general trend of increasing rearrangement time for increasing chain length are observed in both plots, a simple assignment to one of these two possible mechanisms cannot be made based on these groupings alone.

A more quantitative analysis of this type can be made using a population matrix that is

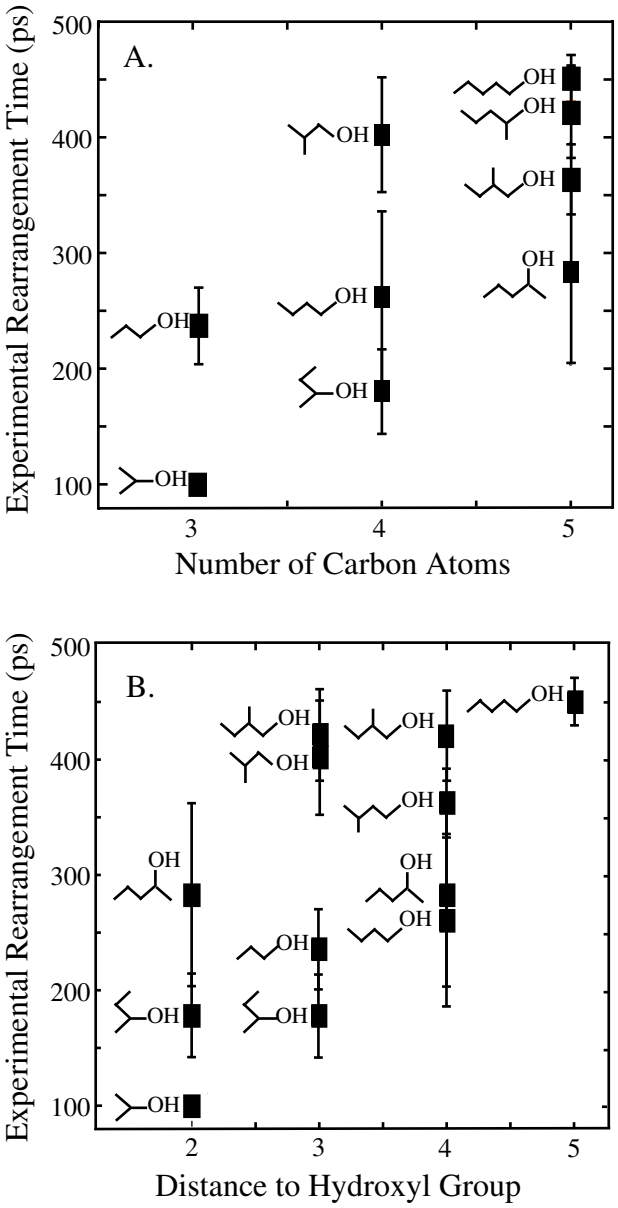

Figure 4.12. Experimental rearrangement times grouped according to the number of carbon atoms in the alcohol (A) and according to the distance from the end of the alkyl chain to the hydroxyl site (B).

propagated in time using a connection matrix consistent with the alcohol and the simulation type. The population matrix is simply a vector indicating the fraction of complexes bound at a given site. The connection matrix shows how population can be transferred as described below for each simulation type. For example, in all alcohols and all simulation types the initial population will be uniformly distributed among the alkyl sites and the alcohol site because we assume that the initial solvation site is random. Population from the hydroxyl site increases with time, but cannot be removed. In the stochastic simulation, population from each of the alkyl sites is transfered to each of the other sites. Eventually, all of the population will be confined to the hydroxyl site and the simulation will end; the simulations discussed below are complete when 99% of the population is in the hydroxyl well. The first step of the stochastic matrix propagation process for 1-butanol is:

$$\begin{bmatrix} OH & C_\alpha & C_\beta & C_\gamma & C_\delta \\ \frac{1}{5} & \frac{1}{5} & \frac{1}{5} & \frac{1}{5} & \frac{1}{5} \end{bmatrix} \cdot \begin{bmatrix} & OH & C_\alpha & C_\beta & C_\gamma & C_\delta \\ OH & 1 & 0 & 0 & 0 & 0 \\ C_\alpha & \frac{1}{5} & \frac{1}{5} & \frac{1}{5} & \frac{1}{5} & \frac{1}{5} \\ C_\beta & \frac{1}{5} & \frac{1}{5} & \frac{1}{5} & \frac{1}{5} & \frac{1}{5} \\ C_\gamma & \frac{1}{5} & \frac{1}{5} & \frac{1}{5} & \frac{1}{5} & \frac{1}{5} \\ C_\delta & \frac{1}{5} & \frac{1}{5} & \frac{1}{5} & \frac{1}{5} & \frac{1}{5} \end{bmatrix}$$

In the chainwalk simulation, the process is the same, but the propagation matrix is different. The population will move to an adjacent site with each propagation step. The first step for the chainwalk matrix propagation process for 1-butanol is:

$$\begin{bmatrix} OH & C_\alpha & C_\beta & C_\gamma & C_\delta \\ \frac{1}{5} & \frac{1}{5} & \frac{1}{5} & \frac{1}{5} & \frac{1}{5} \end{bmatrix} \cdot \begin{bmatrix} & OH & C_\alpha & C_\beta & C_\gamma & C_\delta \\ OH & 1 & 0 & 0 & 0 & 0 \\ C_\alpha & \frac{1}{2} & 0 & \frac{1}{2} & 0 & 0 \\ C_\beta & 0 & \frac{1}{2} & 0 & \frac{1}{2} & 0 \\ C_\gamma & 0 & 0 & \frac{1}{2} & 0 & \frac{1}{2} \\ C_\delta & 0 & 0 & 0 & 1 & 0 \end{bmatrix}$$

The number of propagation steps required for the complete movement of population into the hydroxyl site is shown for each alcohol studied in Table 4.4.

The results using the propagation matrix provide a simple way to group the data in order to assign a particular rearrangement mechanism to the data. Correlation graphs of

Alcohol	Stochastic (steps)	Chainwalk (steps)
1-propanol	25	34
2-propanol	25	29
1-butanol	31	55
2-butanol	31	44
isobutanol	31	45
1-pentanol	38	81
2-pentanol	38	67
2-methylbutanol	38	67
3-methylbutanol	38	66

Table 4.4. Number of steps for 99% of the starting population to reach the hydroxyl site via the matrix propagation method described in the text. Stochastic simulations carry no information about the structure (linear, branched) of the molecule, and yield identical results for molecules of the same length.

the matrix simulation results plotted against the experimental data are shown in Figure 4.13 for each of the solvent systems studied. Figure 4.13A shows the experimental data plotted against the stochastic matrix propagation results. Figure 4.13B shows the experimental data graphed against the chainwalk matrix propagation results. Although the chainwalk matrix propagation results reflect the experimental data more closely than the stochastic results, neither of the models provides good agreement with the experiments.

Since neither of these two grouping schemes definitively identifies the mechanism for the ligand rearrangement, the experimental results alone cannot be used to assign a particular mechanistic description to this process. One reason for this is that such a simple inspection does not take into account the effects of the bath on the rearrangement process. In particular, solvent viscosity is expected to be strongly linked to the timescale for dissociation of an alkyl bound solvent molecule. This is because the viscosity is the solvent parameter that characterizes the friction coefficient and allows for diffusive motion along the barrier as described by the Langevin equation. Simulations, therefore, were carried out for all of the solvent systems studied experimentally to account for the influence of the environment. Kinetic data was obtained by fitting the population of hydroxyl bound complexes over time with a single exponential function. An example of a group of simulated data sets and the resulting single exponential fits are shown in Figure 4.14 for 1-butanol. The results of sim-

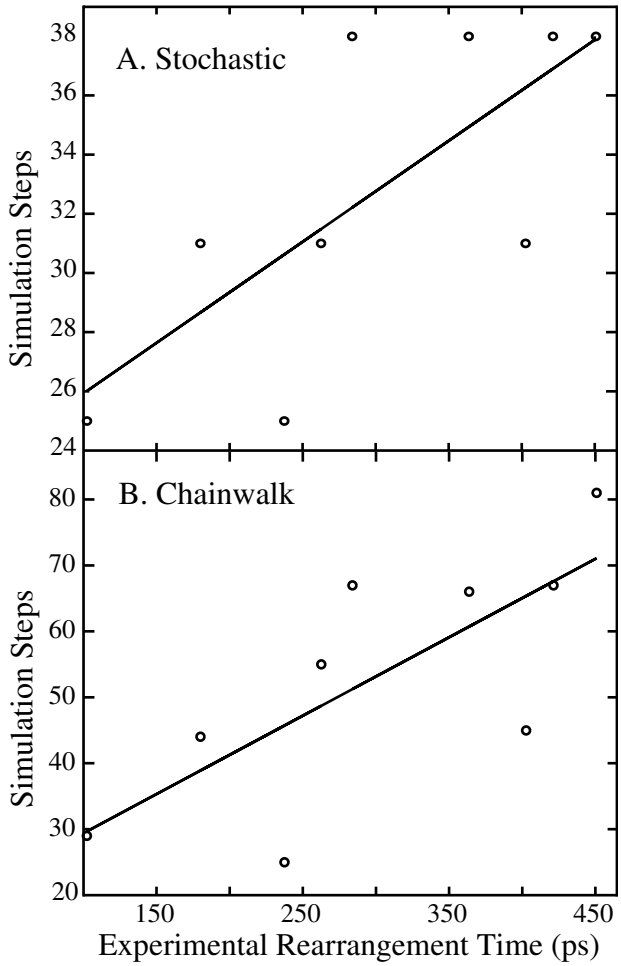

Figure 4.13. Experimental rearrangement times plotted against the number of matrix propagation steps required for the entire population to be solvated at the hydroxyl site. Matrix propagation results for the stochastic simulation (A) and the chainwalk simulation (B) are shown. The solid line is a linear fit to the data demonstrating a relationship that is not linear and each point represents the rearrangement of chromium pentacarbonyl in one of the nine solvents of Table 4.4.

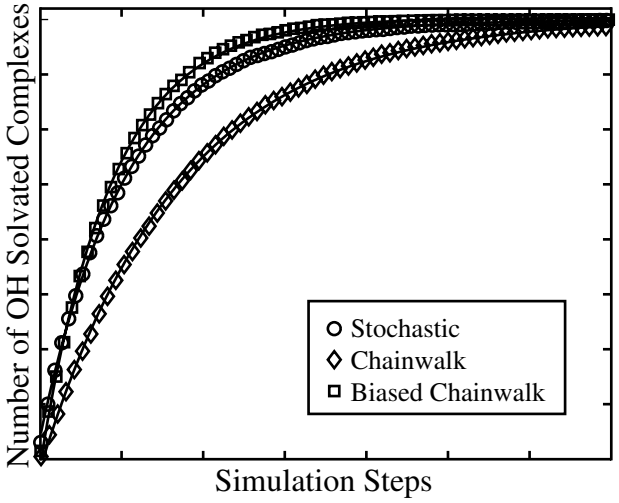

Figure 4.14. Simulation kinetic traces for $Cr(CO)_5$ in 1-butanol. Circles represent stochastic simulation results, diamonds represent chainwalk results, and squares represent biased chainwalk results. Single exponential fits are overlaid onto the data. The y-axis represents the percentage of $Cr(CO)_5$ complexes that are bound to the hydroxyl group of the alcohol. Numbers and units are not given in order to deemphasize quantitative results and emphasize qualitative trends.

ulations for all of the solvent systems studied are given in Table 4.5. In Figure 4.15 all of the simulation data from Table 4.5 are plotted against the experimental data. Linear fits to each of the plots result in goodness of fit values that range from 0.651 - 0.756. While the biased chainwalk mechanism gives the best correlation between the experimental and simulation data, none of the goodness of fit values are sufficiently close to 1.0 to allow for confident assignment of one mechanism over the other.

Although the slope of the correlation graph in Figure 4.15 also implies that the biased chainwalk mechanism best fits the experimental results, it is important to remember that numerical values from the simulations should not be used quantitatively because of simplifications in the model. For example, the use of a cosine potential will systematically change the number of steps required in the simulation which means that the data trends themselves are more informative than the data alone. Figure 4.16 shows the results of each simulation type for the nine solvents studied. The trend in the experimental values is well simulated

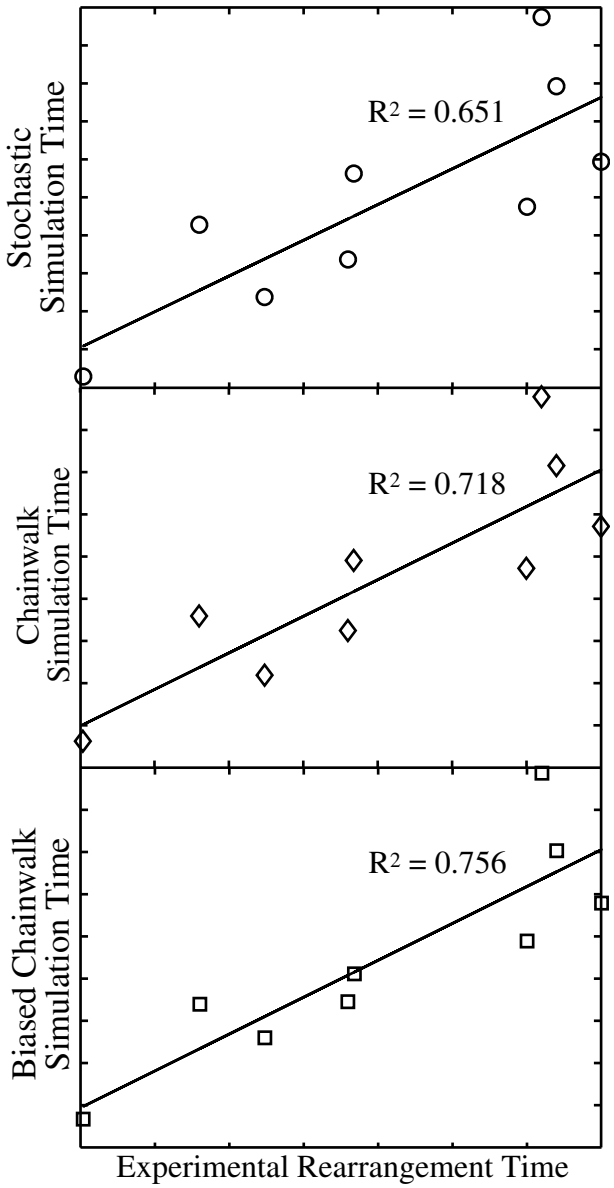

Figure 4.15. Experimental data plotted versus simulation data for each solvent studied. The line from a linear-least-squares analysis is shown along with the slope and the goodness of fit value for each simulation type. The y-axis represents the number of simulation steps required for all complexes to be bound to the hydroxyl group. The x-axis is the experimental rearrangement time obtained by averaging the fits for the decay of alkyl-bound complexes and the rise of hydroxyl-bound complexes. Numbers and units are not given in order to deemphasize quantitative results and emphasize qualitative trends.

Alcohol	Stochastic (ps)	Chainwalk (ps)	Biased Chainwalk (ps)
1-propanol	437.2±16.9	636.2±52.8	360.4±22.4
2-propanol	228.4±17.8	325.6±21.0	167.1±14.2
1-butanol	535.8±38.1	847.8±44.8	445.4±31.8
2-butanol	627.3±37.5	918.7±67.9	439.4±29.7
isobutanol	675.9±33.4	1143.9±38.5	589.1±22.2
1-pentanol	792.9±35.0	1343.0±57.7	678.4±31.9
2-pentanol	762.2±60.7	1181.5±69.1	511.1±43.6
2-methylbutanol	992.0±38.2	1629.7±103.5	802.9±39.0
3-methylbutanol	1174.0±78.3	1956.3±128.9	986.8±69.0

Table 4.5. Average simulation time for hydroxyl coordination. All averages are the result of 10 simulation sets of 500 particles each. Errors are the standard deviation from the ten independent simulation sets.

by all three mechanisms and are within the errors of the experiment; therefore, none of the simulation types can be definitively assigned to the experimental observations.

In order to understand why the results from all three simulation types are so similar, it is instructive to look at the evolution of a delta function distribution for the initial solvation site and position in the well. In these sets of simulations, the particles are initially placed in the center of the gamma carbon well and then allowed to evolve according to the procedures described above. Figure 4.17 shows the evolution of the distributions for each of the three simulation types. The first time slice shows the delta distribution after 20 simulation steps. Each subsequent time slice shows the distribution after an additional 20 simulation steps. In all three of the simulation types, it is observed that the distribution quickly randomizes itself. In fact, the distributions for the three simulation sets are very similar in the last time slice shown (160 simulation steps) with the main difference being the time required for all particles to become trapped in the hydroxyl well. Further, because the reaction is highly diffusive, the stochastic simulation does not differ much from either of the chainwalk simulations. Since the population distribution is quickly randomized and the alkyl well depths are very similar for all of the alcohols studied, the simulation results do not show a clear distinction between the rearrangement types. These results suggest that the two mechanistic descriptions of linkage isomerization reactions are not adequately

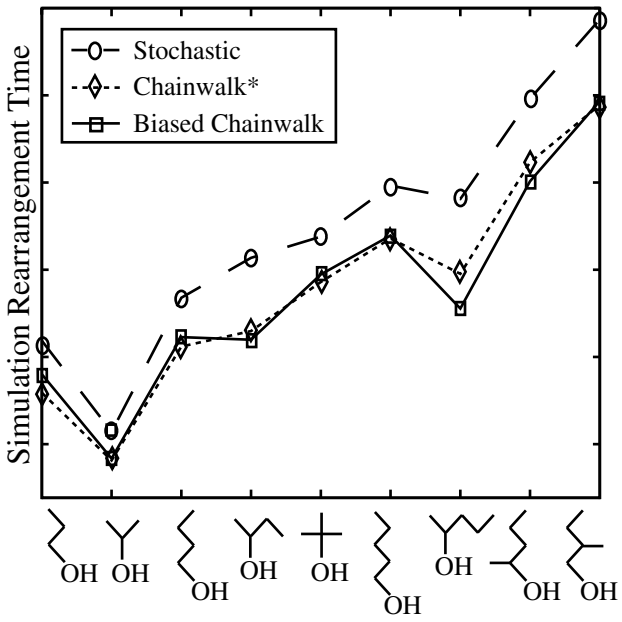

Figure 4.16. Simulation data for all alcohol solvents. The number of simulation steps is plotted against the solvent species. Numbers and units are not given in order to deemphasize quantitative results and emphasize the trends in the simulation results. *Note that the chainwalk simulation times have been divided by 2 to allow for comparison of the trend.

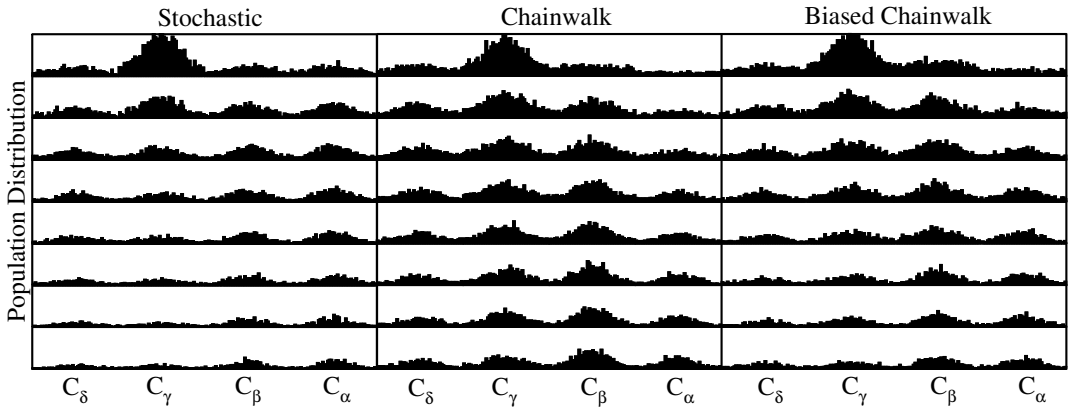

Figure 4.17. Evolution of population distribution at increasing times after starting at the center of the C_γ well of 1-butanol. Each distribution shown is 20 simulation steps after initialization. Loss of population from the alkyl wells (shown) is transfered into the hydroxyl well (not shown).

distinguishable using Brownian dynamics and an assignment of one or the other based on these simulations alone is not justified.

There are two obvious reasons for the failure of Brownian motion simulations in predicting a single mechanistic description of the ligand rearrangement process. First, it is possible that the actual, physical mechanism is a hybrid of these two extremes. Simply put, the mechanisms are not different when the bath is included in the dynamic behavior. Fluctuations of the bath that result from the viscosity of the solvent as well as the interaction energy between the metal center and the solvent ligand are the determining factors in the rearrangement time. This would mean that the microscopic nature of sampling sites is the fast step and therefore not a determining factor in the timescale in the rearrangement. Second, it may be that the Langevin equation does not adequately simulate the physical behavior of the system. A more sophisticated analysis that incorporates the local solvent structure and its effect on the rearrangement may improve the model. For example, if the first solvent shell is highly ordered, an intermolecular rearrangement process will not actually access all sites along the alcohol chain with equal probability.

In order to understand if the chainwalk and stochastic descriptions of ligand rearrangement are physically distinguishable and, if so, which label to assign to the process, further

work must be carried out. It would be interesting to carry out a series of experiments that investigate the rearrangement of $Cr(CO)_6$ in cyclic alcohol solvents. These solvents are expected to give a more definitive difference between the two mechanisms because while the solvent viscosity does not change significantly, a chainwalk mechanism allows for the possibility of very long rearrangement times. In addition, a more complex model of the rearrangement may be required to test the two possibilities. Molecular dynamics simulations will be required to gain a more thorough understanding of the local solvent environment and these will be incorporated into the simulation engine to give a more physical description for the sampling of sites in the stochastic simulation.

4.5 Conclusions

An ensemble measurement of the rearrangement from alkyl bound complexes to hydroxyl bound complexes cannot access the microscopic nature of the ligand rearrangement and cannot, therefore be used to directly assign a specific mechanism to the process. We expect that the limited ability of these experiments to differentiate between the different mechanisms is due to the effect of the solvent on the nature of the rearrangement process. Computer modeling has been utilized for the first time to explicitly include the bath effects in the dynamical linkage isomerization reactions of metal carbonyl complexes in neat alcohol solutions. The models demonstrate dynamic behaviors that are very similar to each other and preclude a definitive assignment of one mechanism over the other indicating that the reaction is highly diffusive. The time required for solvation by the hydroxyl group is longest in the case of a chainwalk description, but the trend in solvation time as the solvent is varied is not very different for the three simulation types. The conclusion of this work is that the mechanistic labels of intramolecular and intermolecular rearrangement used to describe this process are too similar to be uniquely isolated using the diffusive motion along a barrier alone. Current experimental work is aimed at cyclic alcohol solvents which provide deviations between the two mechanisms. Current theoretical work is focused on developing a more realistic description of the local solvent environment and incorporating this into the Brownian dynamics model.

Chapter 5

Mechanistic Studies of Carbon-Hydrogen Bond Activation by Transition-Metal Boryl Complexes

5.1 Introduction to Carbon-Hydrogen Bond Activation

The natural abundance of hydrocarbons has made the activation, or breaking, of carbon-hydrogen (C-H) bonds a continued focus of synthetic chemists.(1; 2; 88) Scientists continue to search for efficient sources of useful, functionalized organic compounds, despite the inherent difficulties of the task. The prime challenge is the relative inertness of C-H bonds (bond energy of 90-100 kcal/mol) which means that hydrocarbon functionalization is generally a kinetically and thermodynamically unfavorable reaction. The goal, then, has become to find catalysts that will provide a low energy pathway to the formation of stable, functionalized products.

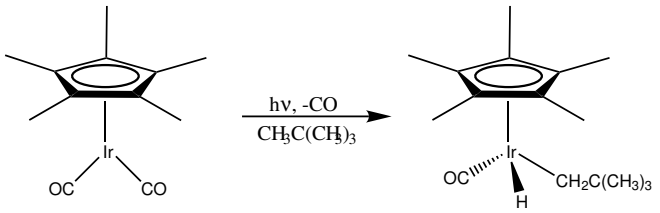

Figure 5.1. First example of a metal-hydride formed in a photolytic C-H activation reaction. In this example, the loss of a carbonyl group upon photolysis allows for the oxidative addition of an alkane to the metal center.

One synthetic approach that has found success is the use of transition-metal complexes to facilitate the reaction.(89) The first example of an organometallic reaction that produced a hydrodoalkylmetal complex was presented by Bergman in 1982.(90) Shortly after, Graham and coworkers reported a similar observation when a related iridium complex was photolyzed in an alkane solution as shown in Figure 5.1.(91) There are two advantages to the use of transition-metal complexes in C-H activation reactions. First, many transition metals have demonstrated an ability to selectively activate C-H bonds. Second, transition metal complexes have shown catalytic activity for a number of reactions.

The selectivity of transition metal activation is an important aspect of their chemistry. The energy of a C-H bond depends on its position in the alkane with tertiary C-H bonds being the weakest and primary C-H bonds being the strongest. Many reactions, radical reactions in particular, provide selectivity at the weakest site. Since most straight chain alkanes contain multiple secondary sites, there is a high probability of activating different sites and, therefore, producing multiple products. These products will be physically and chemically very similar which makes purification difficult or impossible. Other transition metal complexes, however, activate primary C-H bonds preferentially, or even exclusively.

Catalytic activation has not been demonstrated as successfully as selectivity. In many synthetic schemes the final product is an alkane attached to the metal center. With such a product, it is necessary to do further chemistry (which implies a decreased final product yield) to break the metal alkane bond and produce a functionalized alkane product. In addition, most reactions require the stoichiometric use of transition metal reagents which can be an expensive undertaking. The possibility of eliminating a functionalized product

compound	% yield
$Cp^*Fe(CO)_2[Bcat(Me)_2]$	20
$Cp^*Ru(CO)_2[Bcat(Me)_2]$	40
$Cp^*W(CO)_3[Bcat(Me)_2]$	85
$Cp^*Mo(CO)_2[Bcat(Me)_2]$	7
$Cp^*Ru(CO)_2[Bpin]$	78
$Cp^*W(CO)_2[Bpin]$	72

Table 5.1. Yields for the functionalization of pentane with various transition-metal boryl complexes. All complexes are named according to convention with $Cp^* = C_5Me_5$, $Bcat(Me)_2$ = B-1, 2-$O_2C_6H_2$-3, 5-Me_2, Bpin = B-1, 2-$O_2C_2Me_4$, and Me = CH_3. Structures for all complexes are shown in Figure 5.2.

and regenerating the transition metal starting material is, therefore, the most desirable characteristic of future C-H activation reaction pathways.

Recently, Hartwig and co-workers have synthesized a group of transition-metal boryl complexes and demonstrated their effectiveness at selectively and catalytically reacting with both saturated and unsaturated hydrocarbons to yield functionalized derivatives.(92; 93; 94; 95; 96) These borylated alkane complexes can easily be converted into a variety of useful complexes using well-developed synthetic techniques.(97) Table 5.1 summarizes the various organometallic reagents and their effectiveness at functionalizing a primary carbon of pentane.(95) Figure 5.2 shows the structures of the various transition-metal boryl compounds discussed.

The selectivity of these transition-metal boryl compounds is well demonstrated and is consistent with other transition-metal reaction sequences. Even in cases where there are multiple primary positions on the alkane, preference for the less sterically hindered position is observed. Examples of reactions with various hydrocarbon solvents and the observed yields for the products are shown in Figure 5.3. Further, these reactions have shown catalytic activity under thermal conditions(96) with the expectation that photochemical reactions behave in a similar fashion. Although the unique reactivity of transition-metal boryl complexes has been demonstrated, it is not well understood mechanistically. Understanding the nature and origin of the reactivity will aid in further synthetic endeavors.

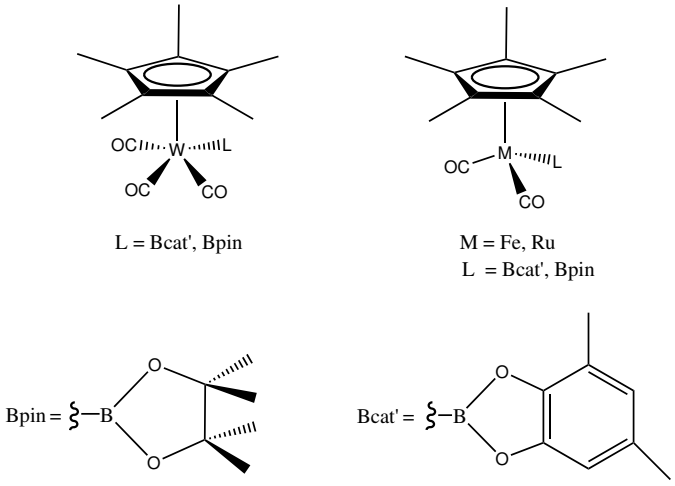

Figure 5.2. Structures of the various transition-metal boryl compounds presented in Table 5.1 and studied using ultrafast spectroscopy.

For this reason, new efforts have focused on the mechanistic details of this and other C-H activation reactions.

5.2 Introduction to Mechanisms of Carbon-Hydrogen Bond Activation

One of the first mechanistic studies to concentrate on transition metal C-H bond activation focused on the unique selectivity that was observed. Bergman and coworkers monitored the coordination of alkanes to unsaturated metal centers using NMR labeling experiments.(50) These experiments showed that longer chain alkanes reacted on a much longer time scale than their shorter chain analogues. The conclusion from these experiments was that coordination to any site on the alkane could occur followed by intramolecular (chainwalk) rearrangement to a primary site where activation then occurred. With this study, the formation of three center, metal-carbon-hydrogen bonds was identified as an important intermediate step in C-H bond activation.

Later experiments confirmed that the first step in the reaction is the photolytic expulsion

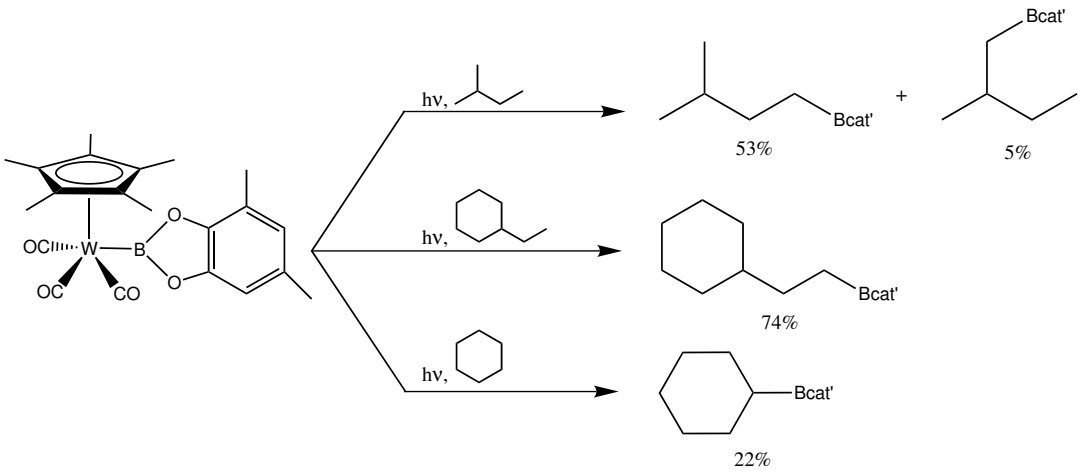

Figure 5.3. Photochemical reactions between $Cp^*W(CO)_3[Bcat(Me)_2]$ and cyclohexane, ethylcyclohexane, and 2-methylbutane. Yields for each product are given. These results demonstrate the highly selective nature of the reaction with a preference for sterically unhindered primary C-H bonds.

of a two-electron donor ligand or dihydrogen to form an unsaturated metal complex.(98) The metal fragment then activates a local carbon hydrogen bond when the experiment is done in a methane matrix. While such an intermediate had been hypothesized for many years, the ability to isolate and spectroscopically characterize the unsaturated complex has broad implications. In the work outlined in this chapter, the two-electron donor is a carbonyl group which is dissociated from the metal center upon photolysis; for this reason, the focus of the following discussion will be on such compounds. It is now generally accepted that the first step after the loss of a carbonyl group from an organometallic compound is the coordination of a solvent molecule to the unsaturated metal center.(52) The alkyl group serves as a 'token' ligand, forming a weak interaction with the metal center. This is in agreement with Bergman's early work investigating the mechanism of C-H bond activation. The steps in between the formation of the solvated complex and the bond activated product are the interesting unknowns that we can utilize ultrafast spectroscopy to probe.

Some of the early work in determining the specific mechanistic details of C-H activation was done by our group in the late 1990s. This work focused on the activation of linear hydrocarbons by $Tp^*Rh(CO)_2$ (Tp^* = HB-3-Pz^*, Pz^* = 3,5-dimethylpyrazolyl) as shown in

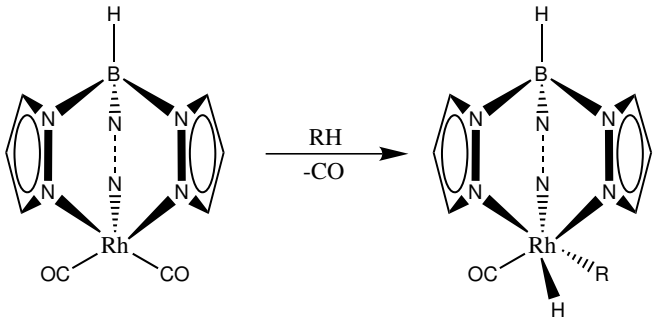

Figure 5.4. The bond activation reaction of $Tp^*Rh(CO)_2$ with linear hydrocarbons. This reaction was studied using ultrafast UV-pump/IR-probe spectroscopy and the mechanism has been outlined.

Figure 5.4. When $Tp^*Rh(CO)_2$ is excited with UV light, a single carbonyl groups dissociates and the vacant site on the metal is quickly occupied by a hydrocarbon from the bulk solvent. One arm of the Tp^* ligand dechelates from the metal center. Bond activation of the coordinated hydrocarbon occurs followed by rechelation of the Tp^* arm. The early steps of dissociation, solvation, and dechelation were monitored using ultrafast UV-pump/IR-probe spectroscopy (for times up to 1 ns); the later steps of bond activation and rechelation were monitored using step- and rapid-scan FTIR (for times from 1 ns to 1 ms). The mechanism is outlined schematically in Figure 5.5.

Hartwig and coworkers have investigated a number of mechanistic possibilities for the reactions of metal-boryl compounds in saturated hydrocarbons including the formation of radical complexes. These radical species could form from the homolytic cleavage of the metal-boron bond. The formation of radical hydrocarbon complexes is known to be most favorable at the tertiary and not primary position; this is contrary to the observations of Hartwig that clearly demonstrate the preferential formation of primary borylated products. Upon excitation, it is possible that a boryl radical forms and reacts with a solvent molecule to produce the final product without formation of any radical alkyl intermediate. Since $Bcat(Me)_2$ $Cp^*W(CO)_3[Bcat(Me)_2]$ and $Cp^*M(CO)_2[Bcat(Me)_2]$ (M = Fe, Ru) all form the same $Bcat(Me)_2$ radical species, they would be expected to have similar reactivities once the radical complex forms. Yet the primary kinetic isotope effects observed in these reactions are very different 1.9, 2.2, and 5.1 for the Fe, Ru, and W complexes respectively.(93)

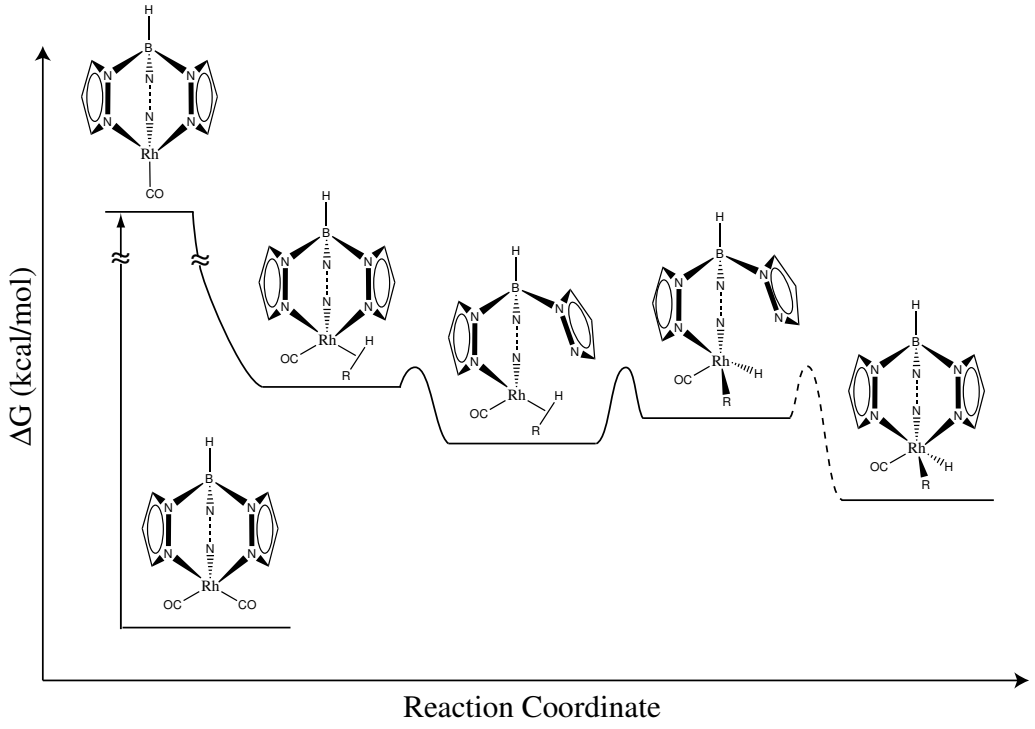

Figure 5.5. The mechanism for C-H activation by Tp*Rh(CO)$_2$ as outlined using ultrafast UV-pump/IR-probe spectroscopy.

The other common pathway for a photoinduced transition metal reaction is carbonyl loss. When the reactions are carried out under ^{13}CO, there is no evidence for the incorporation of the labeled carbonyl into the metal carbonyl complex. Further, an increase in the CO pressure on the reaction vessel had no apparent effect on the reaction yield. These two pieces of evidence indicate that either CO loss is not occurring or that the dissociation is irreversible. Experiments with phosphines indicate that carbonyl loss is occurring. When $Cp^*Fe(CO)_2[Bcat(Me)_2]$ is photolyzed in a 2:1 solution of trimethylphosphine:pentane, a mixture of the metal phosphine ($Cp^*Fe(CO)(PMe_3)[Bcat(Me)_2]$ and the borylated product (pentane-$Bcat(Me)_2$) is produced in a ratio of 0.3:1. When the amount of trimethylphosphine is doubled, the amount of metal phosphine doubles as compared with the amount of borylated pentane produced.(95) With these mechanistic studies, the first step in the photochemical activity of transition metal boryl complexes has been identified as irreversible carbonyl dissociation. After this step, however, multiple mechanistic pathways are possible and not easily differentiable.

Two main mechanistic descriptions have been identified as possibilities for this reaction: σ-bond metathesis and oxidative addition followed by reductive elimination. In a σ-bond metathesis reaction, a σ-bonded ligand reacts with the σ bond of the incoming solvent molecule. A transition state with a four-center bond forms and quickly results in the functionalized hydrocarbon and the metal hydride. Pathways involving σ-bond metathesis are common for d^o metals, actinides, and lanthanides, but have been observed for d^4 and d^5 metals as well. The oxidative-addition/reductive-elimination pathway is more commonly invoked to explain C-H bond activation reactions. In general, this mechanism involves the formation of a bond-activated intermediate followed by elimination of the functionalized alkane. The oxidation number of the metal center is altered in this reaction and the metal center must be amenable to such a possibility. A schematic of these two processes as applied to the transition-metal boryl complexes discussed in this work is shown in Figure 5.6.

Theoretical evidence for both of the pathways shown in Figure 5.6 exists. Work carried out by Lam and Lin indicates that different metal complexes utilize a different mechanism for C-H activation.(99) In this work, the authors show that the lowest energy pathway for the iron complex is a one-step mechanism consistent with the σ-bond metathesis description

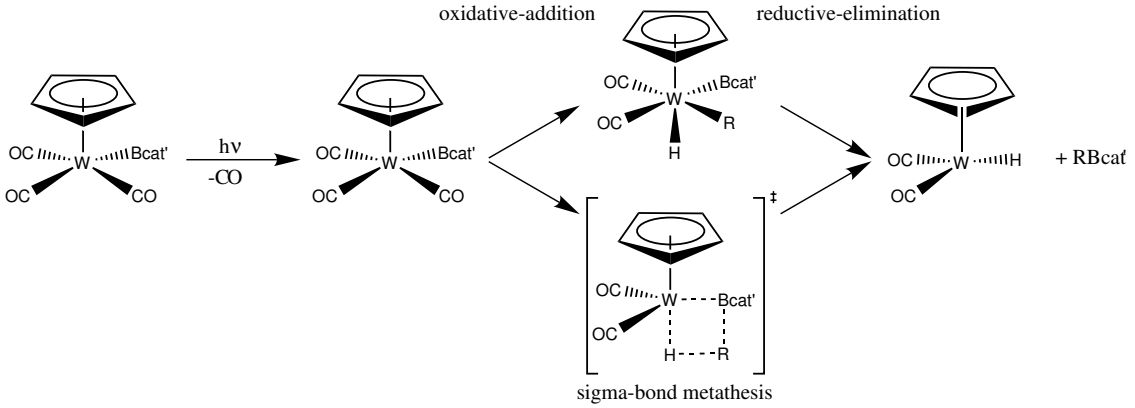

Figure 5.6. Two possible mechanistic pathways proposed for the activation of C-H bonds with transition-metal boryl complexes. The top pathway is the oxidative-addition/reductive-elimination mechanism with the formation of a true intermediate complex. The bottom pathway is the σ-bond metathesis mechanism which involves the formation of a transition state species.

while the two-step oxidative-addition/reductive-elimination pathway is most favorable for the tungsten complex. Interestingly, the authors present evidence for both pathways for the ruthenium complex: when alkane activation occurs it is via a two-step mechanism and when alkene (or aromatic) activation occurs it is via a one-step mechanism. Webster and co-workers also carried out density functional calculations and showed that the σ-bond metathesis pathway is most favorable for both the tungsten and the iron complexes when activating an alkane.(100) The description of the σ-bond metathesis pathway in this work has multiple steps with the formation of multiple intermediate complexes. The mechanism as outlined in that work is shown in Figure 5.7.

The conflicting mechanistic descriptions that have resulted from theoretical calculations have inspired us to study this reaction experimentally using ultrafast, UV-pump, IR-probe spectroscopy. We have investigated the ultrafast reaction dynamics for three transition metal boryl complexes in room temperature solutions of pentane and 1-hexene.

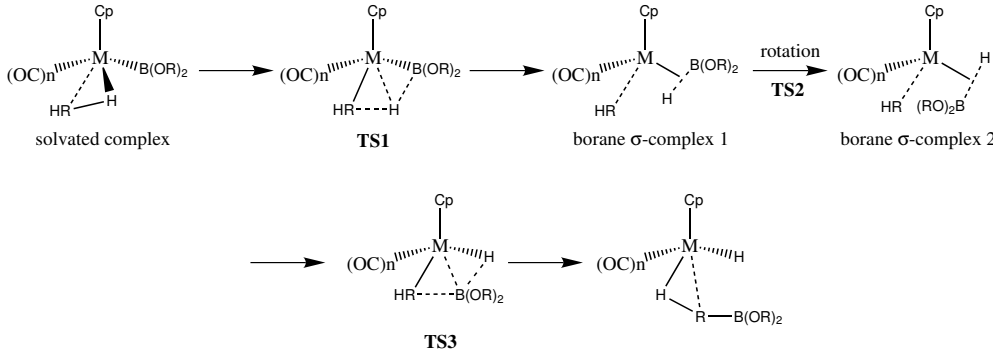

Figure 5.7. Reaction mechanism for the σ-bond metathesis pathway as calculated using DFT by Webster and co-workers.(100)

5.3 Experimental Methods

The pump-probe experiments described in this chapter utilize both 266 nm and 400 nm pump wavelengths. All other aspects of the experimental procedure are as described in Chapter 2.

The $Cp^*Fe(CO)_2[Bcat(Me)_2]$ and $Cp^*W(CO)_3[Bcat(Me)_2]$ complexes were prepared by Tim Boller; the $Cp^*W(CO)_3[Bpin]$ complex was prepared by Marko Hapko, both members of the John Hartwig group at Yale University. The complexes were stored under nitrogen and prepared in the glove box with spectroscopic grade solvents. The molarity of the solutions was adjusted to be about 10 mM, but changed during the experiment with the evaporation and addition of solvent. All experiments were carried out under a continuous argon purge. Additional solvent was added to the sample periodically during the experiments because of evaporation.

5.4 Results

In the ultrafast spectroscopic data shown and discussed below, we do not see any indication of the C-H bond activation steps. This is a reasonable observation since the bond activation steps were observed on the nanosecond to millisecond timescale in the exper-

iments with $Tp^*Rh(CO)_2$ discussed above. With this information, the discussion below focuses on the early time dynamics of the transition-metal boryl complexes with a special focus on the branching ratios (percentage of complexes that form each transient intermediate) and the connection between these ratios and the observed experimental yields for the various metal boryl complexes prepared by Hartwig and co-workers.

Upon irradiation of the sample with 266 nm light, there are multiple photochemical reaction channels for the metal-boryl complexes. The primary photoprocesses are the formation of a seventeen electron, metal radical via the homolytic cleavage of the metal-boryl bond and the formation of a 16 electron unsaturated metal center via the loss of a single carbonyl ligand. In alkane solutions, the radical species is long lived and will either recombine with the boryl radical to reform the starting material or combine with another metal radical complex to form a metal dimer.(101) Although Hartwig and coworkers have eliminated the possibility that radical formation is involved in the C-H bond activation process, it may be an alternative pathway that results in lower reaction yields. The other pathway involves the formation of an unsaturated metal center which will either be solvated by an alkane ligand from the bath or will self-solvate. In self-solvation, the oxygen atom of the boryl group σ bonds to the unsaturated metal center. Figure 5.8 shows these possibilities for a model tungsten complex: $CpW(CO)_3$[Bpin'] (Cp = C_5H_5, Bpin' = $BO_2C_2H_4$). In the figure, the calculated enthalpies are referenced to the starting material which is assigned an enthalpy of zero. The radical pathways are not shown in the figure because they will be diffusion limited (on the order of microseconds) and will, therefore, not be observed in our ultrafast experiment. Spectra were collected for all three metal-boryl complexes: $Cp^*Fe(CO)_2$[Bcat$(Me)_2$], $Cp^*W(CO)_3$[Bcat$(Me)_2$], and $Cp^*W(CO)_3$[Bpin] under various experimental conditions. The results of each experiment are discussed below.

5.4.1 $Cp^*Fe(CO)_2$[Bcat$(Me)_2$]

The UV-pump, IR-probe spectra for $Cp^*Fe(CO)_2$[Bcat$(Me)_2$] in pentane at increasing delay times after photoexcitation are shown in Figure 5.9. A number of features are visible in the spectra. Two bleaches are observed at 1951 and 2004 cm^{-1} corresponding to the symmetric and antisymmetric stretching vibrations of the parent molecule respectively.

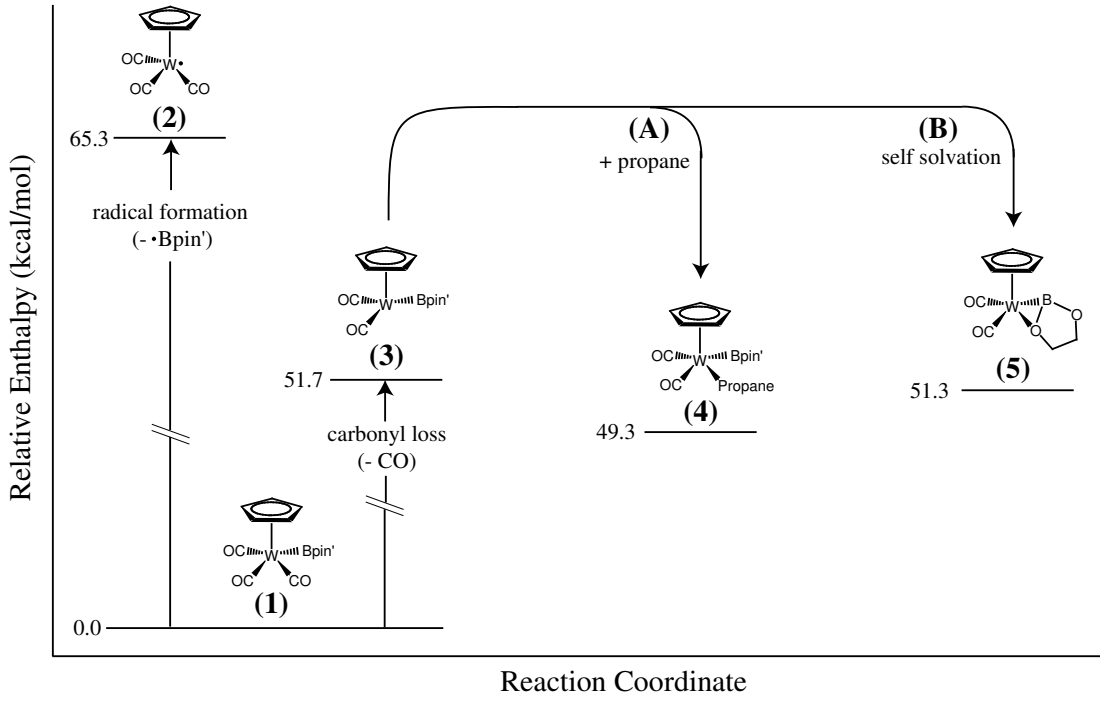

Figure 5.8. Possible ultrafast reaction pathways for $CpW(CO)_3$[Bpin'] after photoexcitation. The pentane solvated complex (**4**) is a three center, agostic bond as discussed in previous chapters. Enthalpy values shown were calculated using DFT on the model complex $CpW(CO)_3$[Bpin'] and have been normalized such that the starting material has an enthalpy value of zero.

Peak Position (cm^{-1})	Time Constant (ps)
1910	undetermined
1928	$\tau_{rise} = 2.6 \pm 0.1$
	$\tau_{decay} = 170 \pm 10$
1936	$\tau_{rise} = 18 \pm 1$
	$\tau_{decay} = 25 \pm 1$
1946	$\tau_{decay} = 25 \pm 1$
	$\tau_{rise} = 670 \pm 40$
1951	$\tau_{decay} = 39 \pm 2$
	$\tau_{rise} = 280 \pm 20$
1960	$\tau_{decay} = 1.0 \pm 0.1$
	$\tau_{decay} = 24 \pm 1$
1979	$\tau_{rise} = 7.3 \pm 0.6$
	$\tau_{decay} = 28.3 \pm 0.6$
1992	$\tau_{rise} = 13 \pm 2$
	$\tau_{decay} = 33 \pm 1$
	$\tau_{decay} = 350 \pm 30$
2004	$\tau_{rise} = 13 \pm 1$
	$\tau_{rise} = 260 \pm 10$
2013	$\tau_{decay} = 6 \pm 1$
	$\tau_{decay} = 480 \pm 70$

Table 5.2. Peak positions and kinetic data for $Cp^*Fe(CO)_2(Bcat(Me)_2)$ in pentane. Undetermined time constants are due to the low signal to noise ratio of the absorption. In these cases, the fitting routine did not converge and/or the errors in the fit were unphysically large. Errors are 95% confidence intervals with all parameters fixed except time constants.

New absorptions are visible at around 1910, 1928, 1936, 1946, 1960, 1979, 1992, and 2013 cm^{-1}. Additionally, the appearance of two additional bleaches can be seen in the spectra at 1987 and 2031 cm^{-1}. Table 5.2 summarizes the peak positions and kinetic behavior for all spectral features.

The small, broad peak at 1910 cm^{-1} and the larger peak at 1979 cm^{-1} correspond to the appearance of an iron radical complex, $Cp^*Fe(CO)_2$, in agreement with the literature values of 1913 and 1983 cm^{-1}.(102) The large absorption at 1928 cm^{-1} is attributed to the formation of a solvated carbonyl loss complex, $Cp^*Fe(CO)(Bcat(Me)_2)$(pentane). This complex is the precursor to C-H activation as discussed above and is expected to have a long lifetime and a large absorption cross-section in agreement with our experimental findings. Further, the calculated absorption frequency for the analogous CpFe(CO)[Bcat](propane)

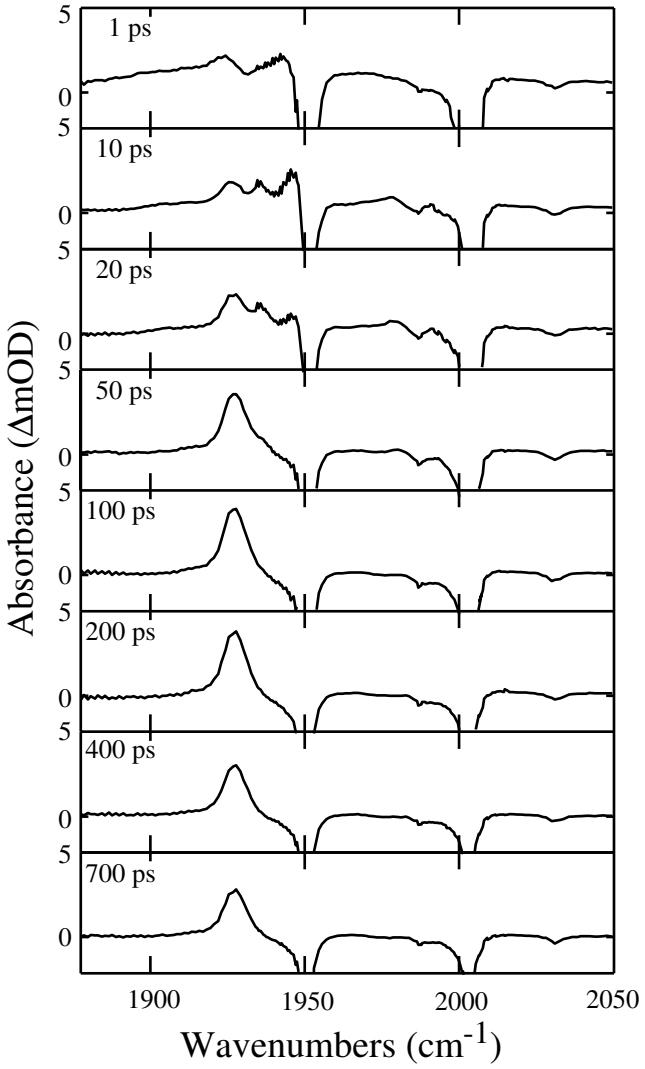

Figure 5.9. Spectra of $Cp^*Fe(CO)_2[Bcat(Me)_2]$ in pentane at increasing delay times after excitation with 266 nm light.

complex is in the same region of the spectrum. The two peaks that are on the low energy side of the two bleaches, at 1946 and 1992 cm^{-1}, are assigned to the hot parent complex. These peaks decay within the first 50 ps after photoexcitation, consistent with the vibrational relaxation time of organometallic complexes of this type.

In assigning the remaining absorptions, the newly formed bleaches (1931, 1987, 2031 cm^{-1}) are an instructive starting point. It is expected that at long times, the radical will lead to the formation of iron dimers and iron hydrides, $Cp^*_2Fe_2(CO)_4$ and $Cp^*Fe(CO)_2(H)$ respectively. The trans-dimer has characteristic absorptions at 1762 and 1931 cm^{-1}(102) and the hydride absorbs at 1933 and 1994 cm^{-1}.(103) The small bleach (around 1930 cm^{-1}) that increases in amplitude as the sample is pumped is most likely due to the formation of the iron dimer. Further evidence for this conclusion is that the broad peak at 1910 cm^{-1} and the small peak at 1979 cm^{-1} increase in amplitude as the sample degrades; since the formation of a dimer will result in an increase in radical formation,(104) this is consistent with the conclusion that the concentration of iron dimers increases as the experiment progresses. Figure 5.10 shows the spectra of the sample at the end of a data collection set. The figure demonstrates the large increase in the bleach intensities at 1931, 1987 and 2031 cm^{-1} as well as an increase in the amplitude of the radical absorptions at 1910 and 1979 cm^{-1}.[1]

There are four remaining features in the spectrum which cannot be definitively assigned to particular species at this time. The peak at 1936 cm^{-1} rises quickly and then displays a monoexponential decay with a time constant of 30 ± 10 ps. This peak is in the region where one would expect to see the solvated $[Bcat(Me)_2]^-$ loss complex, $[Cp^*Fe(CO)_2(pentane)]^+$, but this would involve the heterolytic cleavage of the iron-boryl bond in the starting material to form a cationic iron complex which is unlikely due to the high energetic barrier. The other possibility is that this peak is indicative of the self-solvated complex. The peak on the high energy side of the bleach at 1960 cm^{-1} may be the iron triplet that is formed through CO loss from the parent complex based on DFT calculations that we have carried out. Such a triplet, however, would be expected to have a long lifetime in alkane solution (ms - s)(74) which is not observed in our experiments. The small positive absorption on the high energy

[1] An FTIR spectrum collected at the end of an experiment would allow for the definitive assignment of the dimer absorption. This cannot be collected due to the air sensitive nature of the sample and the difference between ultrafast and FTIR cells.

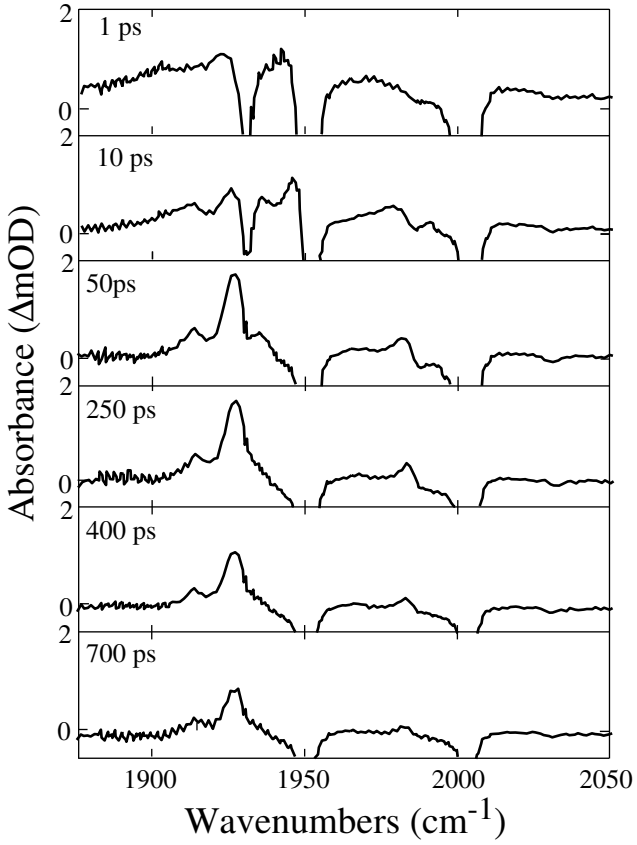

Figure 5.10. Spectra of $Cp^*Fe(CO)_2[Bcat(Me)_2]$ in pentane at increasing delay times after excitation with 266 nm light after five hours of sample pumping.

side of the second bleach (at 2013 cm^{-1}) does not correspond to any species that we expect to observe for this reaction. It is possible, that this peak results from a reaction of one of the product species that accumulates during the course of the experiment or that it is not a true feature and results only from the noise of the experimental data. Finally, the small bleach that appears at 2031 cm^{-1} is not attributable to any known product complex at this time.

5.4.2 $Cp^*W(CO)_3$[Bpin]

Three different sets of UV-pump, IR-probe spectra for $Cp^*W(CO)_3$[Bpin] were collected. Spectra of $Cp^*W(CO)_3$[Bpin] in pentane at increasing delay times after photoexcitation with 266 nm are shown in Figure 5.11; the peak positions and time constants from kinetic fits are given in Table 5.3. The spectra for $Cp^*W(CO)_3$[Bpin] in 1-hexene at increasing delay times after photoexcitation with 266 nm light are shown in Figure 5.12; the peak positions and time constants from kinetic fits are given in Table 5.4. Finally, the spectra for $Cp^*W(CO)_3$[Bpin] in pentane at increasing delay times after photoexcitation with 400 nm light are shown in Figure 5.13; the peak positions and time constants from the kinetic fits are given in Table 5.5

All three sets of data display similar features. Three bleaches, corresponding to the one symmetric and two antisymmetric bands of the parent complex are observed at 1899, 1914, and 1999 cm^{-1}. New absorptions are visible at 1845, 1887, 1933, and 1974 cm^{-1}. In the 1-hexene data, the peak at 1845 cm^{-1} is obscured by the 1-hexene absorption and is, therefore, not isolated for kinetic fitting. The peaks at 1887 and 1974 cm^{-1} are attributable to the formation of a tungsten radical, $Cp^*W(CO)_3$, in agreement with published values of 1887 and 1984 cm^{-1}.(105) The peaks at 1845 and 1933 cm^{-1} are assigned by us as the solvated carbonyl loss product. It is also questionable whether or not there is a small peak to the low energy side of the 1845 cm^{-1} absorption, a peak between those at 1887 and 1933 cm^{-1}, and another peak between those at 1945 and 1980 cm^{-1}; a discussion of the possibility of these peaks will follow.

After photolysis, the excited metal complex can dissociate the boryl radical group to

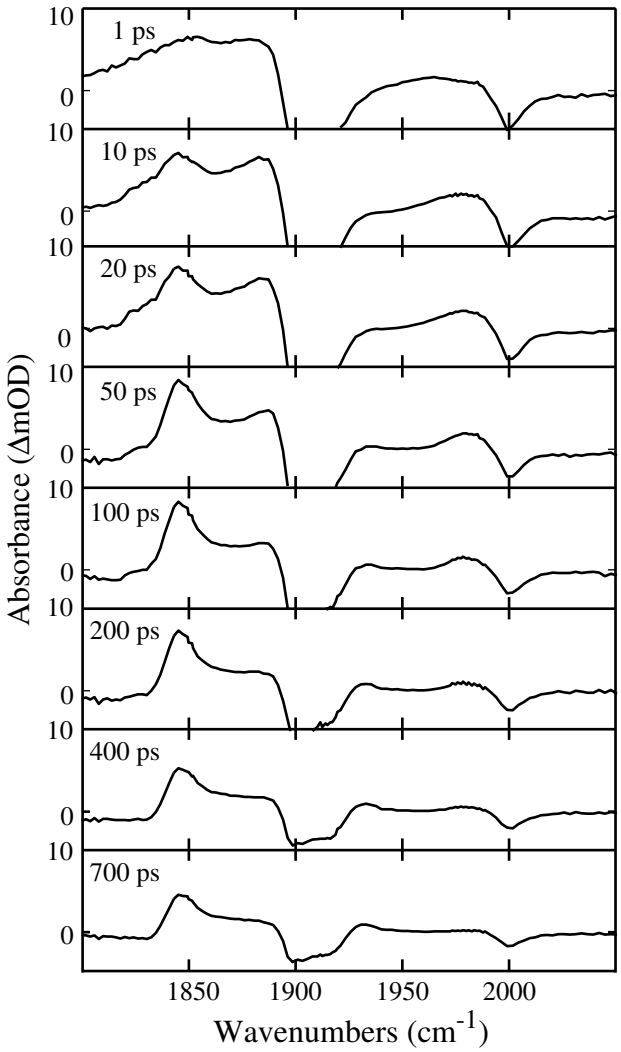

Figure 5.11. Spectra of $Cp^*W(CO)_3[Bpin]$ in pentane at increasing delay times after excitation with 266 nm light.

Peak Position (cm^{-1})	Time Constant (ps)
1845	$\tau_{rise} = 25 \pm 4$
	$\tau_{decay} = 290 \pm 20$
1887	$\tau_{rise} = 21 \pm 3$
	$\tau_{decay} = 22 \pm 3$
	$\tau_{decay} = 290 \pm 80$
1899	$\tau_{rise} = 16 \pm 5$
	$\tau_{rise} = 670 \pm 40$
1914	$\tau_{rise} = 32 \pm 5$
	$\tau_{rise} = 340 \pm 20$
1933	$\tau_{rise} = 39 \pm 3$
1978	$\tau_{rise} = 5 \pm 1$
	$\tau_{decay} = 230 \pm 10$
1999	$\tau_{rise} = 35 \pm 9$
	$\tau_{rise} = 380 \pm 50$

Table 5.3. Peak positions and kinetic data for $Cp^*W(CO)_3$[Bpin] in pentane after photoexcitation with 266 nm light. Errors are 95% confidence intervals with all parameters except time constants fixed.

Peak Position (cm^{-1})	Time Constant (ps)
1882	$\tau_{rise} = 4.2 \pm 0.7$
	$\tau_{decay} = 52 \pm 5$
	$\tau_{decay} = 330 \pm 50$
1899	$\tau_{rise} = 22 \pm 5$
	$\tau_{rise} = 250 \pm 20$
1914	$\tau_{rise} = 33 \pm 5$
	$\tau_{rise} = 380 \pm 30$
1933	$\tau_{rise} = 46 \pm 5$
1978	$\tau_{rise} = 8 \pm 3$
	$\tau_{decay} = 50 \pm 30$
	$\tau_{decay} = 290 \pm 80$
1999	$\tau_{rise} = 35 \pm 5$
	$\tau_{rise} = 190 \pm 20$

Table 5.4. Peak positions and kinetic data for $Cp^*W(CO)_3$[Bpin] in 1-hexene after photoexcitation with 266 nm light. Errors are 95% confidence intervals with all parameters except time constants fixed.

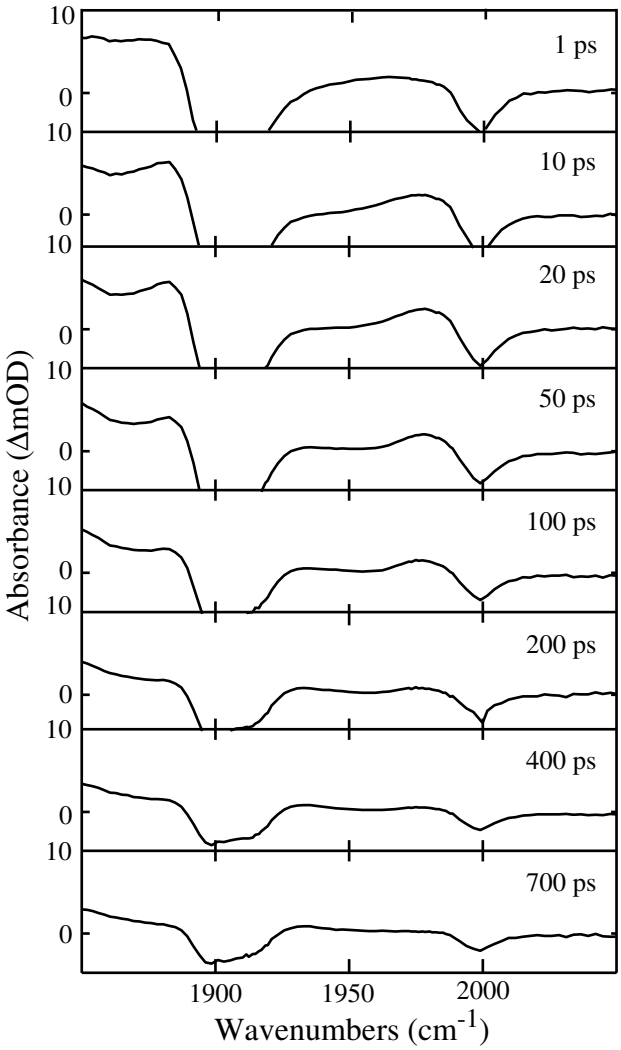

Figure 5.12. Spectra of $Cp^*W(CO)_3[Bpin]$ in 1-hexene at increasing delay times after excitation with 266 nm light. The low energy region of the spectra is not included because of the large solvent absorption in this region.

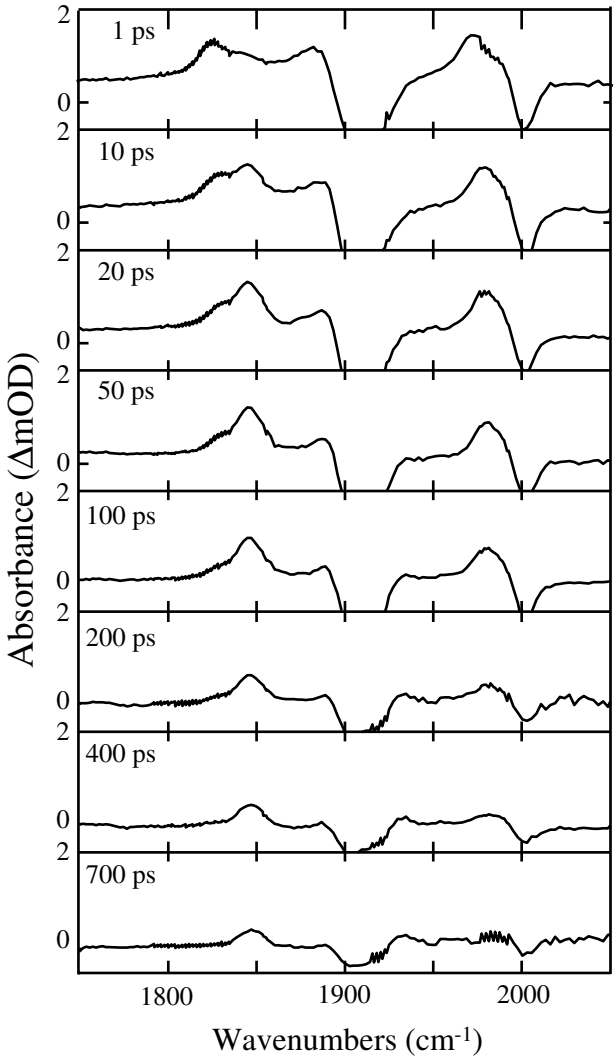

Figure 5.13. Spectra of $Cp^*W(CO)_3[Bpin]$ in pentane at increasing delay times after excitation with 400 nm light.

Peak Position (cm^{-1})	Time Constant (ps)
1826	$\tau_{decay} = 21 \pm 5$
	$\tau_{decay} = 205 \pm 9$
1843	$\tau_{rise} = 10 \pm 2$
	$\tau_{decay} = 220 \pm 10$
1885	$\tau_{decay} = 110 \pm 10$
1899	$\tau_{decay} = 4 \pm 2$
	$\tau_{rise} = 370 \pm 50$
1914	$\tau_{rise} = 700 \pm 100$
1931	undetermined
1976	$\tau_{decay} = 190 \pm 20$
1999	$\tau_{rise} = 380 \pm 80$

Table 5.5. Peak positions and kinetic data for $Cp^*W(CO)_3$[Bpin] in pentane after photoexcitation with 400 nm light. Undetermined time constants are due to the low signal to noise ratio of the absorption. In these cases, the fitting routine did not converge and/or the errors in the fit were unphysically large. Errors reported are 95% confidence intervals with all parameters except time constants fixed.

give the tungsten radical identified above or it can dissociate a carbonyl group as discussed previously. The unsaturated metal center will react quickly with a nearby molecule to provide increased stability. In the case of $Cp^*W(CO)_2$[Bpin] in pentane, there are two foreseeable pathways for solvation. The first pathway is solvation by a surrounding pentane molecule. This complex is the C-H activation precursor. The second pathway involves self-solvation. We have calculated the relative energy for each step in the reaction and the vibrational frequencies associated with each complex. Figure 5.8 shows the reaction pathways and the relative enthalpy of each complex (with respect to the starting complex). The calculated vibrational frequencies for the complexes are given in Table 5.6. The pentane solvated complex and the self-solvated complex should be visible at early times. Because the pentane-solvated complex is more favorable energetically, the self-solvated species should eventually all convert into the pentane-solvated complexes. This pentane-solvated complex can then go on to react in the primary C-H activation pathway. The small peaks on the blue side of the 1845 cm^{-1} absorption and on the red side of the 1980 cm^{-1} absorption are attributed to the self-solvation complex.

A comparison of the spectra for $Cp^*W(CO)_3$[Bpin] in pentane and 1-hexene (both pumped with 266 nm light) indicates that all aspects of the dynamics are very similar. This

Complex	Absorption Frequency (cm^{-1}
(1)	1915 (1.00)
	1928 (0.45)
	2000 (0.52)
(2)	1906 (1.00)
	1907 (0.69)
	1989 (0.51)
(3)	1882 (0.90)
	1954 (1.00)
(4)	1874 (0.97)
	1938 (1.00)
(5)	1880 (1.00)
	1946 (0.93)

Table 5.6. Calculated absorption frequencies for $CpW(CO)_3$[Bpin']. Complex numbers refer to the number assigned to each species in Figure 5.8. Normalized absorption intensities are given in parentheses. For calculation simplicity Cp (C_5H_5) and Bpin' ($BO_2C_2H_4$) were used instead of Cp^* and Bpin and propane was used as the solvent instead of pentane.

is not surprising since the only difference in the interaction should be an increased binding energy to the double bond of the alkene as compared with the alkyl group of the alkane. As discussed in Chapter 3, the vibrational frequency of a metal complex solvated by an unsaturated hydrocarbon is very similar to the vibrational frequency of the metal complex solvated by a saturated hydrocarbon. With a similar vibrational frequency, the infrared signatures of these distinct complexes overlap and cannot be distinguished spectroscopically.

A comparison of the spectra taken after photoexcitation with 266 nm and 400 nm light is more interesting. Although all of the same features are present, the intensities of the absorptions are different. The molar absorptivity at 400 nm is very small which results in a small population of reactive complexes. Experimentally, this results in a set of spectra with a very low signal-to-noise ratio. The most notable difference in the spectra obtained with the 266 nm and the 400 nm pump beams is the existence and behavior of the peak at 1826 cm^{-1}. This peak has the most intense absorption at early times and quickly decays. Such a feature is not observed (or is very weak) in spectra obtained using a 266 nm pump beam. The identity of this peak has not been determined. Another difference in the 400 nm data is that the absorption assigned to the radical complex at 1974 cm^{-1} increases in amplitude with respect to the data collected using 266 nm pump light. Interestingly, the

second radical peak, at 1887 cm^{-1} does not increase in amplitude. This seems to be an experimental artifact that results from the fact that the sample quickly degrades and the high energy region of the spectrum was collected before the low energy region. When data is collected, one region of the spectrum is sampled at a time to minimize the effects of sample degradation on kinetic data. A spectrum collected at one delay time shows growth of both radical peaks as one would expect. The other peaks in the low energy region of the spectrum demonstrate similar behavior.

5.4.3 $Cp^*W(CO)_3[Bcat(Me)_2]$

Similar to the data collected for $Cp^*W(CO)_3[Bpin]$, three different data sets were collected for $Cp^*W(CO)_3[Bcat(Me)_2]$. The UV-pump, IR-probe spectra for $Cp^*W(CO)_3[Bcat(Me)_2]$ in pentane at increasing delay times after photoexcitation with 266 nm are shown in Figure 5.14 with the corresponding peak positions and kinetic data given in Table 5.7. A similar set of spectra for $Cp^*W(CO)_3[Bcat(Me)_2]$ in 1-hexene after photoexcitation with 266 nm light are shown in Figure 5.15 with the peak positions and kinetic data given in Table 5.8. Spectra for $Cp^*W(CO)_3[Bcat(Me)_2]$ in pentane after photoexcitation with 400 nm light are shown in Figure 5.16 with the peak positions and kinetic data given in Table 5.9.

The data for $Cp^*W(CO)_3[Bcat(Me)_2]$ are very similar to those recorded for $Cp^*W(CO)_3[Bpin]$. Two parent bleaches are observable around 1925 and 2014 cm^{-1}. A third bleach, to the red of the 1925 cm^{-1} absorption is not seen. To verify the sample integrity, a static FTIR of the sample was taken and is shown in Figure 5.17. The dashed line in the figure shows the ultrafast spectrum (collected at 200 ps after photoexcitation) and the solid line is the static FTIR spectrum without excitation. The FTIR clearly shows the presence of the third parent complex absorption. The absence of this absorption in the ultrafast data indicates that the parent bleach is masked by an strong, overlapping absorption.

The metal radical complex that results from homolytic cleavage of the metal-boryl bond is again identified by the two absorptions at around 1885 and 1985 cm^{-1}. The two

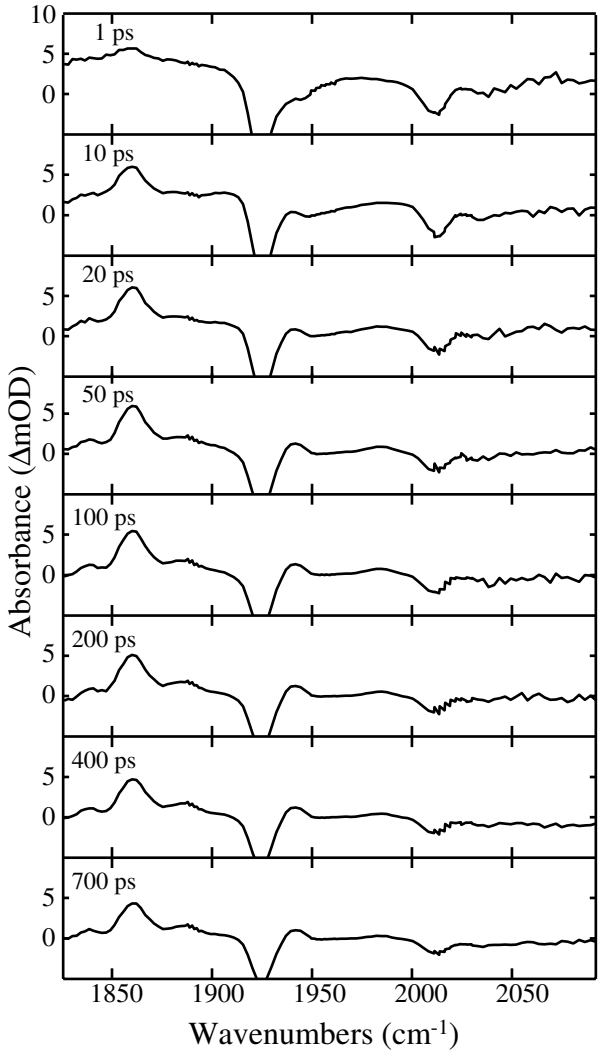

Figure 5.14. Spectra of $Cp^*W(CO)_3[Bcat(Me)_2]$ in pentane at increasing delay times after excitation with 266 nm light.

Peak Position (cm^{-1})	Time Constant (ps)
1839	$\tau_{decay} = 7 \pm 2$
	$\tau_{decay} = 110 \pm 40$
1860	$\tau_{rise} = 6 \pm 2$
	$\tau_{decay} = 240 \pm 30$
1888	$\tau_{decay} = 7 \pm 1$
	$\tau_{decay} = 130 \pm 20$
1909	$\tau_{decay} = 19 \pm 1$
1925	$\tau_{rise} = 15 \pm 5$
	$\tau_{rise} = 270 \pm 30$
1942	$\tau_{rise} = 14 \pm 1$
	$\tau_{decay} = 360 \pm 30$
1985	$\tau_{decay} = 18 \pm 2$
	$\tau_{decay} = 170 \pm 30$
1998	$\tau_{decay} = 23 \pm 2$
2014	$\tau_{rise} = 20 \pm 10$
	$\tau_{rise} = 340 \pm 100$

Table 5.7. Peak positions and kinetic data for $Cp^*W(CO)_3[Bcat(Me)_2]$ in pentane after photoexcitation with 266 nm light. Errors are 95% confidence intervals with all parameters except time constants fixed.

Peak Position (cm^{-1})	Time Constant (ps)
1858	$\tau_{decay} = 3 \pm 1$
	$\tau_{decay} = 190 \pm 40$
1882	$\tau_{decay} = 3 \pm 1$
	$\tau_{decay} = 170 \pm 30$
1923	undetermined
1939	$\tau_{rise} = 13 \pm 3$
	$\tau_{decay} = 400 \pm 50$
1982	$\tau_{decay} = 9 \pm 2$
	$\tau_{decay} = 100 \pm 20$
2011	undetermined
2024	$\tau_{decay} = 32 \pm 4$

Table 5.8. Peak positions and kinetic data for $Cp^*W(CO)_3[Bcat(Me)_2]$ in 1-hexene after photoexcitation with 266 nm light. Undetermined time constants are due to the low signal to noise ratio of the absorption. In these cases, the fitting routine did not converge and/or the errors in the fit were unphysically large. Errors are 95% confidence intervals with all parameters except time constants fixed.

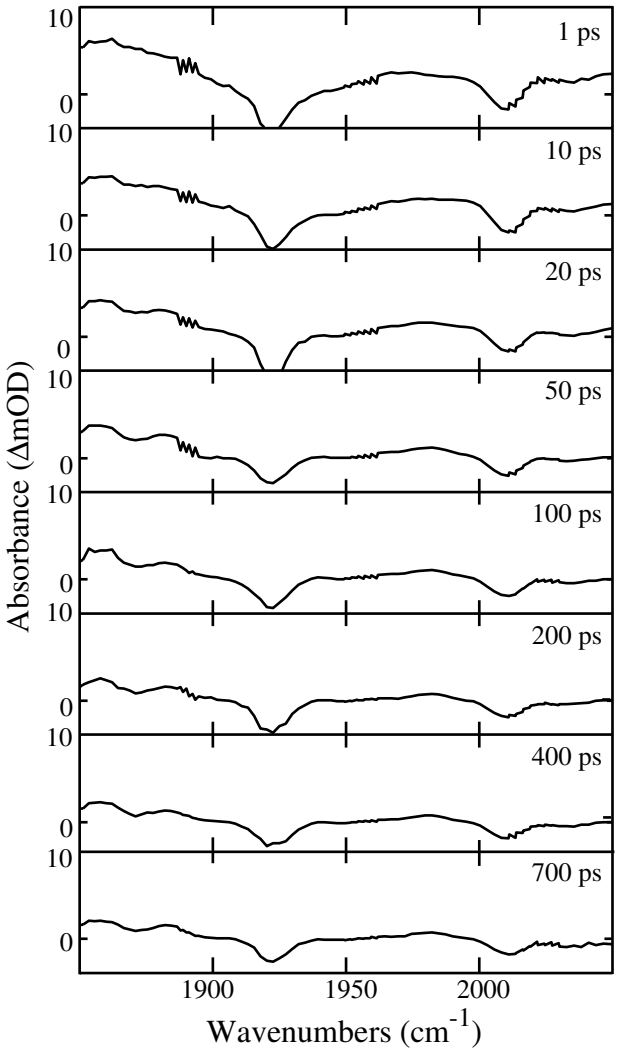

Figure 5.15. Spectra of $Cp^*W(CO)_3[Bcat(Me)_2]$ in 1-hexene at increasing delay times after excitation with 266 nm light. The low energy region of the spectra is not included because of the large solvent absorption in this region.

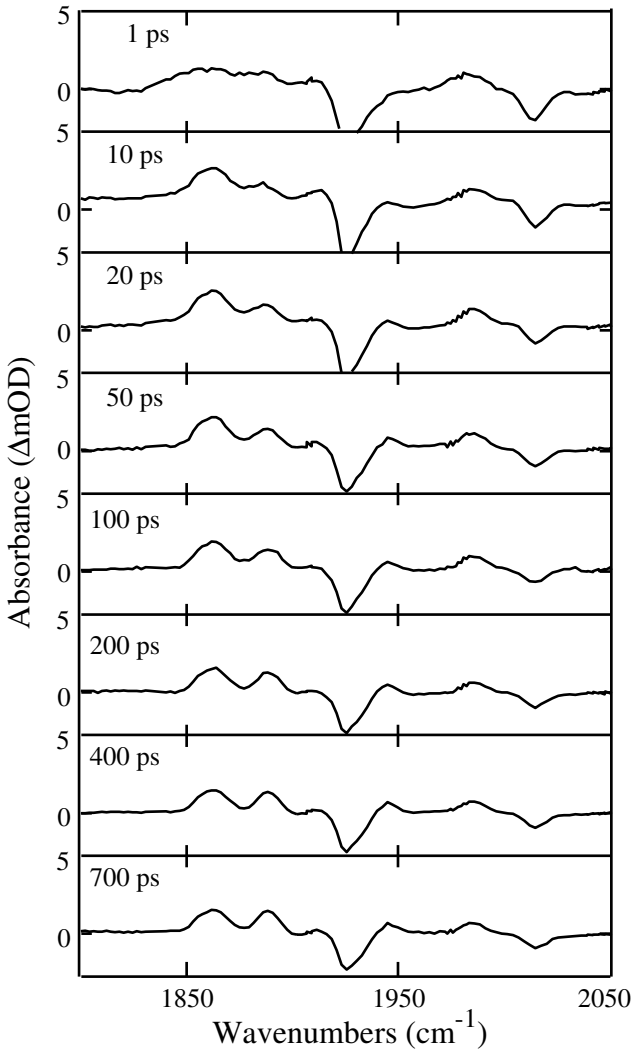

Figure 5.16. Spectra of $Cp^*W(CO)_3[Bcat(Me)_2]$ in pentane at increasing delay times after excitation with 400 nm light.

Peak Position (cm^{-1})	Time Constant (ps)
1840	$\tau_{decay} = 33 \pm 8$
1855	$\tau_{decay} = 90 \pm 20$
1864	$\tau_{decay} = 96 \pm 9$
1888	$\tau_{decay} = 50 \pm 30$
1912	$\tau_{decay} = 28 \pm 6$
1926	$\tau_{rise} = 60 \pm 20$
1945	undetermined
1986	$\tau_{rise} = 60 \pm 10$
2015	undetermined

Table 5.9. Peak positions and kinetic data for $Cp^*W(CO)_3[Bcat(Me)_2]$ in pentane after photoexcitation with 400 nm light. Undetermined time constants are due to the low signal to noise ratio of the absorption. In these cases, the fitting routine did not converge and/or the errors in the fit were unphysically large. Errors are 95% confidence intervals with all parameters except time constants fixed.

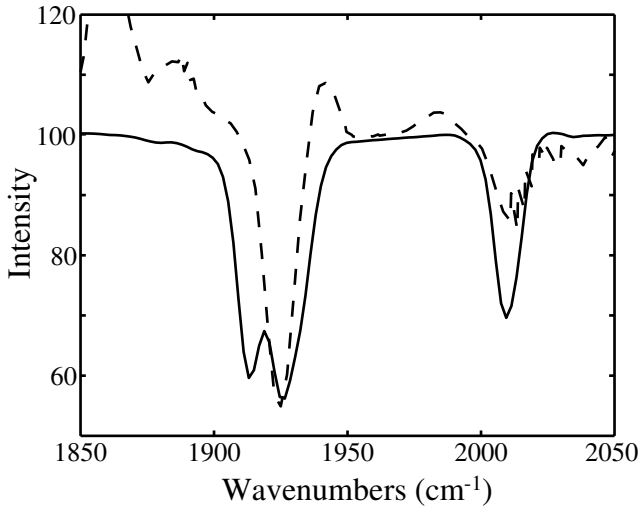

Figure 5.17. Static FTIR spectrum of $Cp^*W(CO)_3[Bcat(Me)_2]$ in pentane overlayed onto the spectrum collected 200 ps after photoexcitation. The solid line is the solvent subtracted FTIR spectrum in pentane and the dashed line is the difference spectrum taken 200 ps after photoexcitation. The FTIR spectrum is inverted (transmission) and the difference spectrum has been amplified by a factor of seven and shifted so that the two overlap.

peaks observed near 1858 and 1940 cm^{-1} are again attributed to the solvated complex and the other absorption around 1840 cm^{-1} has not been attributed to any known complex. Additionally, it is expected that there is a large positive absorption around 1910 cm^{-1} which is masking the third bleach. There is indication of a small bleach around 2030 cm^{-1} that is probably due to the formation of the hydride complex as was observed in the case of the $Cp^*Fe(CO)_2[Bcat(Me)_2]$ complex; the energy of this absorption is comparable to the literature value of 2013 cm^{-1}.(106)

The experiment carried out in 1-hexene with 266 nm excitation shows an increase in the amount of radical complex formed. Because the branching ratio between the carbonyl loss complex and the radical complex should not be solvent dependent, this change in the radical concentration appears to be an experimental artifact that could result from different conditions including, but not limited to, pump intensity, sample concentration, sample purity, and the maintenance of a water free environment throughout the experiment. The 400 nm pump wavelength experiments indicate that the formation of all complexes is much smaller than when 266 nm excitation is used. Even when the spectra are scaled such that the parent bleach intensities are equal, the intermediate population is about 20% of that in the other experiments. This is surprising only in the context of the results for $Cp^*W(CO)_3[Bpin]$ which does not show such dynamics.

5.5 Conclusions

The ultrafast, infrared spectroscopic data outlined above provides a puzzling picture of the early time dynamics for transition-metal boryl chemistry. The most interesting aspect of the results discussed in this chapter is the obvious presence of metal radical species. These complexes were ruled out as possible precursors in the C-H activation pathway, but are definitely formed upon irradiation with ultraviolet light. The radical formation may provide information about why certain metal complexes are better at activating C-H bonds than others.

In order to obtain a picture of the mechanism of C-H activation as mediated by transition-metal boryl complexes, longer time dynamics must be obtained. The capabil-

ities of the instrument utilized here do not allow for the collection of data more than 800 ps after photoexcitation. Dynamics which take place on the nanosecond to microsecond timescales are expected to provide the key information for this project. In addition to allowing for the identification of the C-H activation precursors, long time dynamics may also shed light into the nature of the ultrafast data. In the current data sets, there do not appear to be any new absorptions growing in; this makes identification difficult. It is possible, that on a longer timescale new intermediates and/or products form and will aid in the characterization of remaining peaks.

Chapter 6

Conclusions

Complex reaction dynamics in solution have been extensively studied by our group and this thesis serves to expand on this wealth of information. In the solution phase, organometallic complexes are monitored via their carbonyl stretching frequencies with infrared light. This experimental scheme allows for a more definitive assignment of transient species since the absorptions are sharp and highly sensitive. Monitoring chemical reactions in real time, under the conditions that they are carried out in synthetic laboratories, provides important information that can aid in the control of chemical synthesis.

This thesis has outlined the construction of an ultrafast, ultra-violet pump, infrared-probe experimental apparatus and its use in elucidating the details of three complex, organometallic reaction pathways. Such an experimental apparatus is obviously vital in determining the early time dynamics of these reactive complexes. In Chapter 3, the apparatus was utilized to investigate the formation of a vinylidene-metal complex. Although the vinylidene-metal complex was not observed to form within the first millisecond after photoexcitation, we show that alkyne polymerization reactions have early, previously unstudied, rearrangement dynamics. These rearrangement dynamics mimic those of alcohols as discussed in Chapter 4. As a ubiquitous process, rearrangement was investigated with theoretical modeling using the Langevin Equation. Our results indicate that the prevailent labels for rearrangement, chainwalk and stochastic, are insufficiently different and cannot

be definitively assigned to the physical observations. In Chapter 5, ultrafast studies are carried out on various transition-metal boryl complexes to investigate the mechanism of carbon-hydrogen bond activation. The ultrafast spectroscopic results indicate the formation of two photoproducts which then go on to react along separate pathways. The primary C-H activation steps are slower than the ultrafast time scale and must be studied using step-scan FTIR.

The work described here can be extended to many future studies. The vinylidene formation of Chapter 3 can be investigated using multiphoton excitation; such an experiment would allow for a determination of whether or not the reaction is thermally accessible. The theoretical investigations of Chapter 4 can be expanded to include the structure of the solvent cage with molecular dynamics simulations. Finally, the C-H activation reactions of transition-metal boryl complexes will have to be studied using step-scan FTIR in order to look at the reactivity on a longer time scale. Once the longer time data has been collected, it will be simpler to assign the basic photoprocesses observed on the ultrafast time scale.

Bibliography

[1] Labinger, J. A.; Bercaw, J. E. *Nature* **2002**, *417*, 507–514.

[2] Arndtsen, B. A.; Bergman, R. G.; Mobley, T. A.; Peterson, T. H. *Acc. Chem. Res.* **1995**, *28*, 154–162.

[3] Donaldson, W. A.; John Wiley and Sons, Ltd.: Chichester, England, 2000.

[4] Crabtree, R. H. *The Organometallic Chemistry of the Transition Metals;* John Wiley and Sons, Ltd.: New York, 2001.

[5] Semmelhack, M. E.; Chlenov, A.; Ho, D. M. *J. Amer. Chem. Soc.* **2005**, *127*, 7759–7773.

[6] Bitterwolf, T. E. *J. Organomet. Chem.* **2004**, *689*, 3939–3952.

[7] Andrews, L., Moskovits, M., Eds. *Chemistry and Physics of Matrix-Isolated Species;* Elsevier Science Publishers: The Netherlands, 1989.

[8] Gielen, M., Willem, R., Wrackmeyer, B., Eds. *Advanced Applications of NMR to Organometallic Chemistry;* John Wiley and Sons, Ltd., 1996.

[9] Bruneau, C.; Dixneuf, P. H. *Acc. Chem. Res.* **1999**, *32*, 311–323.

[10] Szymanska-Buzar, T.; Downs, G. J.; Greene, T. M.; Marshall, A. S. *J. Organomet. Chem.* **1995**, *495*, 149–161.

[11] Szymanska-Buzar, T.; Downs, G. J.; Greene, T. M.; Marshall, A. S. *J. Organomet. Chem.* **1995**, *495*, 163–175.

[12] Reid, G. D.; Wynne, K.; John Wiley and Sons, Ltd.: Chichester, 2000; chapter Ultrafast Laser Technology and Spectroscopy.

[13] Payne, C. K. *Ultrafast Infrared Studies of Complex Ligand Rearrangements in Solution* PhD thesis, University of California, Berkeley, **2003**.

[14] Baerends, E. J.; Rosa, A. *Coord. Chem. Rev.* **1998**, *177*, 97–125.

[15] Simon, J. D.; Xie, X. *J. Phys. Chem.* **1986**, *90*, 6751–6753.

[16] Simon, J. D.; Xie, X. *J. Phys. Chem.* **1987**, *91*, 5538–5540.

[17] Joly, A. G.; Nelson, K. A. *Chem. Phys.* **1991**, *152*, 69–82.

[18] King, J. C.; Zhang, J. Z.; Schwartz, B. J.; Harris, C. B. *J. Chem. Phys.* **1993**, *99*, 7595–7601.

[19] Owrutsky, J. C.; Rafery, D.; Hochstrasser, R. M. *Ann. Rev. Phys. Chem.* **1994**, *45*, 519–555.

[20] Stratt, R. M.; Maroncelli, M. *J. Phys. Chem.* **1996**, *100*, 12981–12996.

[21] Morse, J. M.; Parker, G. H.; Burkey, T. J. *Organometallics* **1989**, *8*, 2471–2474.

[22] Weitz, E. *J. Phys. Chem.* **1994**, *98*.

[23] Harris, A. L.; Brown, J. K.; Harris, C. B. *Ann. Rev. Phys. Chem* **1988**, pages 341–366.

[24] Gaussian 03, Revision C.02. Frisch, M. J.; Trucks, G. W.; Schlegel, H. B.; Scuseria, G. E.; Robb, M. A.; Cheeseman, J. R.; Montgomery, Jr., J. A.; Vreven, T.; Kudin, K. N.; Burant, J. C.; Millam, J. M.; Iyengar, S. S.; Tomasi, J.; Barone, V.; Mennucci, B.; Cossi, M.; Scalmani, G.; Rega, N.; Petersson, G. A.; Nakatsuji, H.; Hada, M.; Ehara, M.; Toyota, K.; Fukuda, R.; Hasegawa, J.; Ishida, M.; Nakajima, T.; Honda, Y.; Kitao, O.; Nakai, H.; Klene, M.; Li, X.; Knox, J. E.; Hratchian, H. P.; Cross, J. B.; Bakken, V.; Adamo, C.; Jaramillo, J.; Gomperts, R.; Stratmann, R. E.; Yazyev, O.; Austin, A. J.; Cammi, R.; Pomelli, C.; Ochterski, J. W.; Ayala, P. Y.; Morokuma, K.; Voth, G. A.; Salvador, P.; Dannenberg, J. J.; Zakrzewski, V. G.; Dapprich, S.; Daniels, A. D.; Strain, M. C.; Farkas, O.; Malick, D. K.; Rabuck, A. D.; Raghavachari, K.; Foresman, J. B.; Ortiz, J. V.; Cui, Q.; Baboul, A. G.; Clifford, S.; Cioslowski, J.; Stefanov, B. B.; Liu, G.; Liashenko, A.; Piskorz, P.; Komaromi, I.; Martin, R. L.; Fox, D. J.; Keith, T.; Al-Laham, M. A.; Peng, C. Y.; Nanayakkara, A.; Challacombe, M.; Gill, P. M. W.; Johnson, B.; Chen, W.; Wong, M. W.; Gonzalez, C.; Pople, J. A.

[25] Becke, A. D. *J. Chem. Phys.* **1993**, *98*, 5648–5652.

[26] Lee, C. T.; Yang, W. T.; Parr, R. G. *Phys. Rev. B* **1988**, *37*, 785–789.

[27] Stephes, P. J.; Devlin, F. J.; Chabalowski, C. F.; Frisch, M. J. *J. Phys. Chem.* **1994**, *98*, 11623–11627.

[28] Hehre, W. J.; Ditchfie, R.; Pople, J. A. *J. Chem. Phys.* **1972**, *56*, 2257.

[29] Francl, M. M.; Pietro, W. J.; Hehre, W. J. *J. Chem. Phys.* **1982**, *77*, 3654–3665.

[30] Hay, P. J.; Wadt, W. R. *J. Chem. Phys.* **1985**, *82*, 299–310.

[31] Scott, A. P.; Radom, L. *J. Phys. Chem.* **1996**, *100*, 16502–16513.

[32] Kotz, K. T. *Ultrafast Infrared Studies of Ligand Rearrangements at Coordinatively Unsaturated Group 6 Transition Metal Complexes* PhD thesis, University of California, Berkeley, **2001**.

[33] Glascoe, E. A. *in preparation* PhD thesis, University of California, Berkeley, **2006**.

[34] Hamm, P.; Kaindl, R. A.; Stenger, J. *Optics Letters* **2000**, *25*, 1798–1800.

[35] Gita, B.; Sundararajan, G. *Tetrahedron Lett.* **1993**, *34*, 6123–6126.

[36] Du Plessis, J. A. K.; Vosloo, H. C. M. *J. Mol. Catal.* **1991**, *65*, 51–54.

[37] Landon, S. J.; Shulman, P. M.; Geoffroy, G. L. *J. Am. Chem. Soc.* **1985**, *107*, 6739–6740.

[38] Szymanska-Buzar, T. *J. Mol. Catal.* **1988**, *48*, 43–47.

[39] Szymanska-Buzar, T. *J. Mol. Catal.* **1994**, *93*, 137–147.

[40] Bruce, M. I. *Chem. Rev.* **1991**, *91*, 197–257.

[41] Kotz, K. T.; Yang, H.; Snee, P. T.; Payne, C. K.; Harris, C. B. *J. Organomet. Chem.* **2000**, *596*, 183–192.

[42] Szymanska-Buzar, T.; Kern, K. *J. Organomet. Chem.* **2001**, *622*, 74–83.

[43] Connelly, N. G.; Geiger, W. E.; Lagunas, M. C.; Metz, B.; Rieger, A. L.; Rieger, P. H.; Shaw, M. J. *J. Am. Chem. Soc.* **1995**, *117*, 12202–12208.

[44] Abd-Elzaher, M. M.; Fischer, H. *J. Organomet. Chem.* **1999**, *588*, 235–241.

[45] De Angelis, F.; Sgamellotti, A. *Organometallics* **2002**, *21*, 5944–5950.

[46] Cadierno, V.; Gamasa, M. P.; Gimeno, J.; Gonzalez-Bernardo, C. *Organometallics* **2001**, *20*, 5177–5188.

[47] Birdwhistell, K. R.; Burgmayer, S. J. N.; Templeton, J. L. *J. Am. Chem. Soc.* **1983**, *105*, 7789–7790.

[48] Dougherty, T. P.; Heilweil, E. J. *J. Chem. Phys.* **1994**, *100*, 4006–4009.

[49] Dougherty, T. P.; Grubbs, W. T.; Heiweil, E. J. *J. Phys. Chem.* **1994**, *98*, 9396–9399.

[50] Periana, R. A.; Bergman, R. G. *J. Am. Chem. Soc.* **1986**, *108*, 7332–7346.

[51] Dobson, G. R.; Hodges, P. M.; Healy, M. A.; Poliakoff, M.; Turner, J. J.; Firth, S.; Asali, K. J. *J. Am. Chem. Soc.* **1987**, *109*, 4218–4224.

[52] Hall, C.; Perutz, R. N. *Chem. Rev.* **1996**, *96*, 3125–3146.

[53] Jiang, Y.; Lee, T.; Rose-Petruck, C. G. *J. Phys. Chem.* **2003**, *107*, 7524–7538.

[54] Fan, L.; Ziegler, T. *J. Phys. Chem.* **1992**, *96*, 6937–6941.

[55] Jonas, V.; Thel, W. *J. Chem. Phys.* **1995**, *102*, 8474–8484.

[56] Paur-Afshari, R.; Lin, J.; Schultz, R. H. *Organometallics* **2000**, *19*, 1682–1691.

[57] Dean, J. A. *Lange's Handbook of Chemistry;* McGraw-Hill Inc.: New York, 15th ed., 1999.

[58] Viswanath, D. S.; Natarajan, G. *Data Book on the Viscosity of Liquids;* Hemisphere Publishing Corporation: New York, 1989.

[59] Steinfeld, J. I.; Francisco, J. S.; Hase, W. L. *Chemical Kinetics and Dynamics;* Prentice Hall: Upper Saddle Rive, NJ, 2nd ed., 1998.

[60] Hansen, J. P.; McDonald, I. R. *Theory of Simple Liquids;* Academic Press: Orlando, 2nd ed., 1986.

[61] Schroeder, J.; Troe, J.; World Scientific: Singapore, 1993; chapter Solvent Effects in the Dynamics of Dissociation, Recombination, and Isomerization Reactions.

[62] Breheny, C. J.; Kelly, J. M.; Long, C.; O'Keefe, S.; Pryce, M. T.; Russell, G.; Walsh, M. M. *Organometallics* **1998**, *17*, 3690–3695.

[63] Krishnan, R.; Schultz, R. H. *Organometallics* **2001**, *20*, 3314–3322.

[64] Ladogana, S.; Nayak, S. K.; Smit, J. P.; Dobson, G. R. *Inorg. Chem.* **1997**, *36*, 650–655.

[65] Lugovskoy, S.; Lin, J.; Schultz, R. H. *Dalton Trans.* **2003**, *15*, 3103–3110.

[66] Cotton, F. A.; Wilinson, G.; Gauss, P. L. *Basic Inorganic Chemistry;* John Wiley and Sons: Toronto, 1995.

[67] Snee, P. T.; Shanoski, J. E.; Harris, C. B. *J. Am. Chem. Soc.* **2005**, *127*, 1286.

[68] Nechaev, M. S.; Rayon, V. M.; Frenking, G. *J. Phys. Chem. A* **2004**, *108*, 3134–3142.

[69] Sun, H.; Frei, H. *J. Phys. Chem. B* **1997**, *101*, 205.

[70] Schultz, R. H. *Int. J. of Chem. Kinet.* **2004**, *36*, 427–433.

[71] Shagal, A.; Schultz, R. H. *Organometallics* **2002**, *21*, 5657–5665.

[72] Xie, X.; Simon, J. D. *J. Amer. Chem. Soc.* **1990**, *112*, 1130–1136.

[73] Lawes, D. J.; Geftakis, S.; Ball, G. E. *J. Amer. Chem. Soc.* **2005**, *127*, 4134–4135.

[74] Snee, P. T.; Payne, C. K.; Mebane, S. D.; Kotz, K. T.; Harris, C. B. *J. Amer. Chem. Soc.* **2001**, *123*, 6909–6915.

[75] Simon, J. D.; Xie, X. *J. Phys. Chem.* **1989**, *93*, 291–293.

[76] Zhang, S.; Zang, V.; Bajaj, H. C.; Dobson, G. R.; van Eldik, R. *J. Organomet. Chem.* **1990**, *397*, 279–289.

[77] Schulten, K.; Schulten, Z.; Szabo, A. *J. Chem. Phys.* **1981**, *74*, 4426–4432.

[78] Wagner, C.; Kiefhaber, T. *Proc. Natl. Acad. of Sci. U. S. A.* **1999**, *96*, 6716–6721.

[79] Farrell, G. J.; Burkey, J. J. *J. Photochem. Photobiol. A* **2000**, *137*, 135.

[80] Ben-Amotz, D.; Scott, T. W. *J. Chem. Phys.* **1987**, *87*, 3739–3748.

[81] Roy, M.; Doraiswamy, S. *J. Chem. Phys.* **1993**, *98*, 3213–3223.

[82] Bauer, D. R.; Brauman, J. I.; Pecora, R. *J. Amer. Chem. Soc.* **1974**, *96*, 6840–6843.

[83] Alder, B. J.; Gass, D. M.; Wainwright, T. E. *J. Chem. Phys.* **1970**, *53*, 3813–3826.

[84] Allen, M. P.; Tildesley, D. J. *Computer Simulation of Liquids;* Oxford University Press: Oxford, 1987.

[85] Lian, T.; Bromberg, S. E.; Asplund, M. C.; Yang, H.; Harris, C. B. *J. Phys. Chem.* **1996**, *100*, 11994–12001.

[86] Dougherty, T. P.; Heilweil, E. J. *Chem. Phys. Lett.* **1994**, *227*, 19–25.

[87] Nayak, S. K.; Burkey, T. J. *Organometallics* **1991**, *10*, 3745–3750.

[88] Green, M.; O'Hare, D. *Pure Appl. Chem.* **1985**, *57*, 1897–1910.

[89] Crabtree, R. *J. Organomet. Chem.* **2004**, *689*, 4083–4091.

[90] Janowicz, A.; Bergman, R. *J. Am. Chem. Soc.* **1982**, *104*, 352–354.

[91] Hoyano, J.; Graham, W. *J. Am. Chem. Soc.* **1982**, *104*, 3723–3725.

[92] Waltz, K.; He, X.; Muhoro, C.; Hartwig, J. *J. Am. Chem. Soc.* **1995**, *117*, 11357–11358.

[93] Waltz, K.; Hartwig, J. *Science* **1997**, *277*, 211–213.

[94] Waltz, K.; Muhoro, C.; Hartwig, J. *Organometallics* **1999**, *18*, 3383–3393.

[95] Waltz, K.; Hartwig, J. *J. Am. Chem. Soc.* **2000**, *122*, 11358–11369.

[96] Chen, H.; Schlect, S.; Semple, T.; Hartwig, J. *Science* **2000**, *287*, 1995–1997.

[97] Pelter, A.; Smith, K.; Brown, H. *Borane Reagents;* Academic Press: London, 1988.

[98] Perutz, R.; Belt, S.; McCamley, A.; Whittlesey, M. *Pure Appl. Chem.* **1990**, *62*, 1539–1545.

[99] Lam, W.; Lin, Z. *Organometallics* **2003**, *22*, 473–480.

[100] Webster, C.; Fan, Y.; Hall, M.; Kunz, D.; Hartwig, J. *J. Am. Chem. Soc.* **2003**, *125*, 858–859.

[101] Virrels, I.; George, M.; Johnson, F.; Turner, J.; Westwell, J. *Organometallics* **1995**, *14*, 5203–5208.

[102] Xue, S.; Nikiforov, S.; Dedieu, A.; George, M. *Organometallics* **2001**, *20*, 1515–1520.

[103] Cheng, T.; Bullock, R. *Organometallics* **2002**, *21*, 2325–2331.

[104] George, M.; Dougherty, T.; Heilweil, E. *J. Phys. Chem* **1996**, *100*, 201–206.

[105] Chong, T.; Li, P.; Leong, W.; Fan, W. *J. Organomet. Chem.* **2005**, *690*, 4132–4138.

[106] Cheng, T.; Bullock, R. *J. Am. Chem. Soc.* **1999**, *121*, 3150–3155.

Appendix A

Matlab Program for Data Analysis

Below is an example input file for the Matlab program kinetics_6.m. The first line of the program gives the base name for the file. The path is included if it is different from the one that contains the Matlab program. The files are numbered in the LabView program. The file number is given in the first column and the wavelength at which that kinetic traces was taken is given in the second column.

```
Data/CrCO6/9_29_03/9_29_CrCO6_
4       1960
5       1960
7       1960
8       1887
9       1887
10      1892
11      1892
12      1897
13      1897
14      1902
15      1902
16      1907
```

The Matlab program written for analyzing kinetic data is shown below. This is the most recent version of the program and served as the basis for the spectral array data analysis programs.

```
%-------------------------------------------------------------------------%
% kinetics_6.m                                                            %
%-------------------------------------------------------------------------%
close all;
```

```
clear;
%------------------------------------------------------------------------%
% Read input file and obtain info about filename and wavenumber          %
%------------------------------------------------------------------------%

inputfile = input('What is the name of the spectral input file? ','s');
if length(inputfile)==0;
  inputfile='specinfo.txt';
end
fin = fopen(inputfile,'r');
if fin < 0
  error(['Could not open ',inputfile,' for input']);
end

filebody = fgetl(fin);
specinfo = fscanf(fin,'%f');
nmbrfiles = length(specinfo)/2;
specinfo = reshape(specinfo,2,nmbrfiles);
specinfo = specinfo.';
specinfo = sortrows(specinfo,2);

%------------------------------------------------------------------------%
% Read in time info. from 1st column of 1st file - all stage files must  %
% contain the same time info or be altered to mimick the same time info  %
%------------------------------------------------------------------------%

filename = strcat(filebody,num2str(specinfo(1,1)));
tfin = fopen(filename,'r');

for i=1:5
  dataline = fgetl(tfin);
end

dataline = str2num(dataline);
column=length(dataline);
frewind(tfin);

for i=1:4
  header = fgetl(tfin);
end

tdata = fscanf(tfin,'%f');
```

```
rows = length(tdata)/column;
tdata = reshape(tdata,column,rows);
tdata = tdata.';
alltimepts = tdata(:,1);
nmbrtimepts = length(alltimepts)/2;
timepts = tdata(1:nmbrtimepts,1);

%-------------------------------------------------------------------------%
% Input all of the data collected into a cell array                       %
%-------------------------------------------------------------------------%

wavenmbrs = zeros(size(specinfo(:,1)));

for k=1:nmbrfiles
  wavenmbrs(k) = specinfo(k,2);
  filename = strcat(filebody,num2str(specinfo(k,1)));
  fin = fopen(filename,'r');
  for i=1:4
    header = fgetl(fin);
  end
  inputdata = fscanf(fin,'%f');
  columns = length(inputdata)/rows;
  inputdata = reshape(inputdata,columns,rows);
  inputdata = inputdata.';
  increasing = inputdata(1:nmbrtimepts,2:columns);
  nmbralltimepts = length(alltimepts);
  decreasing = inputdata(nmbrtimepts+1:nmbralltimepts,2:columns);
  decreasing = flipud(decreasing);
  InputData{k} = cat(2,increasing,decreasing);
  nmbrscans = (columns-1)*2;
end

%-------------------------------------------------------------------------%
% Find out if multiple files were collected at the same wavelength and,  %
% if they were put them together into a single array in a new cell       %
%-------------------------------------------------------------------------%

k = 1;

if wavenmbrs(1) == wavenmbrs(2)
  SortedInputData{1} = cat(2,InputData{1},InputData{2});
else
```

```
  SortedInputData{1} = InputData{1};
end

SortedWaveNumbers(1) = wavenmbrs(1);

if wavenmbrs(1) == wavenmbrs(2)
  k = 3;
else
  k = 2;
end

while k < (nmbrfiles+1)
  ind = length(SortedInputData);
  if wavenmbrs(k) == wavenmbrs(k-1)
    SortedInputData{ind} = cat(2,SortedInputData{ind},InputData{k});
    SortedWaveNumbers(ind) = wavenmbrs(k);
  else
    SortedInputData{ind+1} = InputData{k};
    SortedWaveNumbers(ind+1) = wavenmbrs(k);
  end
  k = k + 1;
end

nmbrwvlngths = length(SortedInputData);
for x=1:nmbrwvlngths
  clear snglscns
  snglscns=SortedInputData{x};
  [M,N]=size(SortedInputData{x});
  norm1=sum(snglscns(:,1));
  for y=2:N
    norm2=sum(snglscns(:,y));
    scale=norm1/norm2;
    snglscns(:,y)=snglscns(:,y)*scale;
  end
  SortedInputData{x}=snglscns;
end
%-------------------------------------------------------------------------%
% Now the cell will be split up into arrays (one for each wavelength)  %
% and outliers are thrown out according to Matthias's routine. Similar %
% data will then be averaged and standard deviations calculated.  All  %
% of this data is put into two arrays - one with averaged values and   %
% one with standard deviations                                         %
```

```
%-------------------------------------------------------------------------%

devpm = input('# standard deviations (1-3)? ');
if length(devpm)==0;
  devpm=3;
end
nmbrwvlngths = length(SortedInputData);

for k=1:nmbrwvlngths
  snglwvdata = SortedInputData{k}
  [timepoints,nmbrscns] = size(SortedInputData{k});
  percent=round(nmbrscns*0.1);
  if nmbrscns > 2
    for i=1:nmbrtimepts;
      outlierdata = snglwvdata(i,:);
      outlierdata = sort(outlierdata);
      cutdata = outlierdata(percent+1:nmbrscns-percent);
      DataDevHelp = std(cutdata);
      DataAveHelp = mean(cutdata);
      clear SnglWvData;
      l = 1;
      for j=1:nmbrscns
        if (outlierdata(j) >= (DataAveHelp-devpm*DataDevHelp)) &
(outlierdata(j)<=(DataAveHelp+devpm*DataDevHelp));
          SnglWvData(l) = outlierdata(j);
          l = l + 1;
        end
      end
      avewavedata(i,k) = mean(SnglWvData);
      stddevdata(i,k) = std(SnglWvData);
    end
    dataarray(:,k) = avewavedata(:,k);
    stddevarray(:,k) = stddevdata(:,k);
    else
      snglwvdata = snglwvdata.';
      avewavedata = mean(snglwvdata);
      avewavedata = avewavedata.';
      stddevdata = std(snglwvdata);
      stddevdata = stddevdata.';
      dataarray(:,k) = avewavedata;
      stddevarray(:,k) = stddevdata;
    end
```

```
  end
end

%-------------------------------------------------------------------------%
% Routine for baseline correction (first five time points are used)    %
%-------------------------------------------------------------------------%

basecorr = input('Baseline correction (-5 to -1 ps)? (y/n) ','s');
if (basecorr == 'y') | (basecorr=='Y')
  for k=1:nmbrwvlngths
    baseave = 0;
    for j=1:5
    baseave=baseave+dataarray(j,k);
   end
   baseave=baseave/5;
  for j=1:timepoints
      dataarray(j,k)=dataarray(j,k)-baseave;
  end
  end
end

%-------------------------------------------------------------------------%
% Time and wavelength data are now put into the array                   %
%-------------------------------------------------------------------------%

[M,N] = size(dataarray);
m = M+1; n = N+1;

Output(2:m,1) = timepts(:);
Output(1,2:n) = SortedWaveNumbers;
Output(2:m,2:n) = dataarray;
StdDevData(2:m,1) = timepts(:);
StdDevData(1,2:n) = SortedWaveNumbers;
StdDevData(2:m,2:n) = stddevarray;

outputfileboolean = input('Do you want to write the output array to a
  file (y/n)? ','s');
if (outputfileboolean == 'y') | (outputfileboolean == 'Y')
  disp('  The file for the output array will be saved as output.dat ');
  save output.dat Output -ascii
end
```

```
stddevfileboolean = input('Do you want to write the standard deviation
  array to a file (y/n)? ','s');
if (stddevfileboolean == 'y') | (stddevfileboolean == 'Y')
  disp('The standard deviation file will be saved as stddev.dat ');
  save stddev.dat StdDevData -ascii
end

plots = input('Would you like  plots of your data? (y/n) ','s');
if (plots=='y') | (plots=='Y')
  errbarsboolean = input('Would you like error bars on your plots?
(y/n) ','s');
  if (errbarsboolean == 'y') | (errbarsboolean == 'Y')
    specplot=input('Would you like  a plot of the spectral data?
(y/n) ', 's');
    if (specplot=='y') | (specplot=='Y')
      disp('Which time slices would you like to plot? (Up to seven')
      whichspecs=input('can be plotted at one time - these should be
entered as [1,2,...]) ');
      whichspecs = whichspecs+1;
      numplots=length(whichspecs);
      errorbar(Output(1,2:n),Output(whichspecs(1),2:n),
stddevarray(whichspecs(1),:));
      hold on;
      if numplots>=2;
        errorbar(Output(1,2:n),Output(whichspecs(2),2:n),
stddevarray(whichspecs(2),:),'r');
      end;
      if numplots>=3;
        errorbar(Output(1,2:n),Output(whichspecs(3),2:n),
stddevarray(whichspecs(2),:),'g');
      end;
      if numplots>=4;
        errorbar(Output(1,2:n),Output(whichspecs(4),2:n),
stddevarray(whichspecs(3),:),'m');
      end;
      if numplots>=5;
        errorbar(Output(1,2:n),Output(whichspecs(5),2:n),
stddevarray(whichspecs(4),:),'c');
      end;
      if numplots>=6;
        errorbar(Output(1,2:n),Output(whichspecs(6),2:n),
stddevarray(whichspecs(5),:),'k');
```

```
      end;
      if numplots>=7;
        errorbar(Output(1,2:n),Output(whichspecs(7),2:n),
stddevarray(whichspecs(6),:),'y');
      end;
    end
    timeplot=input('Would you like a kinetic plot? (y/n) ', 's');
    if (timeplot=='y') | (timeplot=='Y')
      disp('Which spectral slices would you like to plot? (Up to')
      whichtimes=input('seven can be plotted at one time - these should
be entered as [1,2,...]) ');
      figure;
      whichtimes = whichtimes+1;
      numplots2=length(whichtimes);
      errorbar(timepts,dataarray(:,whichtimes(1)),
stddevarray(:,whichtimes(1)));
      hold on;
      if numplots2>=2;
        errorbar(timepts,dataarray(:,whichtimes(2)),
stddevarray(:,whichtimes(2)),'r');
      end;
      if numplots2>=3;
        errorbar(timepts,dataarray(:,whichtimes(3)),
stddevarray(:,whichtimes(3)),'g');
      end;
      if numplots2>=4;
        errorbar(timepts,dataarray(:,whichtimes(4)),
stddevarray(:,whichtimes(4)),'m');
      end;
      if numplots2>=5;
        errorbar(timepts,dataarray(:,whichtimes(5)),
stddevarray(:,whichtimes(5)),'c');
      end;
      if numplots2>=6;
        errorbar(timepts,dataarray(:,whichtimes(6)),
stddevarray(:,whichtimes(6)),'k');
      end;
      if numplots2>=7;
        errorbar(timepts,dataarray(:,whichtimes(7)),
stddevarray(:,whichtimes(7)),'y');
      end;
    end;
```

```
    else if (errbarsboolean == 'n') | (errbarsboolean == 'N')
      specplot=input('Would you like to generate a spectral plot?
(y/n) ', 's');
        if (specplot=='y') | (specplot=='Y')
        [p,q] = size(Output);
        wn = Output(2:p,1);
      wn = wn.';
      p = p-1;
      i = (1:p);
      nmbrs = cat(1,i,wn);
      disp('  ');
      disp(nmbrs);
        disp('Which time slices would you like to plot? ')
        whichspecs=input('(these should be entered as [1,2,...]) ');
        whichspecs = whichspecs+1;
        numplots=length(whichspecs);
        plot(Output(1,2:n),Output(whichspecs,2:n));
        for s=1:numplots
          lgnd = sprintf('%4.0f',(Output(whichspecs(s),1)));
          lgnds{s}=lgnd;
        legend(lgnds);
      end;
        titlename = input('Type a title for the spectral plot: ','s');
        title(titlename);
        xlabel('Wavenumbers (cm-1)');
        ylabel('Absorbance (mOD)');
      end
      timeplot=input('Would you like to generate a kinetic plot?
(y/n) ', 's');
      if (timeplot=='y') | (timeplot=='Y')
      [p,q]=size(Output);
      tm = Output(1,2:q);
      q = q-1;
        i = (1:q);
       nmbrs = cat(1,i,tm);
      disp('  ');
      disp(nmbrs);
        disp('Which spectral slices would you like to plot? ')
        whichtimes=input('(these should be entered as [1,2,...]) ');
        figure;
        numplots2=length(whichtimes);
      whichtimes = whichtimes + 1;
```

```
        plot(Output(2:m,1),Output(2:m,whichtimes));
      for s=1:numplots2
        lgnd2 = sprintf('%4.0f',(Output(1,whichtimes(s))));
        lgnds2{s}=lgnd2;
          legend(lgnds2);
        end;
        titlename = input('Type a name for the kinetics plot: ','s');
        title(titlename);
        xlabel('Time (ps)');
        ylabel('Absorbance (mOD)');
      end
    end
  end
  difplot=input('Would you like to generate a difference spectra?
 (y/n) ', 's');
  if (difplot=='y') | (difplot=='Y')
    disp('Difference spectra will be plotted with reference to the ')
    disp('first time slice in the data')
    disp('Which time slices would you like to plot? ')
    difspecs=input('(these should be entered as [1,2,...]) ');
    numplots3=length(difspecs);
    difspecs = difspecs+1;
  figure;
  for s=1:numplots3;
      DifSpecs(s,:) = Output(difspecs(s),2:n)-Output(2,2:n);
      lgnd3 = sprintf('%4.0f',Output(difspecs(s),1));
      lgnds3{s} = lgnd3;
  end;
  plot(Output(1,2:n),DifSpecs(:,:));
  legend(lgnds3);
  end;
  titlename = input('Type a title for the difference plot: ','s');
  title(titlename);
  xlabel('Wavenumbers (cm-1)');
  ylabel('Absorbance (mOD)');
end
```

Appendix B

Langevin Dynamics Computer Code

```
/* Input file for 1-butanol for use with langevin.c or langevin.chainwalk.c */
Number of Particles 500
Time Step 0.500
Alkyl Sites 4
4 0 0 0
2 0 0 0
1 3 0 0
2 4 0 0
3 5 0 0
CH Sites 2
Alkyl Well Depth 3.67
CH Sites 2
Alkyl Well Depth 3.27
CH Sites 2
Alkyl Well Depth 5.07
CH Sites 3
Alkyl Well Depth 5.43
Hydroxyl Well Depth 16.40
Critical Temperature 563.1
Vibrational Relaxation Time 30
Viscosity 2.524
Equation Number 1
A -5.9719
B 1007
C 0
```

The code that follows is langevin.c - this code simulates a random (stochastic) rearrangment.

```
#include ⟨stdio.h⟩
#include ⟨math.h⟩
#include ⟨stdlib.h⟩
#include ⟨stddef.h⟩
#include ⟨string.h⟩
#include ⟨time.h⟩
#include ⟨limits.h⟩

double ran3(long int *seed_flag);
double gauss(void);
float temp(int time, float dt,float Tc,float Tvib);
float eta(float T, float A, float B,float C);

void main()
{
float A,B,C;                /* Viscosity Equation Constants */
float pi=3.1415926535897;
float m=0.192;              /* mass of CrCO5 in kg/mol */
float d=6;                  /* particle diameter in angstroms */
float xi;                   /* friction coefficient in units of inverse ps */
float T;                    /* Current Temperature */
float K = 8.314;            /* boltzmann constant */
float dt;                   /* time step in picoseconds */
float limit;                /* time limit - maximum number of steps */
float L=3.0;                /* site to site distance for pes in angstroms */
float Tc;                   /* Critical Temperature */
float exp1;                 /* dummy variable */
float sr, sr2;              /* position variance */
float sv, sv2;              /* velocity variance */
float c12;                  /* position-velocity correlation function */
float x,xdt;                /* position on potential surface at time t+dt */
float X;                    /* reduced position to determine coordination site */
float v, vdt;               /* velocity of the particle at time t+dt */
float a;                    /* acceleration of the particle at time t */
float adt;                  /* acceleration of the particle at time t+dt */
float u;                    /* value of the potential well depth at a given site */
float V;                    /* potential energy */
float ke;                   /* kinetic energy */
float F;                    /* force */
unsigned N;                 /* number of alkyl sites */
```

```
float M2;                   /* number of CH sites - for use with H statistics */
float M;                    /* dummy variable for site index */
int n;                      /* number of simulation particles */
int dist;                   /* distribution counter */
int i,j,k,l;                /* counter indices */
float EQTN;                 /* viscosity equation number */
long int rand_flag=1;       /* random number initialization seed */
float U[10];                /* well depths for all binding sites */
float r1, r2;               /* random sample from gauss() */
float R1, R2;               /* corresponding variable for fluctuating force */
float c0, c1, c2;           /* integration constants for move formula */
FILE *of1, *of2, *of3;      /* output files */
FILE *ifp;                  /* input parameter file pointer */
int time;                   /* current simulation time */
char times[10], *end;       /* number of times to run simulation */
int loop;                   /* number of simulation sets to run */
float lower, upper;         /* well limits */
float help1, help7;         /* temp value */
float visc;                 /* current viscosity */
float Tvib;                 /* Vibrational Relaxation Time in psec */
char VR[10], CH[10];        /* Simulation Choices */
char infile[80];            /* Input file name */
char help2[80];             /* Dummy string array for input file labels */
char outfile1[80], outfile2[80],outfile3[80];     /* Output file names */
char help4[80],help5[80],help6[80];               /* Dummy string array for output file names */
int steve;                  /* Counter for average time per well calculation */
float OH_well;              /* Variable for the OH well bounds */
float monkey, chicken;      /* IN HONOR OF PRESTON SNEE and STEVE -*/
                            /* positions at which a particle is trapped in OH well */


/* Input Simulation information */
printf("Enter the number of times that you would like to run: ");
scanf("%i",&loop);
printf("Enter the filename base of the file: ");
scanf("%s",infile);
ifp=fopen(infile, "r");

/* Scan in data from input file-all strings are written over and variables are saved */
fscanf(ifp,"%s%s%s%i",&help2,&help2,&help2,&n);
fscanf(ifp,"%s%s%f",&help2,&help2,&dt);
fscanf(ifp,"%s%s%f",&help2,&help2,&X);
```

```
/* Throw away the connection matrix */
/* This will only be used when a chainwalk simulation is run */
N=X;
X=1.0;
for (i=0; i<(N+1); ++i) {
  fscanf(ifp,"%f%f%f%f",&help2,&help2,&help2,&help2);
}
printf("Do you want to use Carbon or Hydrogen statistics? (C/H) ");
/* Construct the site array based on the type of simulation to be run */
/* Carbon or hydrogen statistics can be chosen */
scanf("%s",&CH);
if(!strcmp(CH,"C")) {
  for (i=0; i<N; ++i) {
    fscanf(ifp,"%s%s%f", &help2,&help2,&M2);
    fscanf(ifp,"%s%s%s%f", &help2,&help2,&help2,&U[(i+1)]);
    X=N+1.0;
  }
}
if(!strcmp(CH,"H")) {
  l=1;
  for (i=0; i<N; ++i) {
    fscanf(ifp,"%s%s%f", &help2,&help2,&M2);
    M=M2+1;
    fscanf(ifp,"%s%s%s%f", &help2,&help2,&help2,&help7);
    for (j=1; j<M; ++j) {
      U[(l)]=help7;
      l=l+1;
    }
    X=X+M-1;
  }
}
fscanf(ifp,"%s%s%s%f", &help2,&help2,&help2, &U[0]);
printf("Do you want to include vibrational relaxation? (Y/N) ");
scanf("%s",&VR);
fscanf(ifp,"%s%s%f",&help2,&help2,&Tc);
fscanf(ifp,"%s%s%s%f",&help2,&help2,&help2,&Tvib);
fscanf(ifp,"%s%f",&help2,&visc);
fscanf(ifp,"%s%s%f",&help2,&help2,&EQTN);
fscanf(ifp,"%s%f",&help2,&A);
```

```
fscanf(ifp,"%s%f",&help2,&B);
fscanf(ifp,"%s%f",&help2,&C);

if (EQTN==1) {
 B=-B;
}

/* Find OH well limits for trapping based on a room temperature distribution */
if(!strcmp(VR,"N")) {
  help1=(-6*.4184/9+(U[0]*.4184/9/2));
  help1=-2*L*L/U[0]/.4184*help1;
  help1=acos(help1);
  help1=help1/pi/2;
  OH_well=help1-0.5;
  monkey=OH_well+1;
  chicken=-OH_well;
  T = 298;
  Tc = 298;
}
fclose(ifp);

/* Open output files for writing. Usually, only of3 is used as an output. */
/* of1 is used for error checking and of2 is used for distribution examination */
sprintf(outfile1, "%s%s%s","trajectory.",infile,".");
sprintf(outfile2, "%s%s%s","dist.",infile,".");
sprintf(outfile3, "%s%s%s","time.",infile,".");

/* This loop is for each set of simulations-each set containing n trajectories */
for (k=1; k<=loop; k++) {
  sprintf(times, "%i",k);
  sprintf(help4, "%s%s", outfile1, times);
  sprintf(help5, "%s%s", outfile2, times);
  sprintf(help6, "%s%s", outfile3, times);
  of1 = fopen(help4, "w");
  of2 = fopen(help5, "w");
  of3 = fopen(help6, "w");
  limit=50000/dt;
  steve=0;

  /* This loop is for each particle in a given set of simulations */
  for (j=0; j<n; j++) {
    dist=0;
```

```
   time=1;

/* Randomly choose the initial velocity from a thermal distribution */
   v = gauss();
    v = (sqrt(K*Tc/m))*v*0.01/L;
/* This loop is to ensure that a trajectory is not too long. */
/* The limit is set to be 100000 setps when dt=0.50 */
/* This limit is not met unless something bad is happening - i.e. some error */
   while(time<(limit)) {
/* Randomly choose a well */
     x = ran3(&rand_flag);
/* Determine which well you are in and what the well depth is */
     for (i=0; i<X; i++) {
       if(((i/X) < x) && (x < ((i+1)/X))) {
         u = U[(i)];
         u=u*.4184;
         break;
       }
     }
/* Randomly choose a position */
     x = ran3(&rand_flag);
     steve++;
l = 0;
/* Determine the limits for the particle to be bound. */
/* Based on 10kT below OH well barrier. */
     if(!strcmp(VR, "Y")) {
       T=temp(time,dt,Tc,Tvib);
       help1=-(6.0/298.0*T);
       help1=help1*.4184/9+(U[0]*.4184/9/2);
       help1=-2*L*L/U[0]/.4184*help1;
       help1=acos(help1);
       help1=help1/pi/2;
       OH_well=help1-0.5;
       monkey=OH_well+1;
       chicken=-OH_well;
     }
     if(monkey<chicken) {
       monkey=-OH_well;
       chicken=OH_well+1;
     }
/* If the particle is trapped in the OH well - stop the trajectory */
     if((i==0) && ((x>chicken) && (x<monkey))) {
```

```
      fprintf(of1,"%i\ t%i\ t%i\ t%i\ t%f\ t%f\ t%f\ n",j,i,l,time,x,v,T);
      break;
    }
/* If the particle is not trapped, move the particle along the PES */
/* until it becomes unbound or trapped*/
    else while((0<x) && (x<1.0)) {
      dist=dist+1;
      l=l+1;
/* Change the temperature according to the time. */
/* This changes the viscosity and the bounding limits for OH well */
      if(!strcmp(VR, "Y")) {
        T=temp(time,dt,Tc,Tvib);
        help1=-(6.0/298.0*T);
        help1=help1*.4184/9+(U[0]*.4184/9/2);
        help1=-2*L*L/U[0]/.4184*help1;
        help1=acos(help1);
        help1=help1/pi/2;
        OH_well=help1-0.5;
        monkey=OH_well+1;
        chicken=-OH_well;
      }
/* If the particle becomes trapped in the OH well, stop the trajectory */
      if((i==0) && ((x>chicken) && (x< monkey))) {
        fprintf(of1,"%i\ t%i\ t%i\ t%i\ t%f\ t%f\ t%f\n",j,i,l,time,x,v,T);
        break;
      }
/* Calculate the force based on the position on the PES. */
/* Calculate acceleration from the force. */
      help1=(2*x+1)*pi;
      help1=cos(help1);
      help1=-(u/2)/L/L*help1;
      V = help1-(u/2/L/L);
      ke = 0.5*m*v*v;
      F = (2.0*(u/2)*(sin((2.0*x+1.0)*pi)));
      F = (float) -F * pi/L/L/L;
      a = F/m;
/* Calculate the viscosity at the present temperature */
      if(!strcmp(VR, "Y")) {
        visc=eta(T,A,B,C);
      }
/* All of this is required to carry out the motion along the PES according to */
/* the Langevin Equation - see Allen & Tildesley Chapter 9 for details */
```

```
        xi=2*pi*visc*d*.0602/m;
        exp1 = exp(-(xi*dt));
        sr2=exp1*exp1;
        sr2 = (3-(4*(exp1))+sr2);
        sr2 = (1/xi/dt*sr2);
        sr2 = 2.0-sr2;
        sr2 = (dt*K*T/m)*(1.0/xi)*sr2;
        sr = sqrt(sr2)*0.01/L;
        sv2 = (K*T/m)*(1-(exp1*exp1));
        sv = sqrt(sv2)*0.01/L;
        c12 = (K*T/m/xi)*(1-exp1)*(1-exp1)/L/L;
        c12 = 0.0001*c12/sr/sv;
        c0 = exp1;
        c1 = (1/xi/dt)*(1-c0);
        c2 = (1/xi/dt)*(1-c1);
        r1 = gauss();
        r2 = gauss();
        R1 = sr*r1;
        R2 = ((sqrt(1-(c12*c12)))*r2);
        R2 = sv*((c12*r1) + R2);
/* Movement of the particle is based on an algorithm given by Allen & Tildesley */
        xdt = x+c1*dt*v + c2*dt*dt*a+R1;
        F=(2.0*(u/2)*(sin((2.0*xdt+1.0)*pi)));
        F = (float) -F * pi/L/L/L;
        adt = F/m;
        vdt = c0*v + (c1-c2)*dt*a + c2*dt*adt+R2;
        fprintf(of1,"%i\ t%i\ t%i\ t%i\ t%f\ t%f\ t%f\n",j,i,l,time,x,v,T);
/* Print the distribution information */
        if(dist==20) {
          fprintf(of2,"%i\ t%f\ t%i\n",time,x,i);
          dist=0;
        }
/* Increment time, position, and velocity to new values */
        time=time+1;
        x=xdt;
        v=vdt;
      }
/* End the simulation if the particle is trapped - otherwise, loop through again */
      if((i==0) && ((x>chicken) && (x<monkey))) {
        break;
      }
    }
```

```
    fprintf(of3,"%i\ t%i\n",j,time);
  }
fclose(of1);
fclose(of2);
fclose(of3);
}
}
```

The code that follows is langevin.chainwalk.c - this code simulates a chainwalk rearrangement - biased and random.
All of the libraries and most of the variables are identical to those given in langevin.c. The code shown here starts at the end of the constant and variable declaration section. Only those variables that are new to the code are shown. All of the remaining code is shown for the langevin.chainwalk.c simulations.

```
float x2;                   /* random well selection index */
float nlinks;               /* number of connections */
float links[4][6];          /* Connection Matrix */
float branch[10];           /* Number of Connections for each site */
float biasT;                /* Variable for use in biasing the site choice */
int biasHelp1,biasHelp2;    /* Well index for biasing the site choice */



/* Input Simulation information */
printf("Enter the number of times that you would like to run: ");
scanf("%i",&loop);
printf("Enter the filename base of the file: ");
scanf("%s",infile);
ifp=fopen(infile, "r");
/* Scan in data from input file - all strings are written over and variables are saved */
fscanf(ifp,"%s%s%s%i",&help2,&help2,&help2,&n);
fscanf(ifp,"%s%s%f",&help2,&help2,&dt);
fscanf(ifp,"%s%s%f",&help2,&help2,&X);
N=X;
X=1.0;
/* This part of the code reads in the connection matrix and then counts the */
/* number of connections present for each site on the carbon chain */
for (i=0; i<(N+1); ++i) {
  branch[i]=0.0;
  fscanf(ifp,"%f%f%f%f",&links[0][i],&links[1][i],&links[2][i],&links[3][i]);
  for(j=0; j<4; ++j) {
    if(links[j][i] != 0.0) {
      branch[i]=branch[i]+1.0;
    }
  }
}

printf("Do you want to bias the chainwalk by well depth? (Y/N) ");
scanf("%s",&Bias);
```

```
/* Construct the array of well depths based on C statistics */
for (i=0; i<N; ++i) {
  fscanf(ifp,"%s%s%f", &help2,&help2,&M2);
  fscanf(ifp,"%s%s%s%f", &help2,&help2,&help2,&U[(i+1)]);
  X=N+1.0;
}
fscanf(ifp,"%s%s%s%f", &help2,&help2,&help2, &U[0]);
printf("Do you want to include vibrational relaxation? (Y/N) ");
scanf("%s",&VR);

fscanf(ifp,"%s%s%f",&help2,&help2,&Tc);
fscanf(ifp,"%s%s%s%f",&help2,&help2,&help2,&Tvib);
fscanf(ifp,"%s%f",&help2,&visc);
fscanf(ifp,"%s%s%f",&help2,&help2,&EQTN);
fscanf(ifp,"%s%f",&help2,&A);
fscanf(ifp,"%s%f",&help2,&B);
fscanf(ifp,"%s%f",&help2,&C);

if (EQTN==1) {
  B=-B;
}

/* Find OH well limits for trapping based on a room temperature distribution */
if(!strcmp(VR,"N")) {
  help1=(-6*.4184/9+(U[0]*.4184/9/2));
  help1=-2*L*L/U[0]/.4184*help1;
  help1=acos(help1);
  help1=help1/pi/2;
  OH_well=help1-0.5;
  monkey=OH_well+1;
  chicken=-OH_well;
  T = 298;
  Tc = 298;
}
fclose(ifp);

/* Open output files for writing. Usually, only of3 is used as an output. */
/* of1 is used for error checking and of2 is used for distribution examination */
sprintf(outfile1, "%s%s%s","trajectory.",infile,".");
sprintf(outfile2, "%s%s%s","dist.",infile,".");
sprintf(outfile3, "%s%s%s","time.",infile,".");
```

```
/* This loop is for each set of simulations - each set containing n trajectories */
for (k=1; k<=loop; k++) {
  sprintf(times, "%i",k);
  sprintf(help4, "%s%s", outfile1, times);
  sprintf(help5, "%s%s", outfile2, times);
  sprintf(help6, "%s%s", outfile3, times);
  of1 = fopen(help4, "w");
  of2 = fopen(help5, "w");
  of3 = fopen(help6, "w");
  limit=50000/dt;
  steve=0;
/* This loop is for each particle in a given set of simulations */
  for (j=0; j<n; j++) {
    dist=0;
    time=1;
* Randomly choose the initial velocity from a thermal distribution */
    v = gauss();
    v = (sqrt(K*Tc/m))*v*0.01/L;
/* Choose an initial potential well */
    x = ran3(&rand_flag);
    for (i=0; i<X; i++) {
      if(((i/X) < x) && (x < ((i+1)/X))) {
        break;
      }
    }
/* Choose an initial position */
    x = ran3(&rand_flag);

/* This loop is to ensure that a trajectory is not too long. */
/* The limit is set to be 100000 setps when dt=0.50 */
/* This limit is not met unless something bad is happening - i.e. some error */
    while(time<(limit)) {
/* Assign the well depth for the chosen well */
      u = U[(i)];
      u=u*.4184;
      steve++;
      l = 0;
/* Determine the limits for the particle to be bound. */
/* Based on 10kT below OH well barrier. */
      if(!strcmp(VR, "Y")) {
        T=temp(time,dt,Tc,Tvib);
        help1=-(6.0/298.0*T);
```

```
      help1=help1*.4184/9+(U[0]*.4184/9/2);
      help1=-2*L*L/U[0]/.4184*help1;
      help1=acos(help1);
      help1=help1/pi/2;
      OH_well=help1-0.5;
      monkey=OH_well+1;
      chicken=-OH_well;
    }
    if(monkey<chicken) {
      monkey=-OH_well;
      chicken=OH_well+1;
    }
/* If the particle is trapped in the OH well stop the trajectory */
    if((i==0) && ((x>chicken) && (x<monkey))) {
      fprintf(of1,"%i\ t%i\ t%i\ t%i\ t%f\ t%f\ t%f\ n",j,i,l,time,x,v,T);
      break;
    }
/* If the particle is not trapped, move the particle along the PES */
/* until it becomes unbound or trapped*/
    else while((0<x) && (x<1.0)) {
      dist=dist+1;
      l=l+1;
/* Change the temperature according to the time. */
/* This changes the viscosity and the bounding limits for OH well */
      if(!strcmp(VR, "Y")) {
        T=temp(time,dt,Tc,Tvib);
        help1=-(6.0/298.0*T);
        help1=help1*.4184/9+(U[0]*.4184/9/2);
        help1=-2*L*L/U[0]/.4184*help1;
        help1=acos(help1);
        help1=help1/pi/2;
        OH_well=help1-0.5;
        monkey=OH_well+1;
        chicken=-OH_well;
      }
/* If the particle is trapped in the OH well - stop the trajectory */
      if((i==0) && ((x>chicken) && (x<monkey))) {
        fprintf(of1,"%i\ t%i\ t%i\ t%i\ t%f\ t%f\ t%f\ n",j,i,l,time,x,v,T);
        break;
      }
/* Calculate the force based on the position on the PES. */
/* Calculate acceleration from the force. */
```

```
        help1=(2*x+1)*pi;
        help1=cos(help1);
        help1=-(u/2)/L/L*help1;
        V = help1-(u/2/L/L);
        ke = 0.5*m*v*v;
        F = (2.0*(u/2)*(sin((2.0*x+1.0)*pi)));
        F = (float) -F * pi/L/L/L;

        a = F/m;
/* Calculate the viscosity at the present temperature */
        if(!strcmp(VR, "Y")) {
          visc=eta(T,A,B,C);
        }
/* All of this is required to carry out the motion along the PES according to */
/* the Langevin Equation - see Allen & Tildesley Chapter 9 for details */
        xi=2*pi*visc*d*.0602/m;
        exp1 = exp(-(xi*dt));
        sr2=exp1*exp1;
        sr2 = (3-(4*(exp1))+sr2);
        sr2 = (1/xi/dt*sr2);
        sr2 = 2.0-sr2;
        sr2 = (dt*K*T/m)*(1.0/xi)*sr2;
        sr = sqrt(sr2)*0.01/L;
        sv2 = (K*T/m)*(1-(exp1*exp1));
        sv = sqrt(sv2)*0.01/L;
        c12 = (K*T/m/xi)*(1-exp1)*(1-exp1)/L/L;
        c12 = 0.0001*c12/sr/sv;
        c0 = exp1;
        c1 = (1/xi/dt)*(1-c0);
        c2 = (1/xi/dt)*(1-c1);
        r1 = gauss();
        r2 = gauss();
        R1 = sr*r1;
        R2 = ((sqrt(1-(c12*c12)))*r2);
        R2 = sv*((c12*r1) + R2);

/* Movement of the particle is based on an algorithm given by Allen & Tildesley */
        xdt = x+c1*dt*v + c2*dt*dt*a+R1;
        F=(2.0*(u/2)*(sin((2.0*xdt+1.0)*pi)));
        F = (float) -F * pi/L/L/L;
        adt = F/m;
        vdt = c0*v + (c1-c2)*dt*a + c2*dt*adt+R2;
```

```
      fprintf(of1,"%i\ t%i\ t%i\ t%i\ t%f\ t%f\ t%f\ n",j,i,l,time,x,v,T);
/* Print the distribution information */
      if(dist==20) {
        fprintf(of2,"%i\ t%f\ t%i\ n",time,x,i);
        dist=0;
      }
/* Increment time, position, and velocity to new values */
      time=time+1;
      x=xdt;
      v=vdt;
    }

/* End the simulation if the particle is trapped - otherwise, loop through again */
    if((i==0) && ((x>chicken) && (x<monkey))) {
      break;
    }
/* If the particle isn't trapped, assign a new position based on the old one. */
    if(x>1){
      x=x-1.0;
    }
    else {
      x=x+1.0;
    }
/* Select a random number for use in the new site selection */
    x2=ran3(&rand_flag);
    nlinks=branch[i];
    biasT=0;
/* In the biased chainwalk, selection of a new well is biased by the well depth. */
    if(!strcmp(Bias,"Y")) {
      for(p=0; p<nlinks; p++) {
        biasHelp1=links[p][i];
        if(links[p][i]==X) {
          biasHelp1=0;
        }
        biasT=biasT+U[biasHelp1];
      }
      lower = 0;
      biasHelp1=links[0][i];
      upper = U[biasHelp1];
      for(p=0; p<nlinks; p++) {
        biasHelp2=links[p+1][i];
        if(links[p+1][i]==X) {
```

```
          biasHelp2=0;
        }
        if(((lower/biasT) < x2) && (x2 < (upper/biasT))) {
          i=links[p][i];
          break;
        }
        lower = upper;
        upper = upper + U[biasHelp2];
      }
    }
/* In the random chainwalk simulation, the new site is chosen randomly from adjacent sites */
    else {
      for(p=0; p<nlinks; p++) {
        if(((p/nlinks) < x2) && (x2 < ((p+1)/nlinks))) {
          i=links[p][i];
          break;
        }
      }
    }
    if(i==X) {
      i=0.0;
    }
  }
  fprintf(of3,"%i\ t%i\ n",j,time);
 }
 fclose(of1);
 fclose(of2);
 fclose(of3);
 }
}
```

```
/* Temperature dependent viscosity equation */
float eta(float T, float A, float B,float C)
{
float ETA;
ETA=exp(A+B/(C-T));
return ETA;
}

/* Temperature calculation when vibrational relaxation is considered. */
/* The particle starts at its critical temperature and cools according to /* its characteristic vibrational re

float temp(int time,float dt,float Tc,float Tvib)
{
float T;
T=298+(Tc-298)*exp(-time*dt/Tvib);
return T;
}

/* Sample from gaussian bivariate distribution-from Allen & Tildesley Appendix G */
double gauss(void)
{
const double a1 = 3.949846138;
const double a3 = 0.252408784;
const double a5 = 0.076542912;
const double a7 = 0.008355968;
const double a9 = 0.029899776;

double r, r2, sum, ans;
int i;
long int rand_flag = 1;
double ran3(long int *seed_flag);

sum = 0.0;
for (i=1; i<=12; ++i)
  sum += ran3(&rand_flag);
  r=(sum - 6.0)/4.0;
  r2=r*r;
  ans = ((((a9 *r2 +a7) * r2 + a5) * r2 + a3) * r2 + a1) *r;
  return ans;
}
```

```
/* Random number generator - from Numberical Recipes in C */
const long int MBIG = 1000000000, MSEED = 161803398, MZ = 0;
const double FAC = (1.0 / 1000000000);
double ran3(long int *seed_flag) {
static long int inext, inextp, ma[56];
static long int iff = 0;
long int mj, mk;
double double_seed;
time_t seed;
int ind1, ind2, ind3;
if (*seed_flag < 0 —— iff == 0) {
  iff = 1;
  seed = time(NULL);
  srand(seed);
  while (1){
    double_seed = (double)(rand());
    if (double_seed > 0) break;
  }
  double_seed = double_seed/((double)(RAND_MAX))*((double)(MSEED))/10000;
  mj = MSEED - ((long int)(double_seed));
  mj = mj % MBIG;
  ma[55] = mj;
  mk = 1;
  for (ind1 = 1; ind1 < 55; ++ind1) {
    ind2 = (21 * ind1) % 55;
    ma[ind2] = mk;
    mk = mj - mk;
    if (mk < MZ) mk = mk + MBIG;
    mj = ma[ind2];
  }
  for (ind3 = 1; ind3 <=4; ++ind3){
    for (ind1 = 1; ind1 <= 55; ++ind1) {
      ma[ind1] = ma[ind1] - ma[1+(ind1 + 30) % 55];
      if (ma[ind1] < MZ) ma[ind1] = ma[ind1] + MBIG;
    }
    inext = 0;
```

```
    inext = 31;
    *seed_flag = 1;
  }
  ++inext;
  ++inextp;
  if (inext == 56) inext = 1;
  if (inextp == 56) inextp = 1;
  mj = ma[inext] - ma[inextp];
  if (mj < MZ) mj = mj + MBIG;
  ma[inext] = mj;
  return ((double)(mj) * FAC);
}
```